Title

Multi-stage Differentiation Defines Melanoma Subtypes with Differential Vulnerability to Drug-Induced Iron-Dependent Oxidative Stress

Author

Tsoi, Jennifer

Publication Date

2017

Peer reviewed|Thesis/dissertation

UNIVERSITY OF CALIFORNIA

Los Angeles

Multi-stage Differentiation Defines Melanoma Subtypes with Differential Vulnerability to Drug-Induced Iron-Dependent Oxidative Stress

A dissertation submitted in partial satisfaction of the

requirements for the degree of Doctor of Philosophy

in Molecular and Medical Pharmacology

by

Jennifer Tsoi

2017

ABSTRACT OF THE DISSERTATION

Multi-stage differentiation defines melanoma subtypes with differential vulnerability to drug-induced iron-dependent oxidative stress

by

Jennifer Tsoi

Doctor of Philosophy in Molecular and Medical Pharmacology

University of California, Los Angeles, 2017

Professor Thomas G. Graeber, Chair

Malignant transformation can result in melanoma cells that resemble different stages of their embryonic development. Our analysis of gene expression profiles from a large panel of human melanoma cell lines and patient tumors revealed that melanoma follows a two-dimensional differentiation trajectory that can be sub-classified into four progressive subtypes. This differentiation model is associated with subtype-specific sensitivity to iron dependent oxidative stress and cell death known as ferroptosis. Receptor tyrosine kinase mediated resistance to MAPK targeted therapies and activation of the inflammatory signaling associated with immune therapy involves transitions along this differentiation trajectory, which lead to increased sensitivity to ferroptosis. Therefore, ferroptosis-inducing drugs presents an orthogonal therapeutic approach to target the differentiation plasticity of melanoma cells to increase the efficacy of targeted and immune therapies. Melanoma cells are present at different differentiation states and have the ability to dedifferentiate under cellular stress. This has

important therapeutic implications as dedifferentiation contributes to intrinsic and acquired resistance to MAPK pathway inhibitors, and occurs as a response to inflammatory signaling during immunotherapy. Therefore, targeting dedifferentiation is a logical approach to strengthen these current therapeutic strategies. Here we categorize melanoma differentiation as four distinct stepwise stages and identify a heightened sensitivity to ferroptosis induction with the degree of differentiation. Our results further define tumor differentiation as an important parameter for patient stratification, and propose a new and highly orthogonal component to add to existing therapeutics, namely enhancing targeted signaling inhibition and immune therapies by synthetic lethal induction of ferroptosis.

The dissertation of Jennifer Tsoi is approved.

Heather R. Christofk

Alexander Hoffman

Antoni Ribas

Thomas G. Graeber, Committee Chair

University of California, Los Angeles

2017

Dedicated to my incredible mother,

my inspiration and source for strength, courage, and resilience.

TABLE OF CONTENTS

LIST OF FIGURES

CHAPTER 1. Melanoma subtypes based on multi-stage differentiation

CHAPTER 2. Melanoma differentiation subtype classifier identifies consistent subtypes in cell lines and tumors

CHAPTER 3. Melanoma dedifferentiation status is predictive marker of sensitivity to ferroptosis inducing drugs

APPENDIX

LIST OF TABLES

ACKNOWLEDGMENTS

This work would not have been possible without all the remarkable people that have supported me throughout this journey.

I would like to express my thanks to all members of the Graeber lab, past and present, who have in some way or another contributed to the completion of this work. Thank you for the support, ideas, advice, and flashes of inspiration. I would especially like to thank Kim Paraiso for stepping in to help with experiments and being a great resource for assistance and troubleshooting. I want to thank Carlos Galvan, Johnson Lay, Roksana Shirazi, and Katherine Sheu for helping out with various experiments and analyses. I would like to thank Daniel Braas for our discussions in interpreting metabolomics data. Finally, I also want to thank Kim, Johanna Scott, and Aspram Minasyan for being my support group, which has helped kept me grounded through some of the most difficult and frustrating times.

I would also like to express my thanks to members of the Ribas lab, past and present, who have always made me feel welcome and part of their lab by openly sharing cell lines, reagents, data, and experimental guidance. I especially want to thank Lidia Robert for our collaborative sessions that have been really instrumental in shaping the research direction of my dissertation, and for teaching me how to perform experiments in the lab. I want to thank Catie Grasso for mentoring me as a woman working in bioinformatics, being my advocate, and for teaching me the importance of “lumping and splitting” in science.

I want to thank my committee members Antoni Ribas, Heather Christofk, and Alex Hoffmann for their continual support and guidance. I am especially grateful to Toni for his co-mentorship, his infinite generosity in providing all the resources we needed to carry out this project, and his invaluable advice that has kept this project moving forward.

Importantly, I want to thank my advisor Tom Graeber for his mentorship over these past several years. Thank you Tom for your patience in teaching me how to systematically approach biological problems and introducing me to various bioinformatic algorithms. Thank you for giving me the support and freedom to explore my ideas. These years have definitely transformed the way I think and helped me grow as a scientist.

I want to also acknowledge funding from the UCLA Tumor Immunology Training Program (National Institutes of Health (NIH) Ruth L. Kirschstein Institutional National Research Service Award #T32-CA009120), which supported my training and this project.

Lastly, I want to thank those outside of my academic circle at UCLA, but have had a significant influence throughout my graduate school trajectory from start to finish. I want to thank my former supervisors/mentors at Amgen, Judy Shih and Chad Ray, for giving me opportunities to develop my career, for always believing in my potential, and for encouraging me to go to graduate school. I want to thank my friends for their support and understanding, and for reminding me that there is life outside of lab. I want to thank my family: my mother Cindy Luong, my sister Linda Tsoi, and my brother Kevin Tsoi for their constant support, love, and faith in me, which has kept me motivated throughout this journey.

The work for this dissertation was performed under the direction of Dr. Thomas G. Graeber.

Chapters 1-3 of this dissertation are based upon work from the manuscript:

Tsoi, J., Robert, L., Paraiso, K., Galvan, C., Sheu, K., Lay, J., Wong, D.J., Atefi, M., Shirazi, R., Wang, X., Braas, D., Grasso, C.S., Palaskas, N., and Ribas, A., Graeber, T.G. Multi-stage differentiation defines melanoma subtypes with differential vulnerability to drug-induced iron-dependent oxidative stress. (In Review*)*

VITA

EDUCATION:

University of Southern California — Los Angeles, CA
B.S. Chemical (Biochemical) Engineering — 2003 - 2007

PROFESSIONAL EMPLOYMENT:

Amgen, Pharmacokinetics and Drug Metabolism — Thousand Oaks, CA
Sr. Associate — 2010 – 2011
Associate — 2007 – 2010

Amgen, Purification Process Development — Thousand Oaks, CA
Undergraduate Intern — Summer 2006

GRANTS, FELLOWSHIPS and AWARDS:

UCLA Tumor Immunology Training Grant — 2013 - 2016
National Institutes of Health (NIH) Training Grant T32-CA009120

PUBLICATIONS:

Su, Y., Wei, W., Robert, L., Xue, M., **Tsoi, J.**, Garcia-Diaz, A., Moreno, B.H., Kim, J., Ng, R.H., Lee, J.W., et al. (2017). Single-cell analysis resolves the cell state transition and signaling dynamics associated with melanoma drug-induced resistance. PNAS 201712064.

Homet Moreno, B., Zaretsky, J.M., Garcia-Diaz, A., **Tsoi, J.**, Parisi, G., Robert, L., Meeth, K., Ndoye, A., Bosenberg, M.W., Weeraratna, A.T., Graeber, T.G., Comin-Anduix, B., Hu-Lieskovan, S., and Ribas, A. (2016). Response to programmed cell death-1 blockade in a murine melanoma syngeneic model requires costimulation, CD4, and CD8 T cells. Cancer Immunol Res.

Atefi, M., Titz, B., **Tsoi, J.**, Avramis, E., Le, A., Ng, C., Lomova, A., Lassen, A., Friedman, M., Chmielowski, B., Ribas, A., and Graeber, T.G. (2016). CRAF R391W is a melanoma driver oncogene. Sci Rep *6*, 27454.

Mok, S., **Tsoi, J.**, Koya, R.C., Hu-Lieskovan, S., West, B.L., Bollag, G., Graeber, T.G., and Ribas, A. (2015). Inhibition of colony stimulating factor-1 receptor improves antitumor efficacy of BRAF inhibition. BMC Cancer *15*, 356.

Hu-Lieskovan, S., Mok, S., Moreno, B.H., **Tsoi, J.**, Robert, L., Goedert, L., Pinheiro, E.M., Koya, R.C., Graeber, T.G., Comin-Anduix, B., and Ribas, A. (2015). Improved antitumor activity of immunotherapy with BRAF and MEK inhibitors in BRAFV600E melanoma. Sci Transl Med *7*, 279ra41-279ra41.

Müller, J., Krijgsman, O., **Tsoi, J.**, Robert, L., Hugo, W., Song, C., Kong, X., Possik, P.A., Cornelissen-Steijger, P.D.M., Foppen, M.H.G., Kemper, K., Goding, C.R., McDermott, U., Blank, C., Haanen, J., Graeber, T.G., Ribas, A., Lo, R.S., and Peeper, D.S. (2014). Low MITF/AXL ratio predicts early resistance to multiple targeted drugs in melanoma. Nat Commun *5*, 5712.

Wong, D.J., Robert, L., Atefi, M.S., Lassen, A., Avarappatt, G., Cerniglia, M., Avramis, E., **Tsoi, J.**, Foulad, D., Graeber, T.G., Comin-Anduix, B., Samatar, A., Lo, R.S., and Ribas, A. (2014). Antitumor activity of the ERK inhibitor SCH722984 against BRAF mutant, NRAS mutant and wild-type melanoma. Molecular Cancer *13*, 194.

Robert, L., **Tsoi, J.**, Wang, X., Emerson, R., Homet, B., Chodon, T., Mok, S., Huang, R.R., Cochran, A.J., Comin-Anduix, B., Koya, R.C., Graeber, T.G., Robins, H., and Ribas, A. (2014). CTLA4 Blockade Broadens the Peripheral T-Cell Receptor Repertoire. Clin Cancer Res *20*, 2424–2432.

Tsoi, J., Patel, V., and Shih, J. (2014). A practical approach to automate randomized design of experiments for ligand-binding assays. Bioanalysis *6*, 705–713.

Wang, J., Patel, V., Burns, D., Laycock, J., Pandya, K., **Tsoi, J.**, DeSilva, B., Ma, M., and Lee, J. (2013). Laboratory automation of high-quality and efficient ligand-binding assays for biotherapeutic drug development. Bioanalysis *5*, 1635–1648.

Rohle, D., Popovici-Muller, J., Palaskas, N., Turcan, S., Grommes, C., Campos, C., **Tsoi, J.**, Clark, O., Oldrini, B., Komisopoulou, E., Kunii, K., Pedraza, A., Schalm, S., Silverman, L., Miller, A., Wang, F., Yang, H., Chen, Y., Kernytsky, A., Rosenblum, M.K., Liu, W., Biller, S.A., Su, S.M., Brennan, C.W., Chan, T.A., Graeber, T.G., Yen, K.E., and Mellinghoff, I.K. (2013). An Inhibitor of Mutant IDH1 Delays Growth and Promotes Differentiation of Glioma Cells. Science *340*, 626–630.

Ray, C.A., Zhou, L., **Tsoi, J.**, Uy, L., Gu, J., Malella, J., Desimone, D., Gunn, H., Ma, M., Lee, J., et al. (2010). A strategy for improving comparability across sites for ligand binding assays measuring therapeutic proteins. J Pharm Biomed Anal *53*, 729–734.

Thway, T., Macaraeg, C., Calamba, D., Patel, V., **Tsoi, J.**, Ma, M., Lee, J., and Desilva, B. (2010). Applications of a planar electrochemiluminescence platform to support regulated studies of macromolecules: benefits and limitations in assay range. J Pharm Biomed Anal *51*, 626–632.

INTRODUCTION

Melanoma

Cutaneous melanoma is an aggressive and deadly form of skin cancer that arises from melanocytes, a pigment cell type of neural crest origin that function to protect the skin from ultraviolet radiation by production of melanin. In 2017, it is estimated that there will be 87,11 new cases of melanoma and 9,730 deaths in the US (Howlader et al., 2015). Overall, the 5-year survival rate of melanoma is over 90%, due to the majority of cases detected early and localized to the primary site of the skin. In this case, surgical resection is highly successful and curative with a 5-year survival rate of 98.5%. However, melanoma is a highly aggressive in nature and when left undetected can metastasize to distant areas in the body. Surgical resection is less successful in these cases, and the 5-year survival drops significantly to 62.9% and 19.9% when the tumor has spread to regional lymph nodes and distant sites respectively (Howlader et al., 2015). Melanoma can metastasizes to distant organs such brain, lung, liver, gastrointestinal tract, soft tissue, and bone. In patients where the cancer has metastasized to non-pulmonary visceral organs, the average survival is less than a year (Balch et al., 2009), demonstrating the urgent need for effective systemic therapy to treat metastatic disease.

Melanocyte development

The developmental history of melanocytes as progenitors from neural crest could potentially provide an explanation for the aggressive and invasive nature of melanoma. Neural crest cells are a transient, multi-potent, and highly migratory population of cells that arises from the neural tube during embryonic development (Mort et al., 2015; Sauka-Spengler and Bronner-Fraser, 2008; Thomas and Erickson, 2008). Neural crest cells are programmed to undergo an epithelial to mesenchymal-like transition to delaminate from the neural tube and migrate extensively to various regions throughout the embryo where they differentiate into multiple cell

lineages in addition to melanocytes, such as neurons, glia, bone, and cartilage derivatives. Melanocyte precursors, melanoblasts, migrate primarily dorsolaterally along ectoderm and must then invade into the ectoderm where they complete differentiation to melanocytes. The lineage switch from neural crest to melanoblasts and melanocytes is regulated through microphthalmia-associated transcription factor (MITF), the master regulator of melanocyte development and survival. MITF is expressed early in fate specification to melanoblasts via neural crest lineage transcription factors, paired-box transcription factor PAX3, and the SRY-related HMG-box transcription factor SOX10. MITF then activates the expression of genes involved in melanocytic properties and melanogenesis such as tyrosinase (TYR), tyrosinase-related protein 1 *(TYRP-1),* dopachrome tautomerase *(DCT), and* MART-1 *(MLANA).* Other signaling pathways are also proposed to be involved in the induction of MITF and its target genes such as β-catenin/Wnt and endothelin receptor B signaling (Hou et al., 2004; Schepsky et al., 2006; Takeda et al., 2000).

Role of MAPK/ERK pathway in melanoma

The majority of melanomas are driven through genomic alterations that result in the hyper-activation of the mitogen-activated protein kinase (MAPK) extracellular signal-regulated kinase (ERK) pathway. The MAPK/ERK pathway transmits extracellular signals through RAS, RAF, MEK and ERK proteins. The RAS protein is a small membrane GTPase that in its inactive state is GDP-bound. Ligand-mediated activation of receptor tyrosine kinases (RTK) promotes the loading of GTP and switches RAS to an “on” conformational state. In its active state RAS-GTP recruits RAF to the membrane, promoting RAF homodimerization or heterodimerization, and activation of the RAF kinases. Activated RAF phosphorylates MEK, which in turn phosphorylates ERK, and activated ERK phosphorylates other targets to promote survival and proliferation (Dhillon et al., 2007; Santarpia et al., 2012; Sullivan and Flaherty, 2013).

Approximately 15-30% of driver mutations occur in NRAS and another 40-60% of

mutations occur in BRAF (Akbani et al., 2015; Davies et al., 2002; Goel et al., 2006; Hodis et al., 2012). In NRAS, these mutations commonly work by stabilizing the binding and preventing hydrolysis of GTP, which maintains NRAS in the active conformation (Santarpia et al., 2012; Sullivan and Flaherty, 2013). While potentially a promising target, the structure of RAS and the high affinity for GTP has made development of RAS inhibitors challenging (Samatar and Poulikakos, 2014). Targeting BRAF has been more successful, as the most common BRAF mutation is from a valine to glutamic acid substitution in codon 600 (V600E, earlier misreported as V599E) and comprises about 90% of all BRAF-mutant cancers in general. This mutation reside in the kinase activation segment and acts as a phosphomimetic that renders BRAF constitutively active, functional as a monomer, and RAS-independent (Davies et al., 2002; Wan et al., 2004). This finding has led to the development of targeted therapies selectively against mutant $BRAF^{V600E}$ such as vemurafenib and dabrafenib that demonstrate impressive initial clinical response rates (Chapman et al., 2011; Flaherty et al., 2012; Hauschild et al., 2012). However, resistance generally develops in less than a year for these patients, while there still remain some patients intrinsically resistant to therapy.

The major route of resistance to mutant BRAF inhibitors is through reactivation of MAPK signaling (Samatar and Poulikakos, 2014). Genomic amplification of $BRAF^{V600E}$ leading to BRAF overexpression (Shi et al., 2012), and alternative splicing of $BRAF^{V600E}$ have both been observed in patients. The alternative splice variants encode a truncated BRAF protein that lacks a RAS-binding domain, resulting in enhanced dimerization capability and reduced sensitivity to RAF inhibitors (Poulikakos et al., 2011). Overexpression of another RAS isoform CRAF or other MAPK kinases such as TPL2/COT, in addition to mutations in MEK have also been proposed as resistance mechanisms (Emery et al., 2009; Johannessen et al., 2010; Montagut et al., 2008; Wagle et al., 2014). RAS-mediated mechanisms of re-activation can also promote resistance such as through acquisition of activating NRAS mutations (Nazarian et al., 2010) or by loss of RAS negative regulator neurofibromin (NF1), which facilitates the hydrolysis of GTP to GDP

(Nissan et al., 2014; Whittaker et al., 2013).

Combination of BRAF mutant inhibitors with inhibitors of its downstream target MEK have been effective in restoring sensitivity from MAPK reactivation and prolonging patient response (Eroglu and Ribas, 2016; Flaherty et al., 2012). This combination also helps reduce the occurrence of secondary skin lesions caused by paradoxical activation of MAPK signaling and hyper-proliferation in cells with wild-type BRAF protein (Su et al., 2012). With the improved patient response rates and survival compared to BRAF inhibitor monotherapy, the BRAF and MEK inhibitor combination therapy is the standard-of-care for targeted therapy treatment in BRAF mutant melanomas (Eroglu and Ribas, 2016; Luke et al., 2017).

Melanoma dedifferentiation in MAPK inhibitor cross-resistance

Resistance can also occur through MAPK pathway independent mechanism through upregulation of receptor tyrosine kinases (RTKs), which result in broad pathway inhibition resistance. RTKs such as the epidermal growth factor receptor (EGFR), platelet-derived growth factor receptor β (PDGFRβ), and insulin-like growth factor receptor (IGFR) (Girotti et al., 2013; Nazarian et al., 2010; Paraiso et al., 2014; Villanueva et al., 2010) have been found to be upregulated in resistance. High levels of RTKs are also indicative of a dedifferentiated melanoma transcriptional state, characterized by low levels of MITF and melanocytic genes (Konieczkowski et al., 2014a; Müller et al., 2014). As with acquired resistance, this dedifferentiation transcriptional state is associated with intrinsic cross-resistance to multiple MAPK pathway inhibitors targeting BRAF, MEK, and ERK (MAPKi). Accordingly, MITF loss and RTK upregulation has been observed in patient tumors during disease progression on MAPKi therapy (Konieczkowski et al., 2014a; Müller et al., 2014; Tirosh et al., 2016). Dedifferentiation was also found to be associated with an NF-κB high transcriptional state, observed in both cell lines and patient tumors (Konieczkowski et al., 2014a). Induction of NF-κB signaling by treatment with TNFα was able to promote dedifferentiation and MAPKi resistance. This therapy

resistance was specific for the MAPK pathway as it does not rescue other cytotoxic drugs (Gray-Schopfer et al., 2007; Konieczkowski et al., 2014a). The receptor tyrosine kinase AXL was identified to be one of the best predictive markers for this dedifferentiated MAPKi resistant state and exhibited expression patterns highly inversely correlated with MITF. AXL over-expression itself was sufficient to confer resistance, however there is mixed reports on the efficacy of combinatorial therapy with AXL inhibitors (Konieczkowski et al., 2014a; Müller et al., 2014).

Melanoma dedifferentiation in immunotherapy resistance

The dedifferentiation response of melanoma to inflammatory signaling also has implications in immunotherapy. Melanoma is among the most highly mutated cancers, likely due to the accumulation of UV-induced DNA damage from sun exposure of the skin (Alexandrov et al., 2013). The increased immunogenicity through mutated antigens provides an explanation for the immune infiltrates commonly found within tumors by histopathological analysis (Thomas et al., 2013). The presence of immune infiltration is significantly associated with improved outcome in patients, which underscores the therapeutic value of an active immune response (Akbani et al., 2015; Bogunovic et al., 2009; Fridman et al., 2012; Jönsson et al., 2010; Thomas et al., 2013). The importance of the immune response and formation of “memory” is especially evident in the long-lasting results that can be achieved by immunotherapy (Hodi et al., 2010; Larkin et al., 2015; Robert et al., 2015; Rosenberg et al., 2011). Immunotherapies that restore anti-tumor T cell immunity such as adoptive cell transfer of exogenously re-activated T cells (Rosenberg et al., 2011) and immune checkpoint blockade inhibitors targeting CTLA-4 and PD-1/PD-L1 have been able to remarkably achieve durable responses in patients (Hodi et al., 2010; Larkin et al., 2015; Robert et al., 2015).

Analysis of epitopes recognized by tumor-infiltrated lymphocytes isolated from patient tumors had identified that melanocyte lineage antigens were those frequently recognized

(Brichard et al., 1993; Kawakami et al., 2000). Therefore, dedifferentiation of melanoma cells could provide a means of immune evasion by down-regulating the expression of melanocytic antigens recognized by CD8+ T cells. This has been demonstrated in a mouse model of melanoma with tumors expressing the melanocytic antigen gp100, and adoptive cell transfer (ACT) of CD8+ T cells from transgenic pmel-1 mice expressing a gp100 specific T-cell receptor (Landsberg et al., 2012). In this model, there was an initial strong tumor regression demonstrating the immune response and efficacy of ACT therapy. However, the tumors relapsed with hypomelanotic areas, pro-inflammatory cytokine expression, and loss of the gp100 antigen. Thus, dedifferentiation was able to promote immunotherapy resistance by altering the antigenic landscape to avoid immune recognition. Furthermore, inflammatory MITF-low melanomas were shown to have greater recruitment of myeloid cells (Riesenberg et al., 2015), which could support tumor growth or immune suppression (Hugo et al., 2015; Soudja et al., 2010).

Discussion

Advances in the field of tumor biology and immunology have led to new treatment approaches that significantly prolong survival and improve patient outcome. However, melanoma cells are highly plastic, with the ability to switch differentiation states during resistance to both targeted and immune therapies. Low baseline levels of MITF and high levels of AXL arise from acquired resistance and are predictive of intrinsic resistance to broad MAPK pathway inhibition (MAPKi). A high MITF differentiated state is also important for immune recognition as melanocytic lineage proteins can serve as tumor-associated antigens recognized by CD8+ T cells (Kawakami et al., 2000). This collective impact of differentiation state and plasticity on current melanoma therapies highlights the importance of further understanding melanoma differentiation. In this study, we propose that melanoma cells span a differentiation spectrum that can be divided into four subtypes and include a transient neural crest

transcriptional program. This refinement of the differentiation program combined with pharmacogenomics analyses guided us in the discovery of vulnerability to iron-dependent oxidative stress associated with dedifferentiation than can be used to overcome resistance.

CHAPTER 1:

Melanoma subtypes based on multi-stage differentiation

INTRODUCTION

Analysis of tumor transcriptional profiles has enabled the discovery of shared molecular features and tissue cell type-based classification defining subtypes predictive of survival, response to therapy, and such work has aided in guiding rational treatment strategies (Alizadeh et al., 2000; Perou et al., 2000; Sotiriou and Pusztai, 2009; Verhaak et al., 2010). In melanoma, molecular classification of cell lines revealed two dominant phenotypes that were predictive of metastatic potential and independent of mutation status (Hoek et al., 2006). The “proliferative” phenotype expressed higher levels of the melanocyte lineage transcription factor MITF and differentiation markers. The “invasive” phenotype is less differentiated with slower proliferation but demonstrates greater motility. Subsequent studies have found that these phenotypic classifications have significant prognostic value in terms of the response to MAPK pathway inhibitors (MAPKi). The low MITF invasive phenotype cells were generally more resistant to MAPKi, consistently expressed high levels of the receptor tyrosine kinase (RTK) AXL, and were associated with an inflammatory transcriptional state (Konieczkowski et al., 2014b; Müller et al., 2014).

Multiple studies have shown that these transcriptional states are not fixed, as melanoma cells are also known to exhibit dynamic plasticity with the capacity to dedifferentiate and switch between phenotypes with therapy resistance and pro-inflammatory signaling (Landsberg et al., 2012; Müller et al., 2014). The differentiation plasticity of melanoma could have its origins from the embryonic history of melanocytes, which are derived from the neural crest, a transient, migratory, and multi-potent population of cells that can differentiate into diverse cell types (Sauka-Spengler and Bronner-Fraser, 2008). With dedifferentiation, neural crest markers such as the neural growth factor receptor NGFR has been found to be upregulated in therapy

resistance (Fallahi-Sichani et al., 2017; Landsberg et al., 2012; Titz et al., 2016).

In this study, we take advantage of the relative purity of a cohort of equivalently derived melanoma cell lines to refine the melanoma classification and to relate them to stages of melanocyte differentiation. As cell lines do recapitulate much of the gene expression patterns in patient tumors, a cell line guided analyses enables identification of specific melanoma intrinsic subtypes. Our approach reveals that melanoma cells span a two-dimensional spectrum of four differentiation-related subtypes and this spectrum also reflect a cellular trajectory that cells traverse through during phenotype switching in therapy resistance.

RESULTS

Melanoma Cell Line and Tumor Gene Expression is Highly Concordant

To test the similarity between melanoma cell lines and bulk tumors, we compared the maximum expression of each gene within skin cutaneous melanoma (SKCM) tumors (n=470) from The Cancer Genome Atlas (TCGA) against that from a panel of 53 human melanoma cell lines, including paired acquired resistance sub-lines, established from patient biopsies. There was a strong concordance (R=0.87) between bulk tumor and cell line gene expression, demonstrating how well cell lines retain tumor expression patterns (Figure 1-1). The residual disparity is mostly from genes expressed higher in tumors than in cell lines. Included within these genes were highly immune-specific CD markers and response genes encoding cytokines, cytotoxic molecules, and complement components, reflecting immune infiltration within at least a subset of tumors. Additionally, a number of keratinocyte-type stratified epithelial keratin genes such as keratin pairs KRT1/KRT10, and KRT5/KRT14 (Moll et al., 2008) were found highly expressed in tumors, demonstrating the presence of normal skin-associated tissue from the biopsy site of origin in some cases.

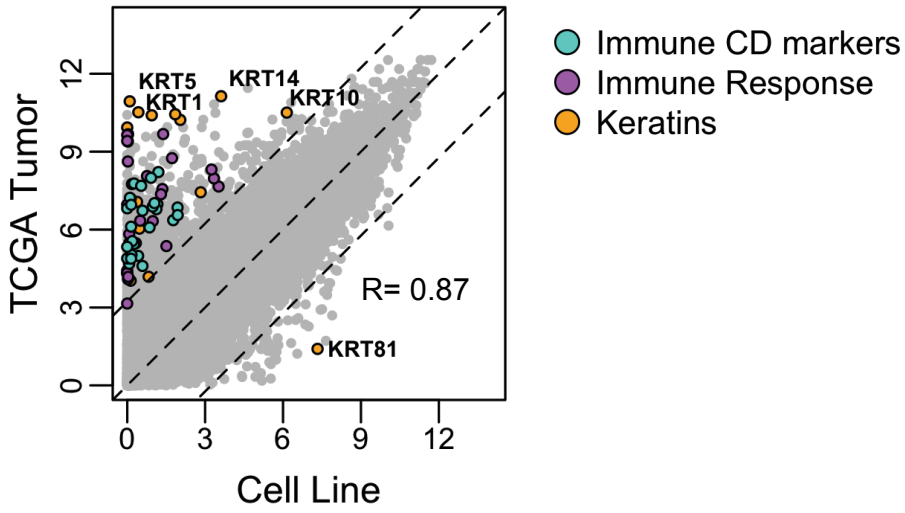

Figure 1-1. Melanoma cell line and tumor expression profiles are highly concordant. Scatterplot of maximum gene expression in the melanoma bulk tumors and cell lines show strong concordance. Maximum expression was defined as the 95th percentile value to reduce the effects of outliers. Dashed lines represent two standard deviations from the diagonal.

Melanoma Subtypes Reflect Four Progressive Differentiation States

Consensus hierarchal clustering (Monti et al., 2003) of the expression profiles from the panel of 53 human melanoma cell lines revealed that cell lines fall robustly into four clusters numbered C1-C4 with no appreciable gain in cluster stability when increasing to higher numbers of clusters (Figure 1-2A, Figure 1-2B). We next evaluated every combination of cluster pairs using SigClust (Liu et al., 2008) and found each cluster to be significantly different from one another (Figure 1-2C). Additionally, all of the clusters arranged into distinct groups by principal component analysis (PCA) (Figure 1-2D). The cell lines and their respective annotations can be found in Table 1-1 and Table 1-2.

We next investigated how our four melanoma clusters were related by differentiation. We performed a comparative analysis to a human *in vitro* model of melanocyte differentiation (Mica et al., 2013) where human embryonic stem (ES) cells were induced to differentiate sequentially to neural crest, melanoblast, and melanocyte stages. PCA of these differentiation stage gene expression profiles, which included primary melanocytes as a reference control, showed that each stage segregated progressively along a two-dimensional arc-like trajectory with differentiation. Projection of the melanoma cell lines onto the same melanocyte differentiation stage-defined PCA space similarly separated out the four identified melanoma clusters, indicating a progressive four-stage differentiation relationship (Figure 1-3A).

Enrichment analysis of the gene expression signal-to-noise ratios for each cluster compared with the remaining three clusters showed a progressive pattern of differentiation-related enrichment of Gene Ontology biological process terms and guided the naming of the subtypes (Figure 1-3B). C1 was defined as the undifferentiated subtype due to enrichment for invasive phenotype gene sets such as those involving cell adhesion and migration, in addition to inflammation-related gene sets as observed previously in dedifferentiated low MITF melanoma cells (Hoek et al., 2006; Konieczkowski et al., 2014b). C2 was defined as the neural crest-like subtype due to enrichment for neural crest-related gene sets. As a generally dedifferentiated

subtype, the neural crest-like subtype shared enrichment for the characteristic invasive/inflammation-related gene sets. C3 was defined as the transitory subtype, due to concurrent enrichment of neural crest and pigmentation associated gene sets, suggesting a transitional or mixed neural crest to melanocytic state. Finally, C4 is the most differentiated and was defined as the melanocytic subtype, due to loss of a neural crest signature and a strong enrichment for pigmentation-associated gene sets.

We next explored the expression patterns of transcription factors and RTK genes across the identified melanoma subtypes (Figure 1-4A). As expected, the undifferentiated and neural crest-like subtypes both had low levels of *MITF* and high levels of *AXL*. In addition, SMAD3 was elevated in these two subtypes, suggesting a role for TGFβ signaling with the invasive phenotype as previously described (Hoek et al., 2006; Rodeck et al., 1999). These two subtypes do have some notable differences. In the undifferentiated subtype, we observed significantly lower levels of *ERBB3*, neural crest marker *NGFR*, and transcription factor *SOX10*. As *SOX10* is a critical neural crest lineage specifying transcription factor essential for melanocyte development (Sauka-Spengler and Bronner-Fraser, 2008), its absence is further supportive of an even less differentiated state. Genes upregulated in the undifferentiated subtype include *SOX9* and *EGFR*, both of which have been shown to be promoted by SOX10 loss (Shakhova et al., 2012; Sun et al., 2014) . The transitory and melanocytic subtypes are a refinement of the previously reported differentiated proliferative phenotype, characterized by higher expression of *MITF* and lower expression of *AXL*. Wnt/beta-catenin signaling has been implicated in enhancing MITF target gene expression, and an increased expression of beta-catenin (*CTNNB1*) is observed across these two subtypes in support of a more mature melanocyte signature (Schepsky et al., 2006). To evaluate the differential MITF activity between these two subtypes, we performed enrichment analysis using previously described MITF target genes to infer activity (Hoek et al., 2008a). The melanocytic subtype showed stronger enrichment of these MITF target genes (Figure 1-4B), supportive of greater differentiation within this subtype.

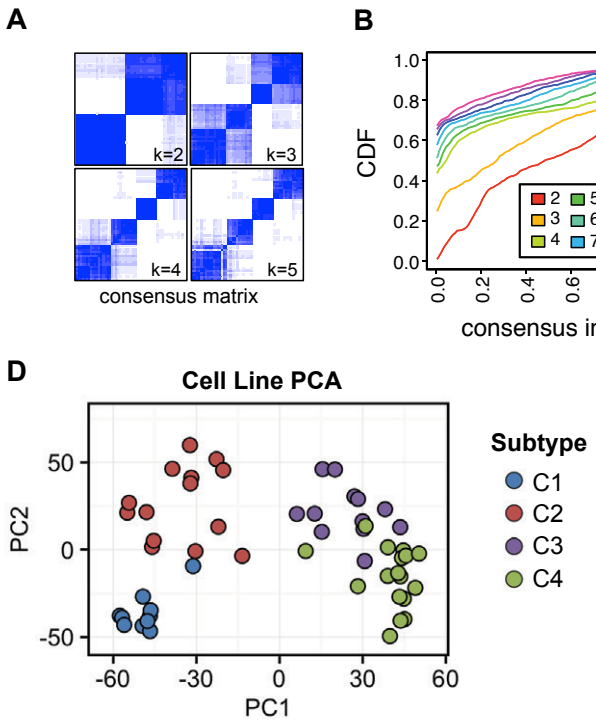

	C1	C2	C3	C4
C1				
C2	3.26E-36			
C3	1.29E-47	3.64E-50		
C4	7.11E-58	8.44E-67	5.23E-30	

Figure 1-2. Identification of four melanoma subtypes. (A) Consensus hierarchical clustering of melanoma cell lines identifies four robust clusters. (B) Cumulative distribution function (CDF) plot reflecting four as the optimal number of clusters. (C) Pairwise comparisons using SigClust showing that the cluster delineations are statistically significant. (D) PCA of melanoma cell line expression profiles annotated by identified clusters.

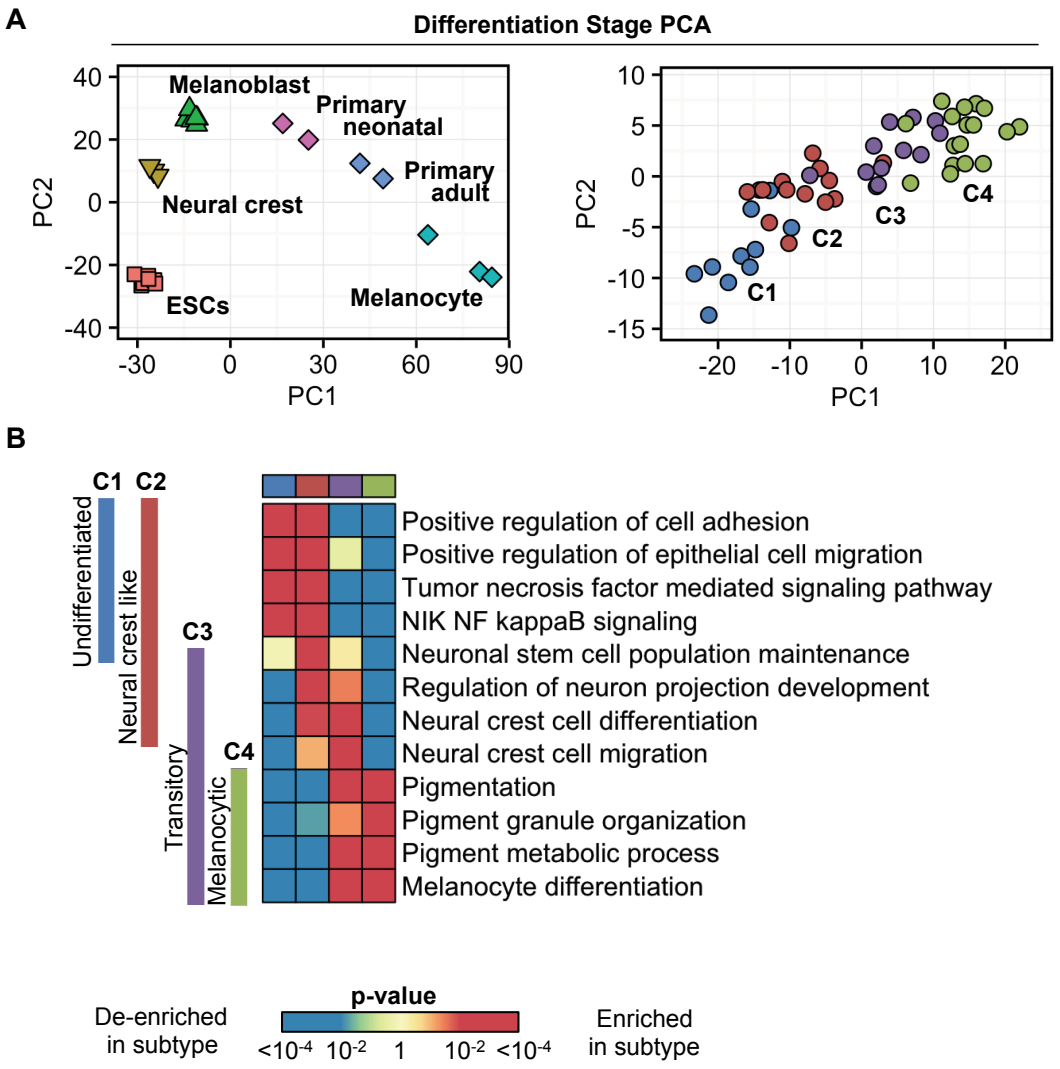

Figure 1-3. Melanoma subtypes are related by progressive differentiation. (A) PCA of gene expression profiles from an *in vitro* embryonic stem cell (ESC) to melanocyte multi-stage differentiation system (top) and projection of melanoma cell line expression profiles into melanocyte differentiation stage PCA space show progressive separation of clusters (bottom). (B) Heatmap of rank-based enrichment analysis p-values of each individual cluster vs. the remaining clusters showing progressive enrichment patterns of differentiation-associated gene ontology (GO) gene sets.

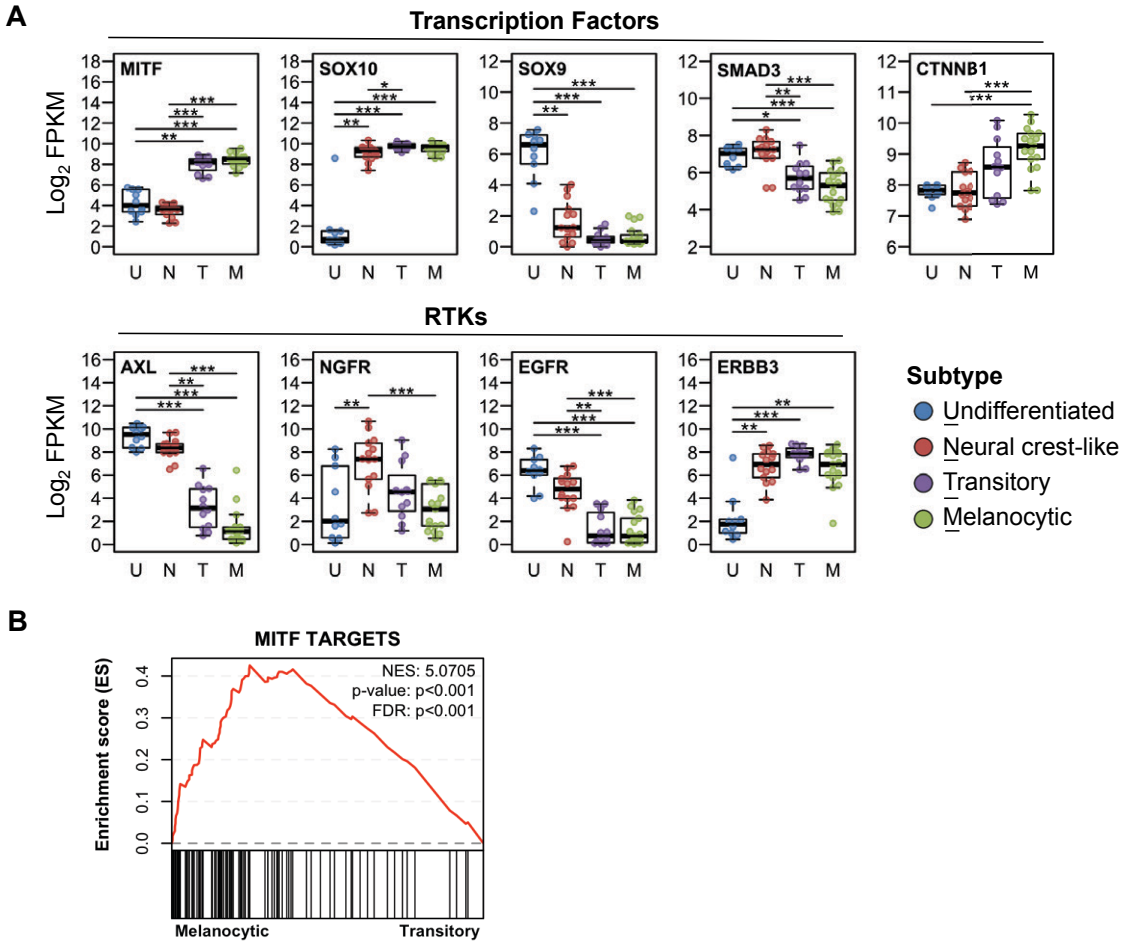

Figure 1-4. Expression patterns of transcription factors and receptor tyrosine kinases across melanoma subtypes. (A) Boxplots of select transcription factors and receptor tyrosine kinase (RTK) genes in cell line expression profiles showing their subtype-specific patterns. (U: Undifferentiated, N: Neural crest-like, T: Transitory, M: Melanocytic; number in each group: U=10, N=42, T=12, M=17; Kruskal-Wallis ANOVA and Dunn's post hoc test p-values: * ≤ 0.05, ** ≤ 0.01, *** ≤ 0.001). (B) Enrichment analysis of Melanocytic vs. Transitory subtypes to infer MITF activity in cell lines using an independently identified list of MITF target genes.

Melanoma differentiation subtypes are consistent with and unify other independent cell line classifications

We next looked for commonality between our clusters to other independently identified melanoma cell line classifications (Hoek et al., 2006; Dugo et al., 2015) using the tool SubMap subtype comparison tool (Hoshida et al., 2007). In the classification by Hoek *et al*, three cohorts A, B, and C were consistently observed by hierarchical clustering but the strongest transcriptional signatures were found in Cohort A and Cohort C, which defined the "proliferative" and "invasive" phenotype respectively. Comparison of these cohorts with our identified subtypes shows informative mapping relationships for all cohorts, with the melanocytic subtype (C4) mapped to Cohort A, the transitory subtype (C3) mapped to both Cohort A and B, and both the undifferentiated and neural crest-like subtype mapped (C1-C2) mapped to Cohort C (Figure 1-5A). In an independent set of melanoma cell lines, Dugo *et al* identified three subtypes that also refined the invasive phenotype into two subclasses with differential ERBB3 and EGFR levels. Our subtypes again map informatively to all three subtypes, with the transitory and melanocytic (C3-C4) mapping to the Proliferative $EGFR^{LOW}ERBB3^{HIGH}$, the neural crest-like subtype mapping to the Invasive $EGFR^{LOW}ERBB3^{HIGH}$, and the undifferentiated subtype mapping to the Invasive $EGFR^{HIGH}ERBB3^{LOW}$ (Figure 1-5B). These results show that our clusters are consistent with independent analysis from the literature and importantly unify other subtype reports, which were previously not fully concordant or not understood in a differentiation context.

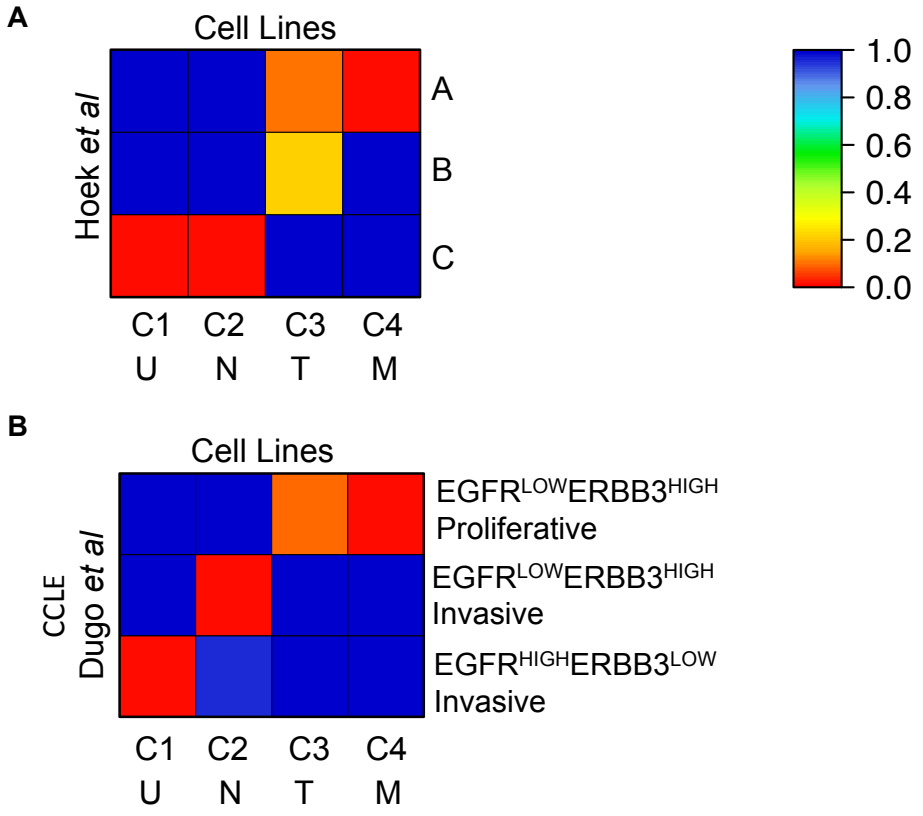

Figure 1-5. Comparison to independent datasets show subtype-specific overlap with previous classifications and MITF signatures. (A-B) Submap analysis comparing the four identified melanoma subtypes to the Hoek *et al.* cohorts (A) and Dugo *et al.* subtypes (B).

Four-Stage Differentiation Model Reflects Treatment-Induced Step-wise Dedifferentiation

Our results demonstrate that melanoma cells can exist at distinct baseline differentiation states. As melanoma cells are highly plastic and can dedifferentiate in response to MAPK pathway inhibition and pro-inflammatory signaling from immunotherapy, we sought to relate these treatment-induced differentiation transitions to our subtypes. We first defined transcriptional signatures that would allow us to distinguish each subtype. For each signature, differentially upregulated genes specific to each subtype were determined using a log2 fold change threshold of 1.5 and 5% false discovery rate. Additionally, since our subtypes were related by progressive differentiation states as proposed above, we tested the extent of shared differentially expressed genes between 'adjacent' subtypes compared to other subtype pairings. Highly consistent with our interpretation of the subtypes as four progressive differentiation states, the only cluster pairings that generated an appreciable signature were between sequential clusters in the two-dimensional arc-like trajectory model (Figure 1-6).

We applied these signatures to investigate RTK-upregulated, dedifferentiation-associated acquired resistance to MAPK pathway inhibitors (Müller et al., 2014). To quantify the degree of treatment-induced dedifferentiation, we calculated a differentiation trajectory position score for each sample using a "center of mass" approach that reflects the relative position along the differentiation trajectory where the sample has the strongest gene expression signature match. The difference between each sample from its respective control in the calculated score thus represents the magnitude and direction of change in differentiation. In the BRAF mutant cell lines M229P and M238P, we observed that cell lines begin with different initial differentiation stages as defined by their subtype signatures, but shift notably towards the undifferentiated signature upon acquired resistance to vemurafenib (M229R, M238R) (Figure 1-7). As a negative control, resistance mediated by genomic alterations that directly reactivate the MAPK pathway, such as through *NRAS* mutation (M249R) or *BRAF* alternative splicing (M395R, M397R) do not show differentiation changes (Nazarian et al., 2010).

To evaluate the temporal changes that occur with the acquisition of resistance, we performed a vemurafenib treatment time-course study using the M229 parental cell line, which starts as a transitory subtype but switches to an undifferentiated subtype in M229R. Supportive of our differentiation model, treatment with vemurafenib produced gene expression changes with time that marked progressive dedifferentiation through our subtype signatures towards the undifferentiated subtype (Figure 1-8). We also observed similar temporal changes of dedifferentiation in an additional melanoma cell line, M397, which has an acquired resistant subline through MAPK pathway re-activation by BRAF alternative splicing (M397R) (Figure 1-7, Figure 1-8A). These routes of acquired resistance are not mutually exclusive, as dedifferentiation can be a transient response of adaptive resistance as previously observed by us and others (Fallahi-Sichani et al., 2017; Ravindran Menon et al., 2014; Sun et al., 2014; Titz et al., 2016). Thus, an adaptive phase could allow evolution of resistant clones with genetic mechanisms that enable return to the parental differentiation signature. Alternately, the dedifferentiation signature can be stabilized, such as through loss SOX10 by epigenetic reprogramming in BRAF inhibition resistant clones (Shaffer et al., 2017).

Since current treatment strategies for targeted therapy includes both BRAF and MEK kinase inhibition, we applied our four-stage differentiation model to an independent study of RTK-driven single and double drug (BRAFi and MEKi) resistant cell lines (Figure 1-9). We again find similar dedifferentiation patterns towards the undifferentiated subtype signature in both single and double drug resistance. In patient tumor biopsies, there are multiple mechanisms of multiple resistance mechanisms that contribute to heterogeneous responses in patient samples. This diversity has been reported in tumors, where different resistance mechanisms were found within the same patient and even within the same lesion (Allen et al., 2014; Hugo et al., 2015; Shi et al., 2014). Additionally, both low and high MITF cells can be present in the same patient tumors at varying degrees (Eichhoff et al., 2010; Hoek et al., 2008b; Tirosh et al., 2016). Therefore, patient tumor-based results will tend to reflect the overall

heterogeneity of melanoma therapeutic response. Nevertheless, within the heterogeneity of patient tumors, our subtype signatures were also able detect dedifferentiation in patient biopsies on-treatment (Figure 1-10) or upon disease progression (Figure 1-11A) on double drug MAPK therapy (Hugo et al., 2015; Kwong et al., 2015; Tirosh et al., 2016). As expected, in a comparison across a panel of patient biopsies at disease progression, tumors with established MAPK re-activation resistance mechanisms do not exhibit dedifferentiation changes from baseline at relapse (Figure 1-11B).

We next applied our subtype signatures to investigate immunotherapy resistance occurring through inflammation-induced dedifferentiation. Such dedifferentiation has been shown to occur *in vivo* in a mouse model of adoptive cell transfer (ACT) using transgenic cytotoxic T cells targeting the melanocytic antigen gp100 (Landsberg et al., 2012). Dedifferentiation decreased tumor antigen presentation, as scored by loss of melanocytic biomarkers (gp100, TRP2), and resulted in tumor progression. As expected, we observed greater expression of dedifferentiation signatures within the relapse group compared to the control both in the tumors and in tumor-derived cell lines (Figure 1-12). Collectively, these results demonstrate that our differentiation framework is consistent with and can semi-quantitatively reflect dedifferentiation associated with current melanoma therapy resistance.

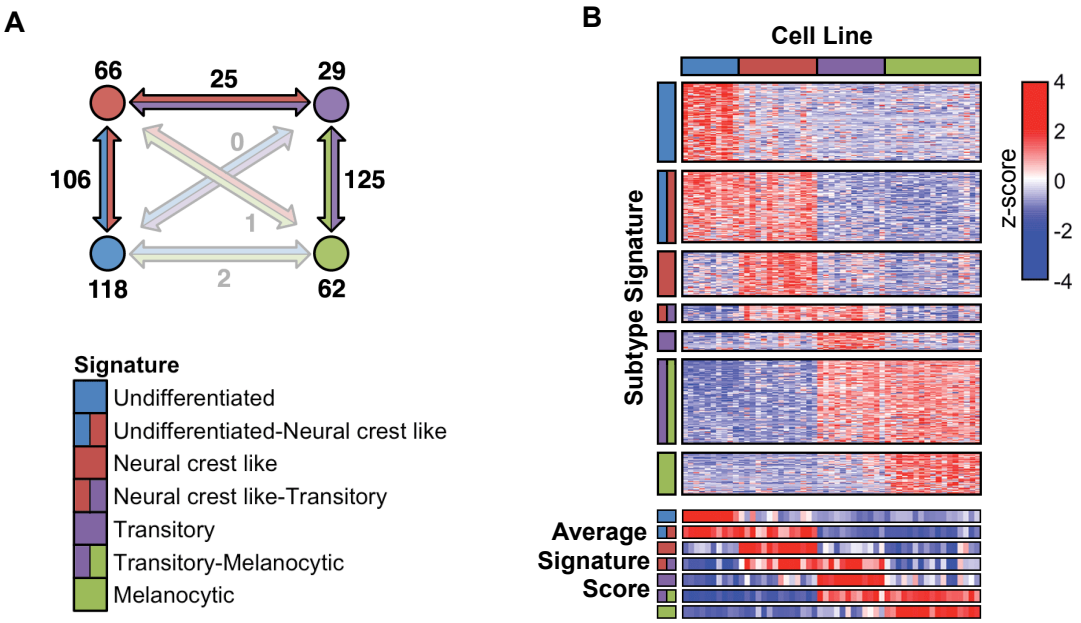

Figure 1-6. Identification of subtype signatures for scoring and visualization of treatment-induced dedifferentiation. (A) Numbers of differentially upregulated genes in each individual subtype or shared between pairs of subtypes when compared to the remaining subtypes (log_2 fold change ≥ 1.5, 5% false discovery rate). (B) Heatmap of subtype gene signatures in cell line gene expression profiles. Average of each subtype signature z-score are shown at the bottom.

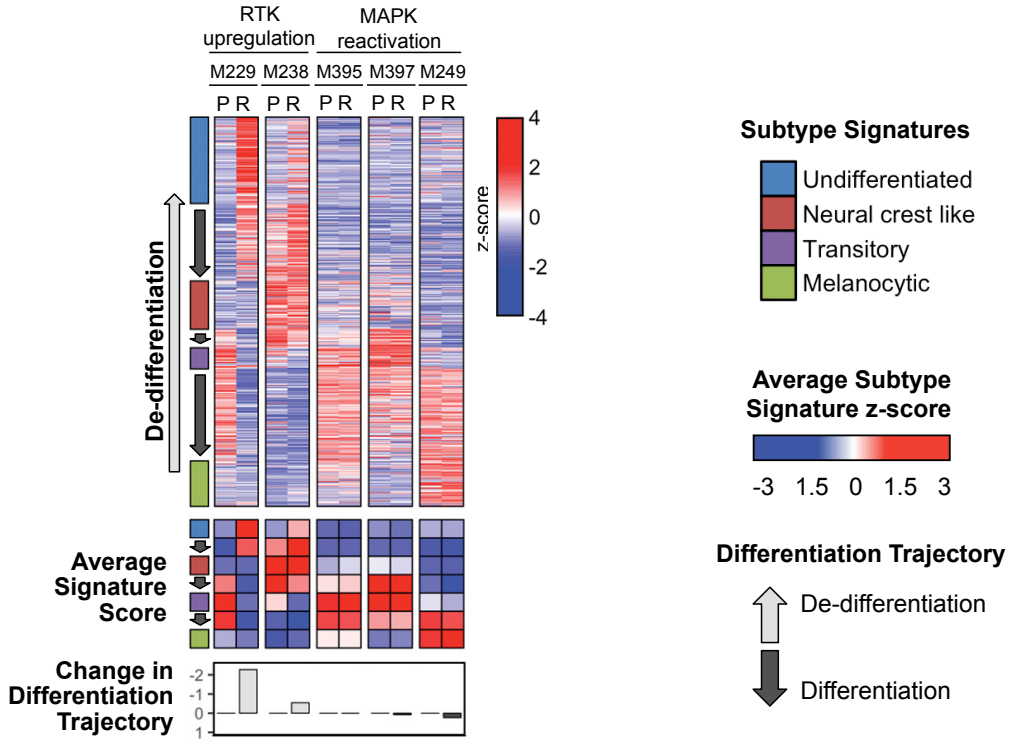

Figure 1-7. RTK upregulation mechanism of BRAFi acquired resistance show subtype transitions towards dedifferentiation. Heatmap of signature genes (top), average signature z-scores (middle), and differentiation trajectory position changes (bottom) in matched parental and resistant cell lines with different indicated mechanisms of vemurafenib acquired resistance.

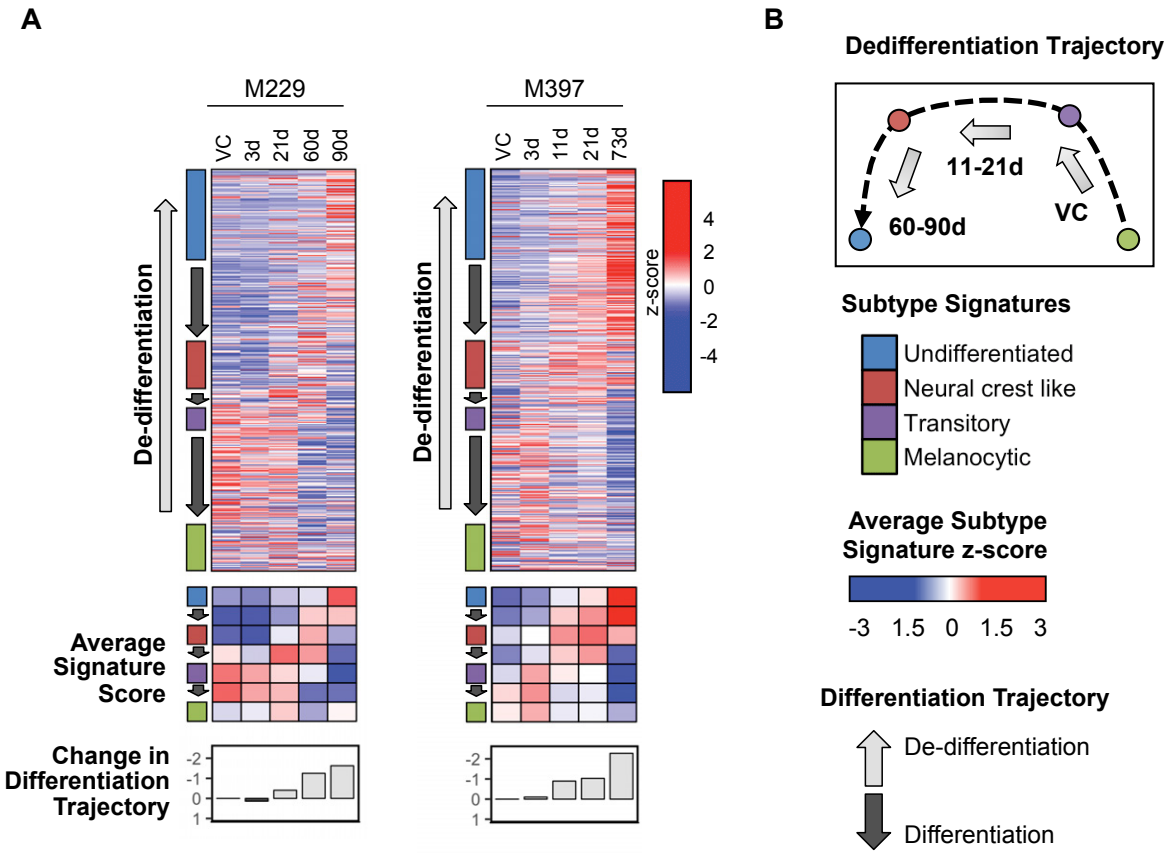

Figure 1-8. BRAF inhibition induces step-wise dedifferentiation towards acquired resistance. (A) Heatmap of signature genes (top), average signature z-scores (middle), and differentiation trajectory position changes (bottom) in a time-course of M229 and M397 melanoma cell line treated with vemurafenib compared to DMSO vehicle control. (B) Schematic representing progressive dedifferentiation along our two-dimensional trajectory model with increased treatment time with vemurafenib.

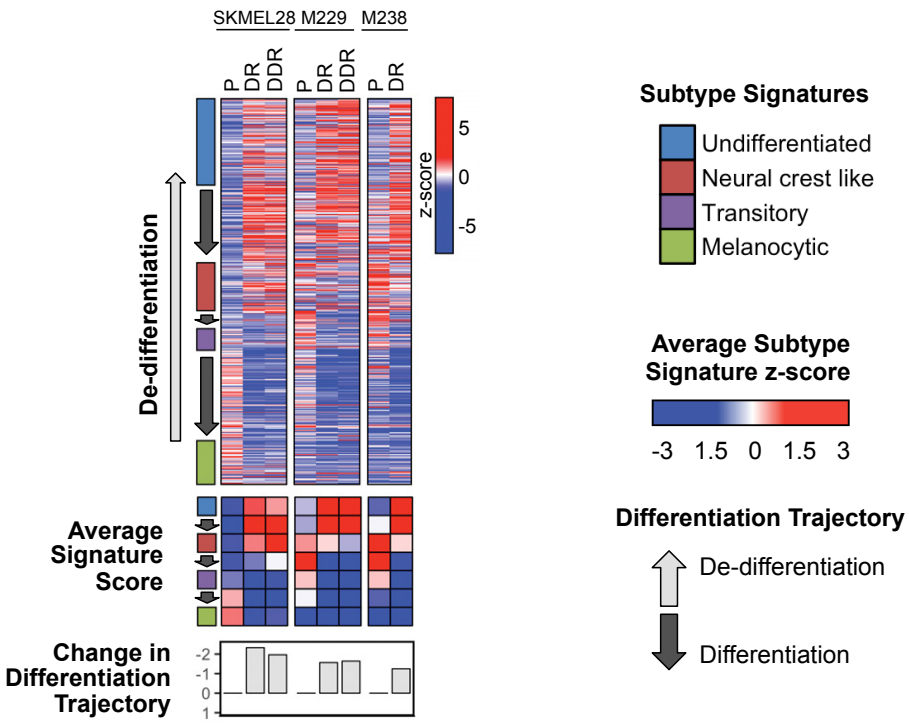

Figure 1-9. Single and double drug MAPKi acquired resistance show subtype signature transitions towards dedifferentiation. Heatmap of signature genes (top), average signature z-scores (middle), and differentiation trajectory position changes (bottom) in matched parental (P) or single drug resistant (DR) or double drug resistant (DDR) samples of the three indicated cell lines. DR: vemurafenib (BRAFi); DDR: vemurafenib + selumetinib (MEKi).

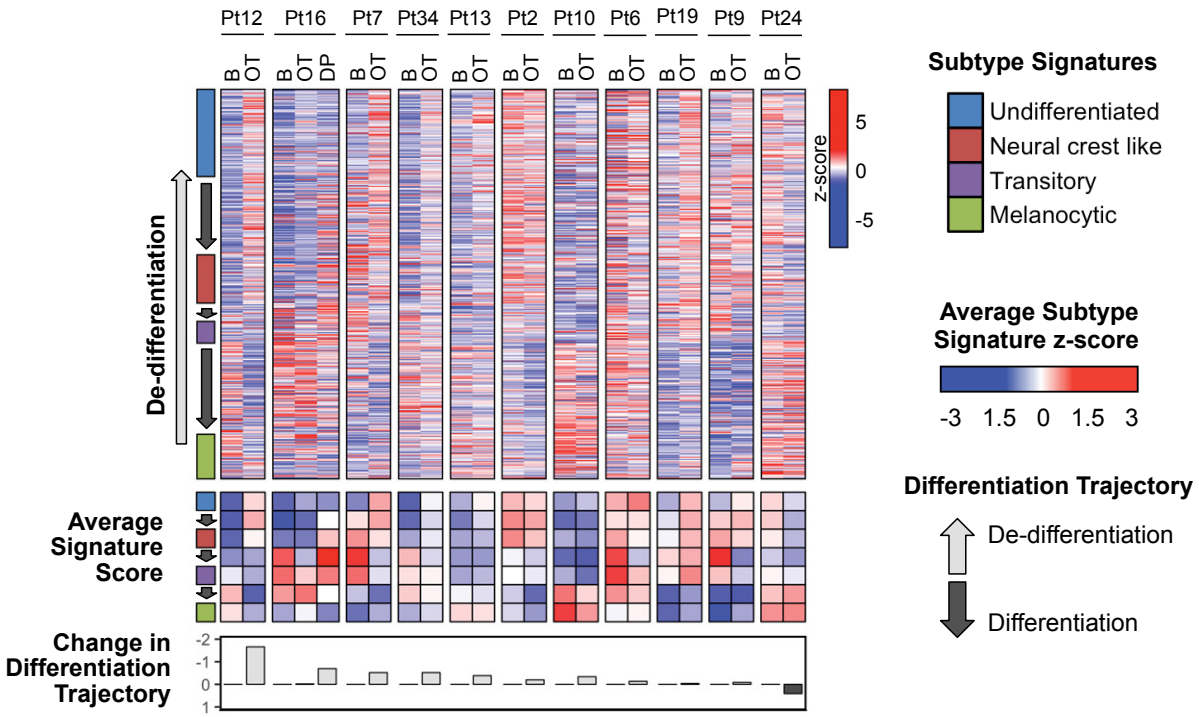

Figure 1-10. Tumor biopsies of patients on MAPKi treatment show dedifferentiation transitions. Heatmap of signature genes (top), average signature z-scores (middle), and differentiation trajectory position changes (bottom) in tumors from 11 patients (Pt) at baseline, on-treatment, or disease progression (B, OT, DP). Patients were on double drug (dabrafenib + trametinib (BRAFi+MEKi)) therapy with the exception of Pt2 on single drug therapy (vemurafenib (BRAFi)). On treatment samples are 12 ± 5 days.

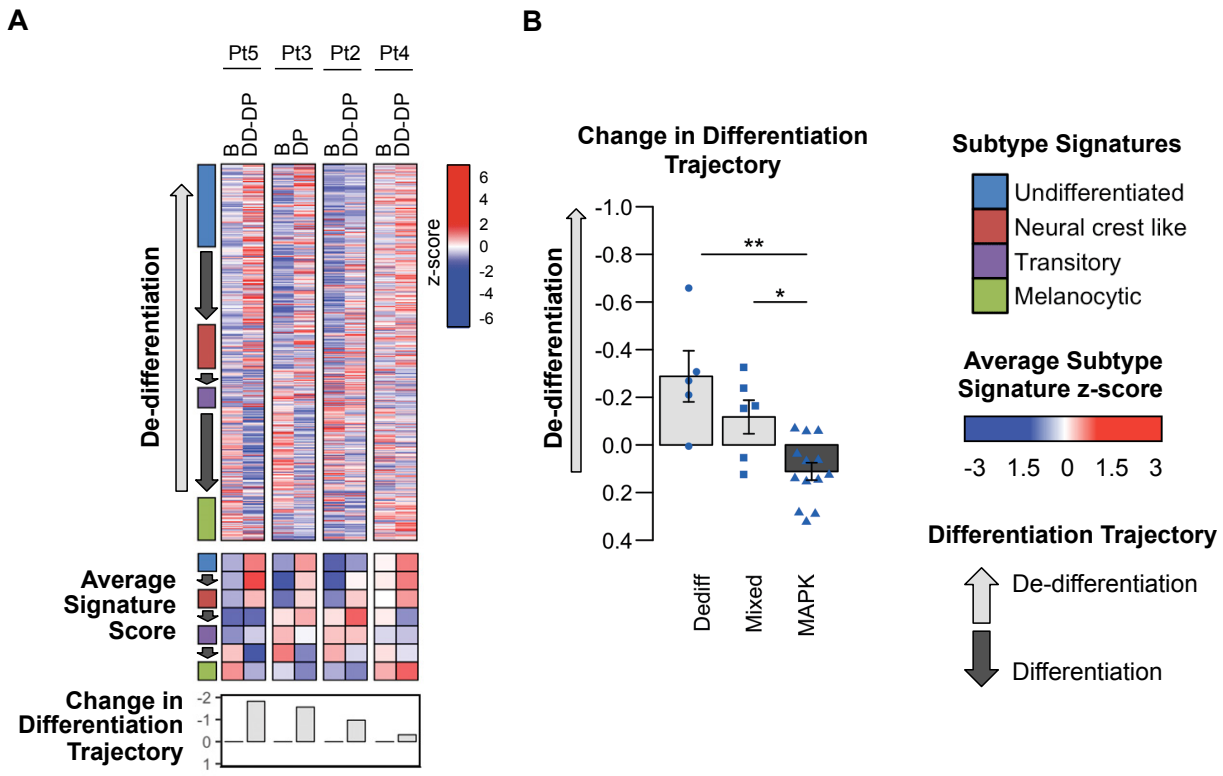

Figure 1-11. Tumor biopsies of patients at disease progression on MAPKi show dedifferentiation transitions. (A) Heatmap of signature genes (top), average signature z-scores (middle), and differentiation trajectory position changes (bottom) in 4 reported post-relapse tumors at baseline with statistically significant dedifferentiation at disease progression on double drug therapy (B: baseline, DD-DP: dabrafenib and trametinib therapy) (B) Comparison of changes in differentiation trajectory score of patient tumors with dedifferentiation, MAPK re-activation, or mixed dedifferentiation and MAPK reactivation markers upon disease progression on therapeutic RAF and/or MEK inhibition. Pairwise p-values: * ≤ 0.05, ** ≤ 0.01, overall Kruskal-Wallis p-value 0.002. For all panels, negative differentiation trajectory position changes reflect dedifferentiation.

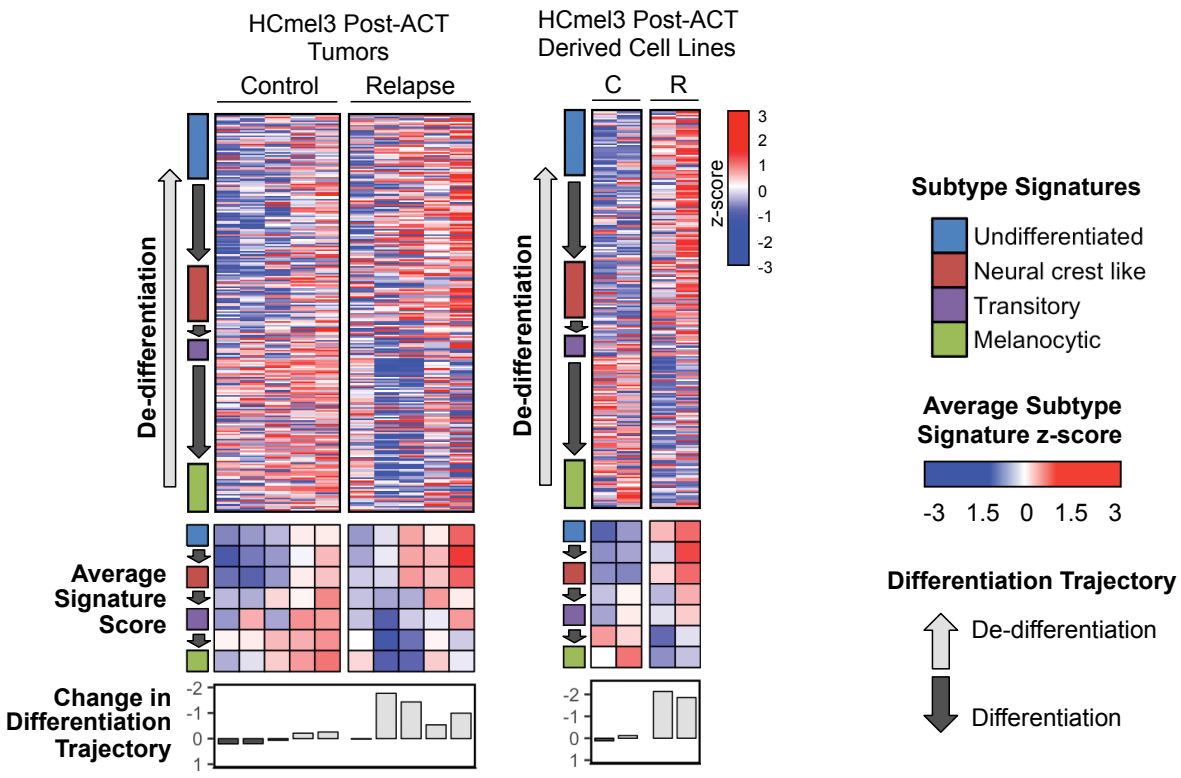

Figure 1-12. Immunotherapy-induced dedifferentiation in the context of the four-stage differentiation model. Heatmap of signature genes, average signature z-scores, and differentiation trajectory position changes for murine HCmel3 tumors or cell lines with treatment control or relapse from adoptive transfer of antigen specific T cells. Dark grey arrows represent increased differentiation state and the light grey arrow indicates the treatment induced dedifferentiation direction.

TABLE 1-1. Undifferentiated and Neural-crest like subtype cell lines

Cell Line	Mutation Status	Subtype
M407	BRAF mutant	Undifferentiated
M410	BRAF mutant	Undifferentiated
M257	Wild-type	Undifferentiated
M244	NRAS mutant	Undifferentiated
M296	NRAS mutant	Undifferentiated
M318	NRAS mutant	Undifferentiated
M381	BRAF mutant	Undifferentiated
M406	BRAF mutant	Undifferentiated
M229AR	BRAF mutant	Undifferentiated
Sbcl2	NRAS mutant	Undifferentiated
M233	BRAF mutant	Neural crest like
M243	NRAS mutant	Neural crest like
M245	NRAS mutant	Neural crest like
M238	BRAF mutant	Neural crest like
M370	BRAF mutant	Neural crest like
M409	BRAF mutant	Neural crest like
M423	NA	Neural crest like
M418	Wild-type	Neural crest like
M402	BRAF mutant	Neural crest like
M411	BRAF mutant	Neural crest like
M238AR	BRAF mutant	Neural crest like
M255	BRAF mutant	Neural crest like
M409AR	BRAF mutant	Neural crest like
M420	BRAF mutant	Neural crest like

TABLE 1-2. Transitory and Melanocytic subtype cell lines

Cell Line	Mutation Status	Subtype
M395	BRAF mutant	Transitory
M308	BRAF mutant	Transitory
M229	BRAF mutant	Transitory
M263	BRAF mutant	Transitory
M297	BRAF mutant	Transitory
M376	BRAF/NRAS double mutant	Transitory
M398	BRAF/NRAS double mutant	Transitory
M375	Wild-type	Transitory
M399	BRAF mutant	Transitory
M395AR	BRAF mutant	Transitory
M397	BRAF mutant	Transitory
M397AR	BRAF mutant	Transitory
M202	NRAS mutant	Melanocytic
M207	NRAS mutant	Melanocytic
M230	Wild-type	Melanocytic
M249	BRAF mutant	Melanocytic
M262	BRAF mutant	Melanocytic
M285	Wild-type	Melanocytic
M311	NRAS mutant	Melanocytic
M417	BRAF mutant	Melanocytic
M416	BRAF mutant	Melanocytic
M421	BRAF mutant	Melanocytic
M368	Wild-type	Melanocytic
M403	BRAF mutant	Melanocytic
M408	NRAS mutant	Melanocytic
M249AR	BRAF/NRAS double mutant	Melanocytic
M412a	NRAS mutant	Melanocytic
M412b	NRAS mutant	Melanocytic
PB	Wild-type	Melanocytic

DISCUSSION

Multiple studies have shown that melanoma cell lines and tumors can consistently be categorized into two phenotypic states based on differential levels of the transcription factor MITF. Classification of bulk tumors had identified subtypes that take into account the cells present in the microenvironment, however, our study is distinct in that we focused on identifying melanoma cell autonomous subtypes. We achieved this by taking a large cohort cell line approach, owing to the more homogeneous population and supported by the high concordance in gene expression observed between cell lines and tumors. There was published evidence of additional subtypes beyond the MITF-low and MITF-high phenotypes in cell lines (Dugo et al., 2015; Hoek et al., 2006), and importantly our results organize these findings into a unified description of four transcriptional subtypes that span a set of progressive differentiation states. Further supportive of this two-dimensional differentiation trajectory is the observation that melanoma cells de-differentiate progressively through these states with elapsed time under BRAF inhibitor treatment and accompanying acquisition of BRAFi resistance. We propose that changes in melanoma differentiation follow a progression through these four states in a two dimensional arc like trajectory.

Our identification of melanoma specific subtypes may also have important roles in immunohistochemical (IHC) diagnosis of melanoma. Poorly differentiated melanoma stain negative for melanocytic markers such as tyrosinase and MART-1, and thus have been a challenge to distinguish from other less differentiated cancer types. SOX10 has been used as a specific marker of cancers that arise from neural crest derived cells such as melanocytes (Ordóñez, 2014). NGFR, while not a melanocytic marker, has also been used to stain de-differentiated or desmoplastic melanomas that are negative for melanocytic antigens (Lazova et al., 2010). However, our refinement of de-differentiated “invasive” phenotype melanomas into two subtypes reveals that staining with SOX10 or

NGFR could result in lack of detection of melanoma cells from the more fully undifferentiated subtype. Therefore, our identification of the more fully undifferentiated subtype will guide the development of improved markers for this extreme de-differentiated phenotype.

Microenvironmental stresses such as inflammation, hypoxia, and treatment with MAPK inhibitors have been shown to induce de-differentiation and increase cell invasiveness (Landsberg et al., 2012; O'Connell et al., 2013). In the case of MAPK inhibition, it is possible that de-differentiation is an early adaptive mechanism for cells to survive, before genomic alterations such as NRAS mutations or BRAF amplifications take precedence, which can take a longer time to develop but provide a greater growth advantage under treatment. Our definition of four phenotypical subgroups of melanomas, matched with melanocyte development stages as well as associated with adaptation mechanisms of survival in melanoma, can guide discovery of combinatorial strategies to target dedifferentiation to overcome therapy resistance.

CHAPTER 2:

Melanoma differentiation subtype classifier identifies consistent subtypes in cell lines and tumors

INTRODUCTION

In the previous study, we refined the two “proliferative” and “invasive” differentiation phenotypes into a four-stage differentiation model. The melanoma cell intrinsic classifications of the MITF high “proliferative” and MITF low “invasive” phenotypes are very strong transcriptional signatures and have been detected in melanoma bulk tumor classification (Akbani et al., 2015; Verfaillie et al., 2015). However, it remains unexplored whether tumors can be reclassified into our four-group model that contains the more subtle transitional differentiation signatures.

In the past, direct molecular classification of melanoma tumor gene expression profiles have yielded subtypes that were inclusive of the non-melanoma cells within the bulk tumor such as immune and normal skin cells. (Akbani et al., 2015; Jönsson et al., 2010). These cells can be highly informative as investigating their roles in the microenvironment is important in understanding broad effects of therapy, immune function, and factors promoting metastasis. However, this can also mask more subtle differences in underlying cancer cell autonomous tumor biology. Since cancer cell lines still retain many of the properties of the original tumors (Masters, 2000), our molecular classification based on cell lines is a more homogeneous way to identify tumor-specific subtypes in the absence of cells in the microenvironment.

In this study, we apply a cell line-guided approach to classify melanoma tumors in the context of our differentiation framework. We build a predictive model to identify the differentiation subtypes in other cell line expression datasets and verify these subtype patterns among tumors. Finally, as an advantage of building this classifier, we harnessed matching methylation data paired with these datasets to evaluate methylation patterns that may be involved in regulating differentiation.

RESULTS

Melanoma Classifier Identifies Consistent Subtypes in Cell Lines

We first built a predictive model (Figure 2-1) trained on our cell line expression profiles to determine if we could predict differentiation subtypes in other cell line datasets. The predictive model was built using a support vector machine (SVM) classifier combined with the “top-scoring pairs” (TSP)-based method (Shi et al., 2011) to capture the relative expression relationship between genes. This approach ensured that different data sources, processing methods, and normalization strategies are compatible with our prediction model while minimizing test-set bias. We applied our prediction model to the Cancer Cell Line Encyclopedia (CCLE) and Genomics of Drug Sensitivity in Cancer (GDSC) independent datasets. Within the 29 cell lines shared between these two datasets, 27 were identically predicted (93.1%) and the other two only shifted by 1 stepwise differentiation state. PCA of each dataset annotated by the subtype prediction reveals a similar two-dimensional differentiation trajectory clustering pattern previously observed in the original analysis (Figure 2-2). Subtype-specific expression patterns of RTKs, transcription factors, and inferred MITF activity were also similar to that of the original cell line training data in the CCLE (Figure 2-3) and GDSC (Figure 2-4) datasets. Collectively, these results observed across independent melanoma cell line datasets further support the robustness of our classification model.

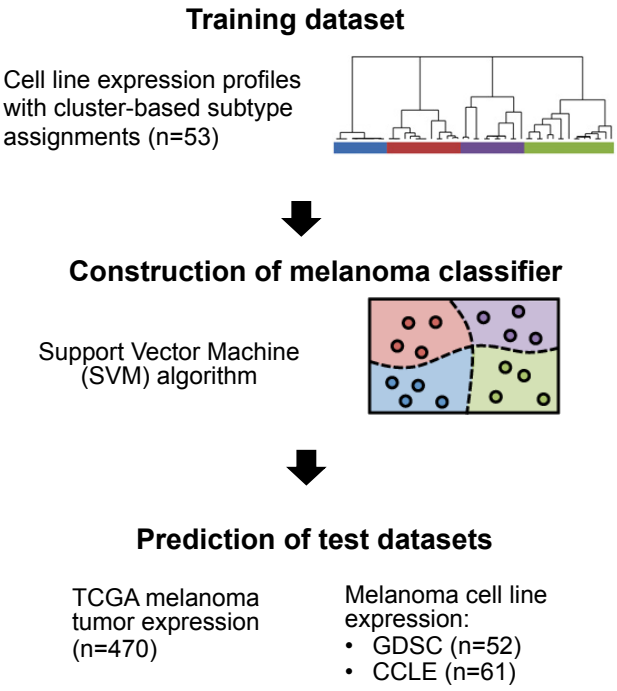

Figure 2-1. Schematic of the melanoma subtype classifier pipeline.

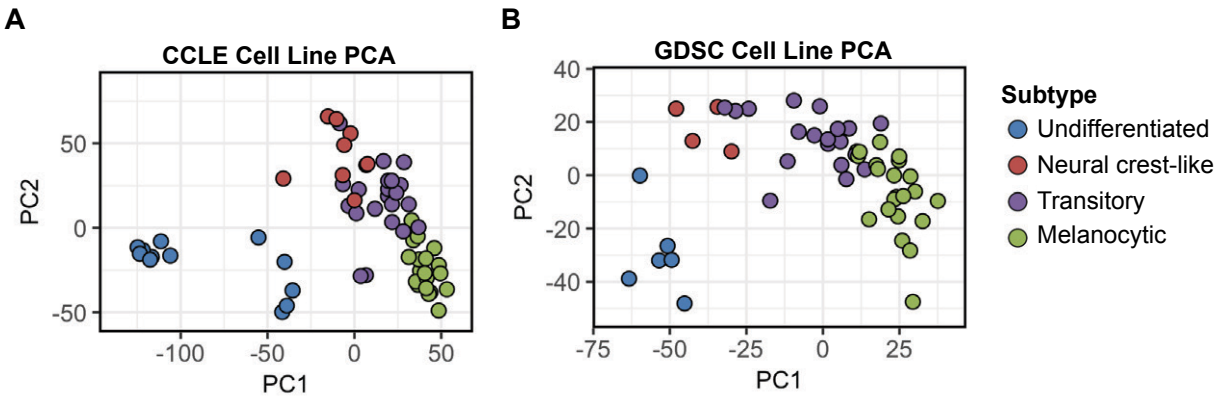

Figure 2-2. Subtype prediction of independent cell line datasets show similar differentiation-related arc-like clustering patterns. (A-B) PCA of CCLE (A) and GDSC (B) dataset annotated by the predicted cluster assignment.

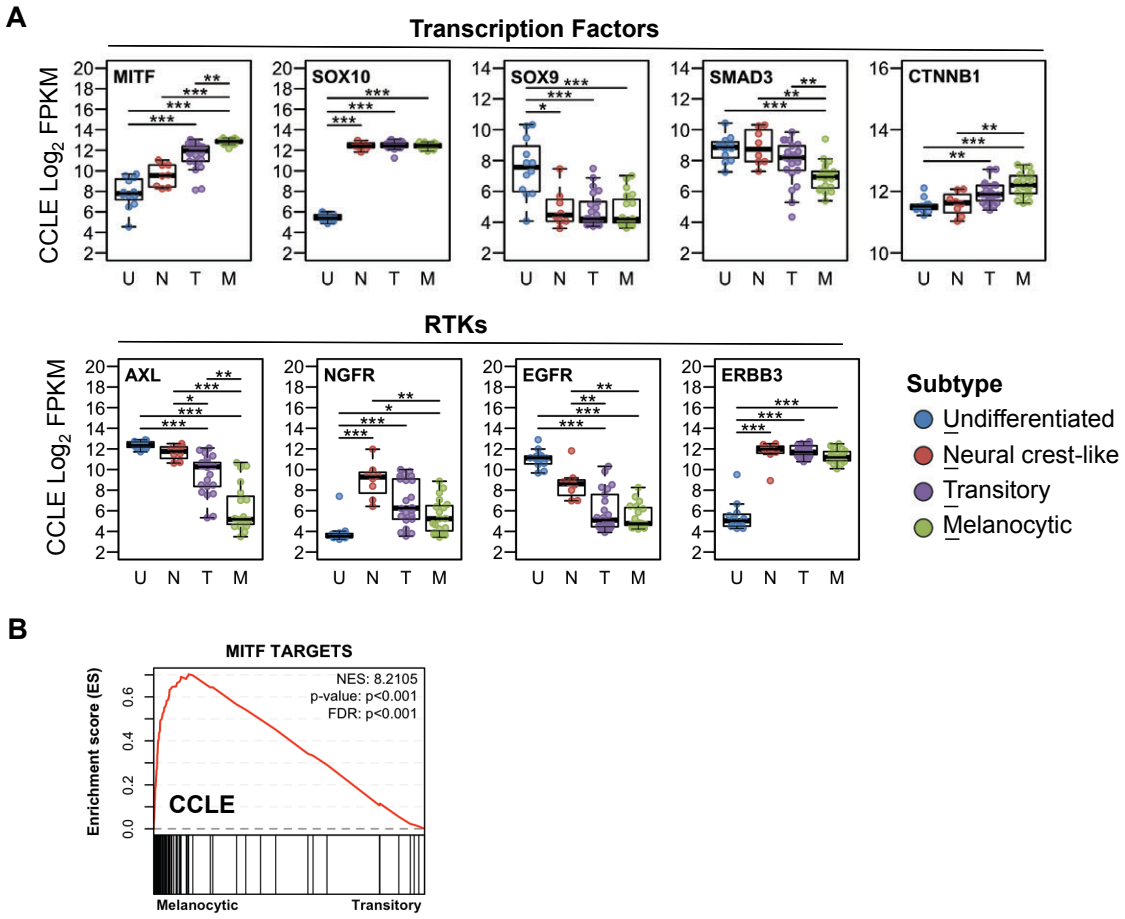

Figure 2-3. Subtype prediction of CCLE dataset show similar subtype-specific transcription factor and RTK expression patterns. (A) Boxplots of select transcription factors and RTK gene expression from the CCLE dataset showing subtype-specific expression patterns. (B) Enrichment analysis of Melanocytic vs. Transitory subtypes to infer MITF activity (U: Undifferentiated, N: Neural crest-like, T: Transitory, M: Melanocytic; number in each group: U=12, N=8, T=22, M=19; Kruskal-Wallis ANOVA and Dunn's post hoc test p-values: * ≤ 0.05, ** ≤ 0.01, *** ≤ 0.001).

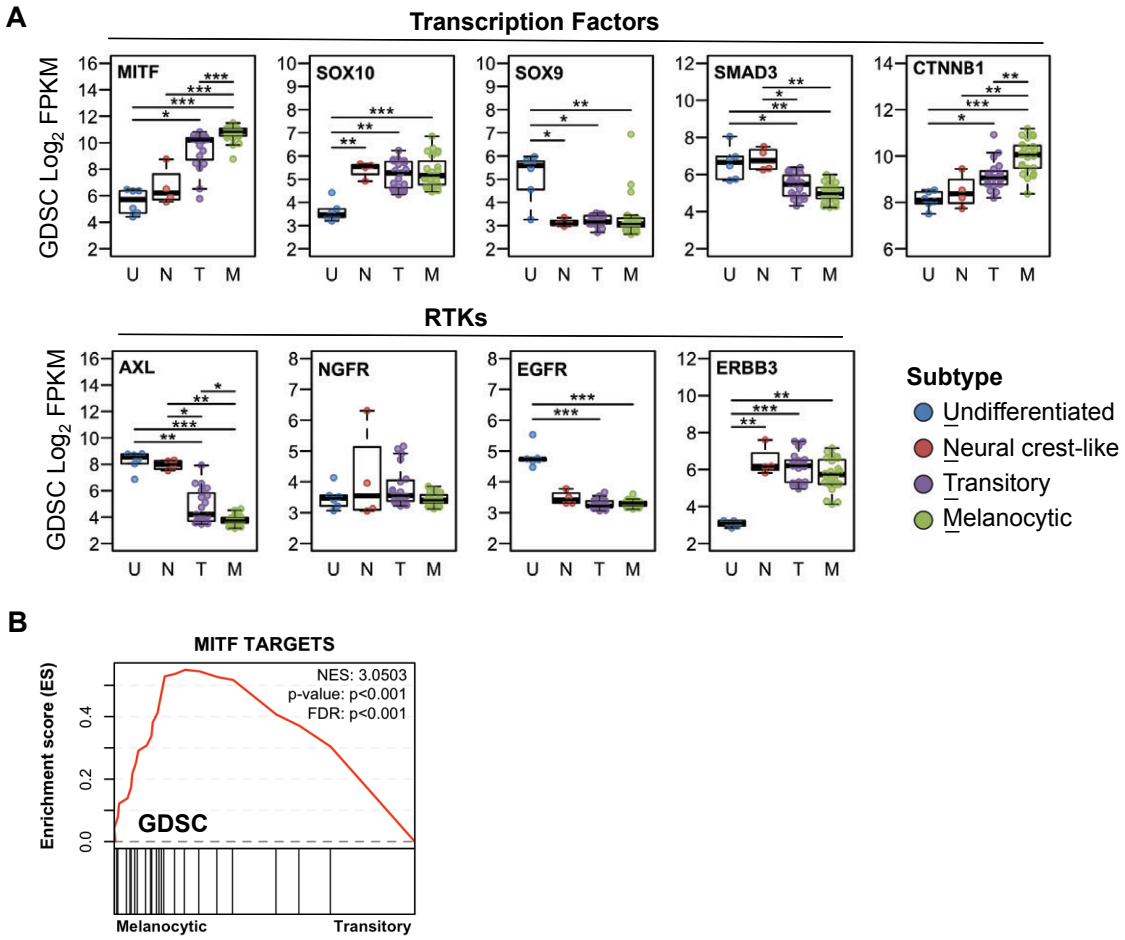

Figure 2-4. Subtype prediction of GDSC dataset show similar subtype-specific transcription factor and RTK expression patterns. (A) Boxplots of select transcription factors and RTK gene expression from the GDSC dataset showing subtype-specific expression patterns. (B) Enrichment analysis of Melanocytic vs. Transitory subtypes to infer MITF activity. (U: Undifferentiated, N: Neural crest-like, T: Transitory, M: Melanocytic; number in each group: U=6, N=4, T=19, M=23; Kruskal-Wallis ANOVA and Dunn's post hoc test p-values: * ≤ 0.05, ** ≤ 0.01, *** ≤ 0.001).

Melanoma Classifier Identifies Consistent Subtypes in Tumors

To evaluate the relevance of the subtypes in patient tumors, we extended our cell line-trained classifier to the TCGA skin cutaneous melanoma (SKCM) bulk tumor expression profiles for melanoma-specific sub-classification. As in the cell line cases, subtype-specific expression patterns of RTKs, transcription factors, and inferred MITF activity were also similar to that of the original cell line training data (Figure 2-5). However, PCA on the tumor gene expression profiles and annotated by its predicted subtype showed that while tumors in the same predicted subtypes generally cluster together, the overall patterns were distinct from the cell line cases (Figure 2-6A). This is likely due to the non-melanoma cells that contribute to the PCA-based summary of bulk tumor variance, as we observed a strong effect of immune infiltration using the T cell gene *CD3E* expression as a surrogate marker (Figure 2-6B). When we project the bulk tumor expression onto the PCA space rotations defined by the more controlled melanoma cell line training set, which now focuses on genes important to melanoma cell biology and decreases the bias from immune infiltration, we observed differentiation-related clustering patterns highly similar to that of cell line cases (Figure 2-7).

We next investigated if removal of confounding signatures could yield results similar to those seen in the cell line-guided PCA projections approach. Previously we had identified the source of the disparity between the melanoma cell line and bulk tumor gene expression was from immune cells and normal adjacent skin tissue within the tumor bulk. This was evident by high expression of immune-specific CD markers and cytokines indicative of immune infiltration and high expression of keratinocyte-type keratin pairs (*KRT1/KRT10* and *KRT5/KRT14*), which is found almost exclusively in stratified epithelia such as the epidermis (Moll et al., 2008). We first removed a set of immune reference genes previously annotated to be highly expressed in immune cells. We calculated an “immune score” across all tumors, which consisted of a dimension reduction of the set of immune reference genes, and removed additional genes that were correlated to this score. This approach helps further remove genes that could be

confounded by the presence of immune cells. PCA of the bulk tumor global gene expression profiles after removal of the immune-confounded genes re-oriented the clustering patterns of the subtypes (Figure 2-8A) by reducing the bias from immune infiltration (Figure 2-8B). Namely, tumors were now clustering together more similarly based on predicted subtype rather than level of immune infiltration. However, we now uncovered a secondary level of bias observed on PC2 from stratified epithelial signatures as measured by averaged expression levels of keratin pairs *KRT5/14* (Figure 2-8C). Expression of *KRT5/14* coincided with primary tumors as the source, suggesting that this high level of keratin gene expression is from adjacent skin (Figure 2-8D).

As in the immune case, we next removed skin-confounded genes using a starting reference set of keratin genes, generating a PCA-based keratin score, and then removing those genes correlated to the keratin score. PCA of the bulk tumor global gene expression profiles after removal of both the immune and keratin-confounded genes now markedly resembles the differentiation-related clustering patterns similar to that of the cell line guided PCA (Figure 2-9A). As confirmation, we observed a decreased bias from expression of normal adjacent skin (*KRT5/14*) (Figure 2-9B) and the tissue biopsy site on the PCA summary of variance (Figure 2-9C). Comparable results were also observed with an analogous approach of excluding primary tumor samples from the analysis, which further supports that the source of the keratin-confounded signature is from adjacent skin tissue (Figure 2-10). Taken together, our results demonstrate the consistency of these subtype relationships detectable in both melanoma cell line and tumor cohorts independently. Concordant subtype signatures could also be observed across all datasets, although with some heterogeneity in the patient tumors as expected (Figure 2-11).

To allow users to visualize other gene expression trends among the subtypes and within the bulk tumors in PCA space, we have created an interactive web-interface resource available at http://systems.crump.ucla.edu/dediff/ (username: melanoma_subtypes, password:

web_resource).

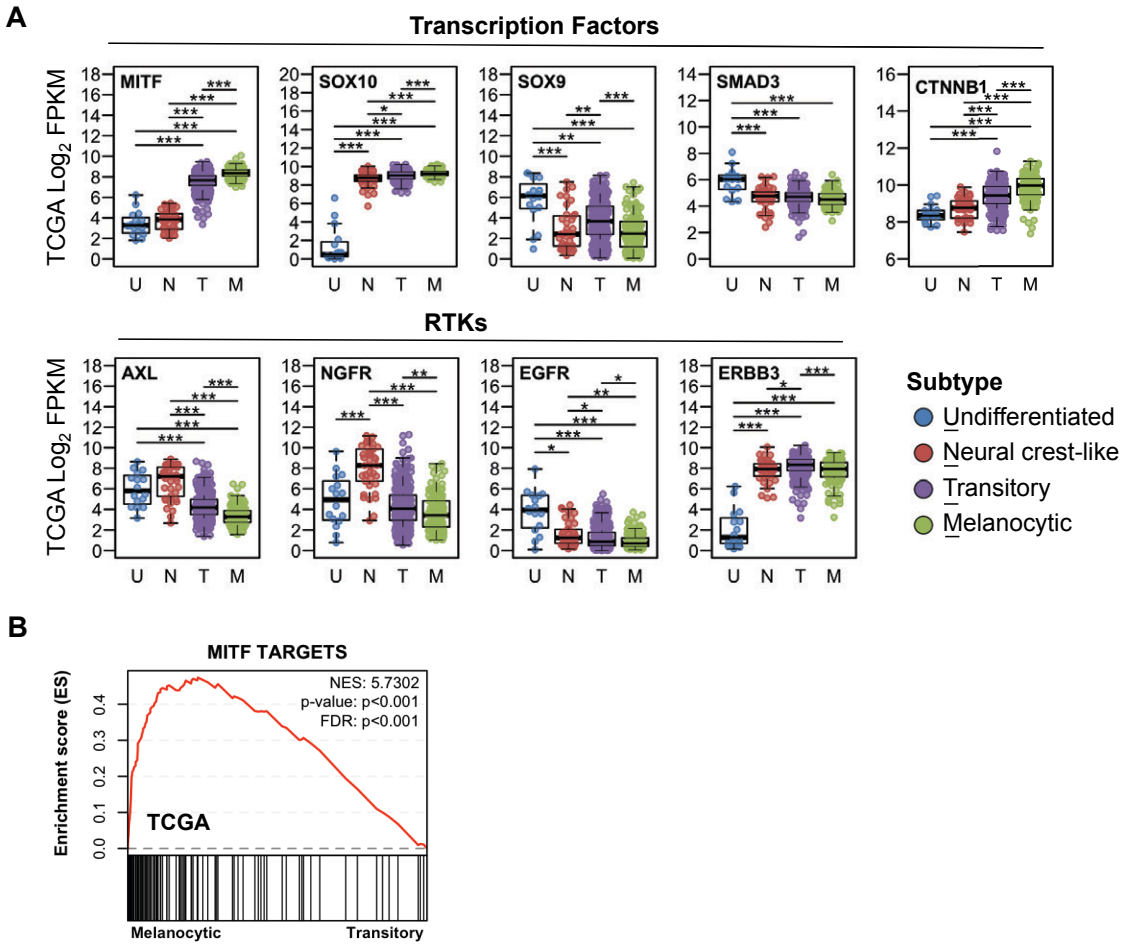

Figure 2-5. Subtype prediction of TCGA bulk tumor dataset show similar subtype-specific transcription factor and RTK expression patterns as cell lines.
(A) Boxplots of select transcription factors and RTK gene expression showing their subtype-specific patterns. (B) Enrichment analysis of Melanocytic vs. Transitory subtypes to infer MITF activity for CCLE. (U: Undifferentiated, N: Neural crest-like, T: Transitory, M: Melanocytic; number in each group, U=6, N=4, T=17, M=23; Kruskal-Wallis ANOVA and Dunn's post hoc test p-values: * ≤ 0.05, ** ≤ 0.01, *** ≤ 0.001).

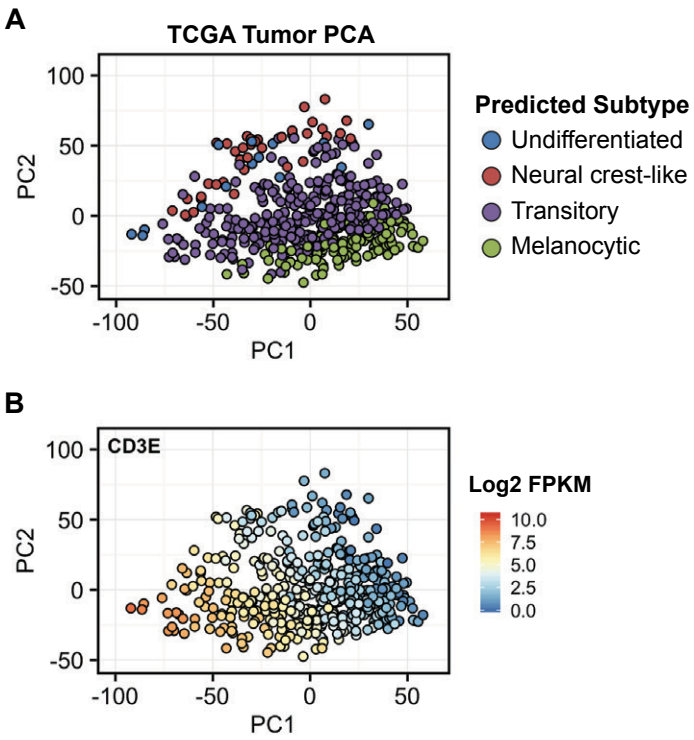

Figure 2-6. PCA of bulk tumor expression is influenced by immune infiltration. (A) PCA of bulk tumor global gene expression profiles annotated by predicted subtype for the original unfiltered dataset (B) PCA figure colored by CD3E expression to show the influence of immune infiltration.

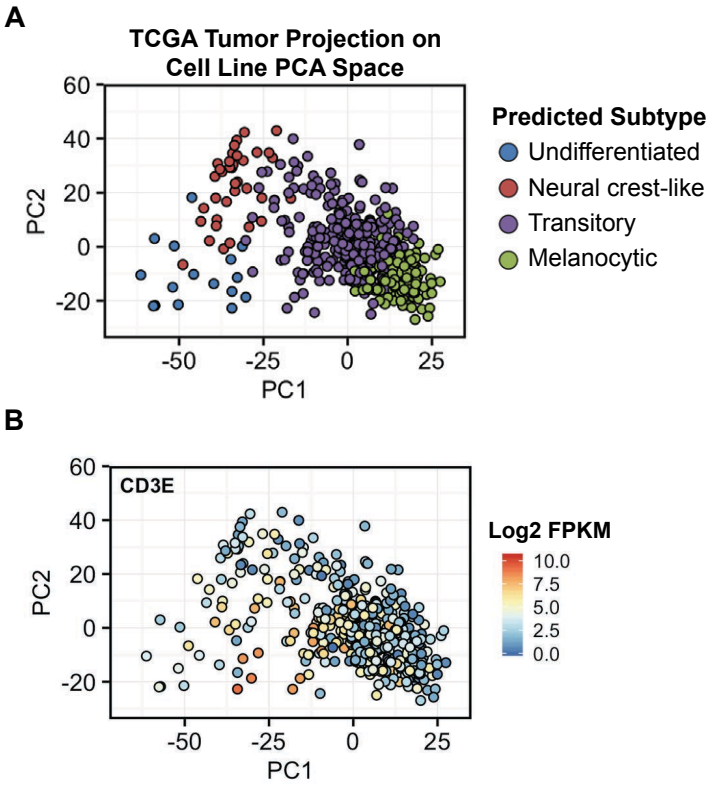

Figure 2-7. Cell line guided PCA projection of bulk tumor expression recapitulates differentiation-related arc-like clustering patterns. (A) Projection of bulk tumor expression profiles into melanoma cell line-based PCA space. (B) PCA figure colored by CD3E expression to show decreased influence of immune infiltration.

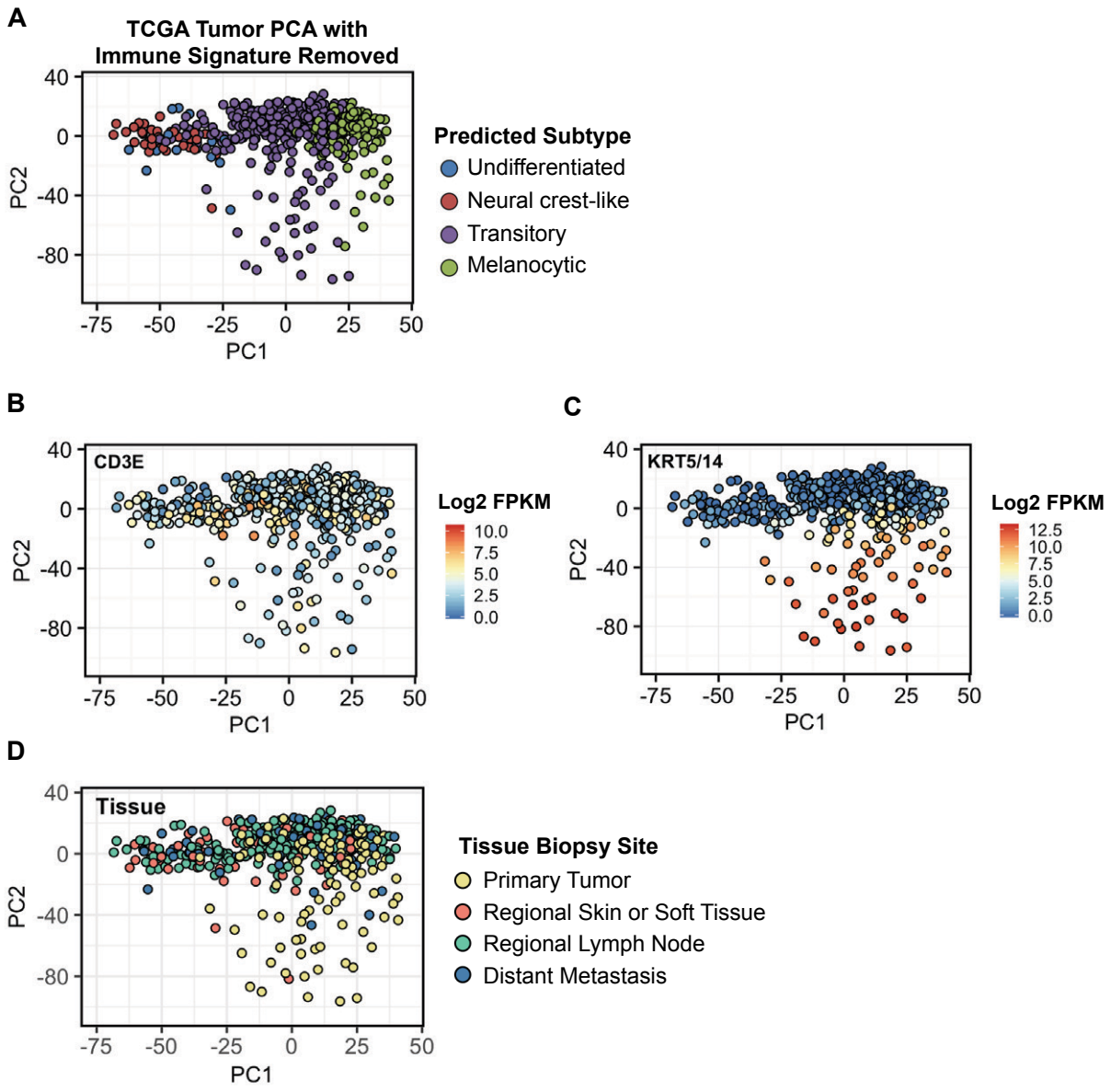

Figure 2-8. Removal of immune-confounded genes from bulk tumor analysis reveals an underlying keratin signature associated with primary samples. (A) PCA of bulk tumor global gene expression profiles after removal of confounding immune genes, and annotated by predicted subtype. (B-C) PCA figures colored by CD3E (B) expression to show the decreased influence of immune infiltration and KRT5/14 averaged expression (C) to show the influence of normal adjacent skin. (D) PCA figure annotated by tissue biopsy source.

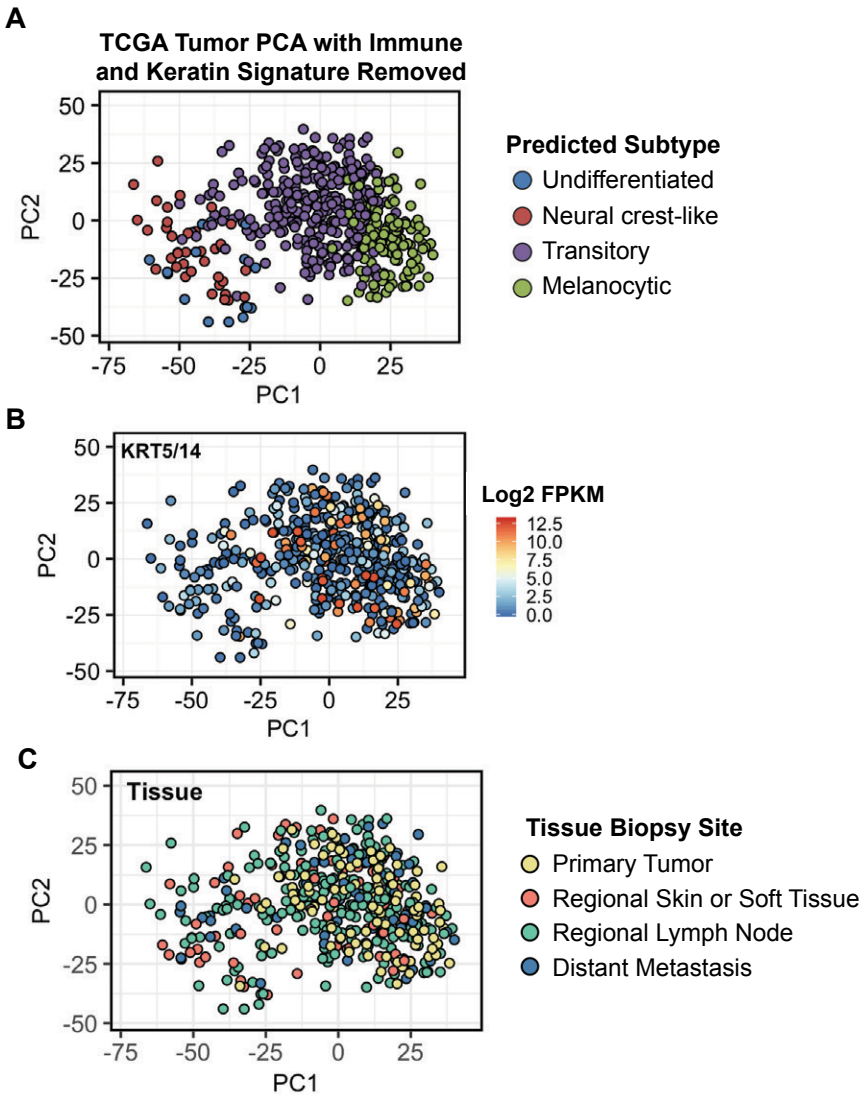

Figure 2-9. Removal of both immune and keratin-confounded genes from bulk tumor analysis reveals similar differentiation-related arc-like clustering patterns as cell lines. (A) PCA of bulk tumor global gene expression profiles after removal of both immune and keratin confounded genes, annotated by predicted subtype. (B) PCA figures colored by KRT5/14 averaged expression to show the decreased bias from stratified epithelial keratins. (C) PCA figure annotated by tissue biopsy source.

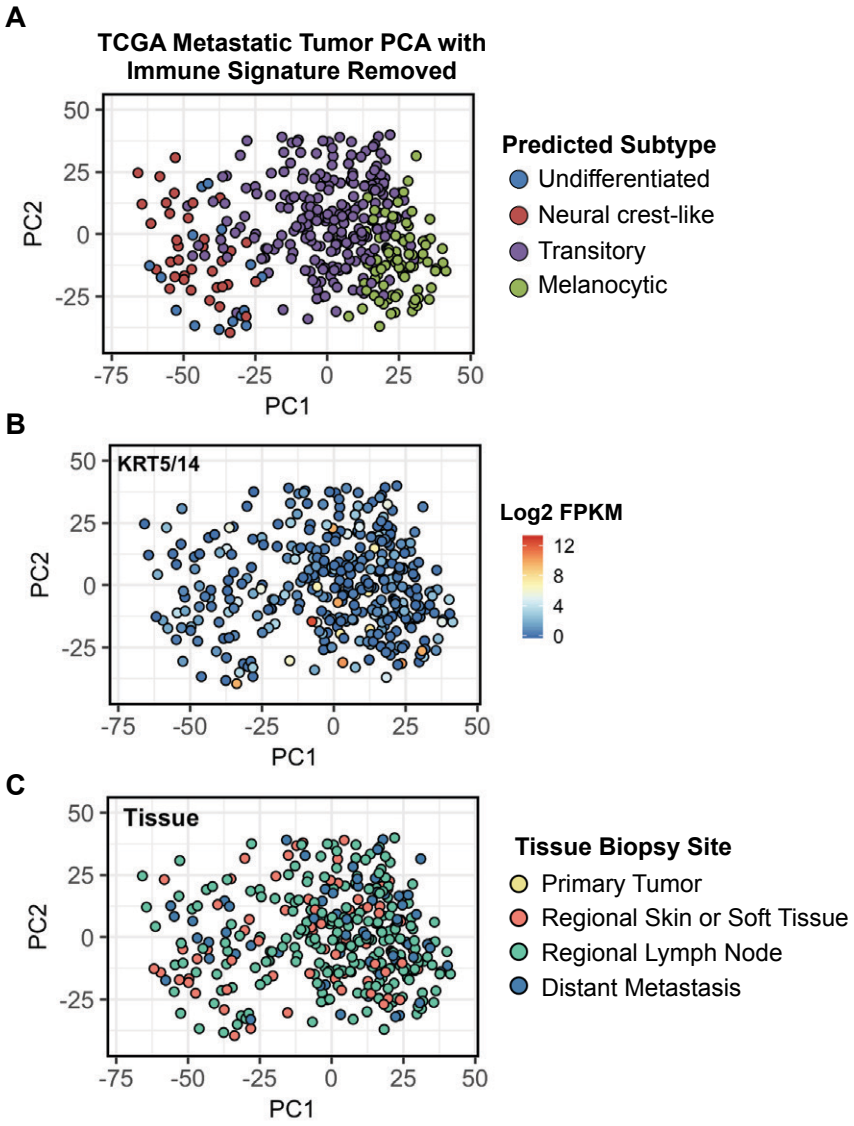

Figure 2-10. Exclusion of primary tumor samples from bulk tumor analysis yields similar results as removal of keratin-confounded genes. (A) PCA of only metastatic bulk tumor global gene expression profiles after removal of confounding immune genes, annotated by predicted subtype. (B) PCA figures colored by KRT5/14 averaged expression to show the decreased bias from stratified epithelial keratins. (C) PCA figure annotated by tissue biopsy source.

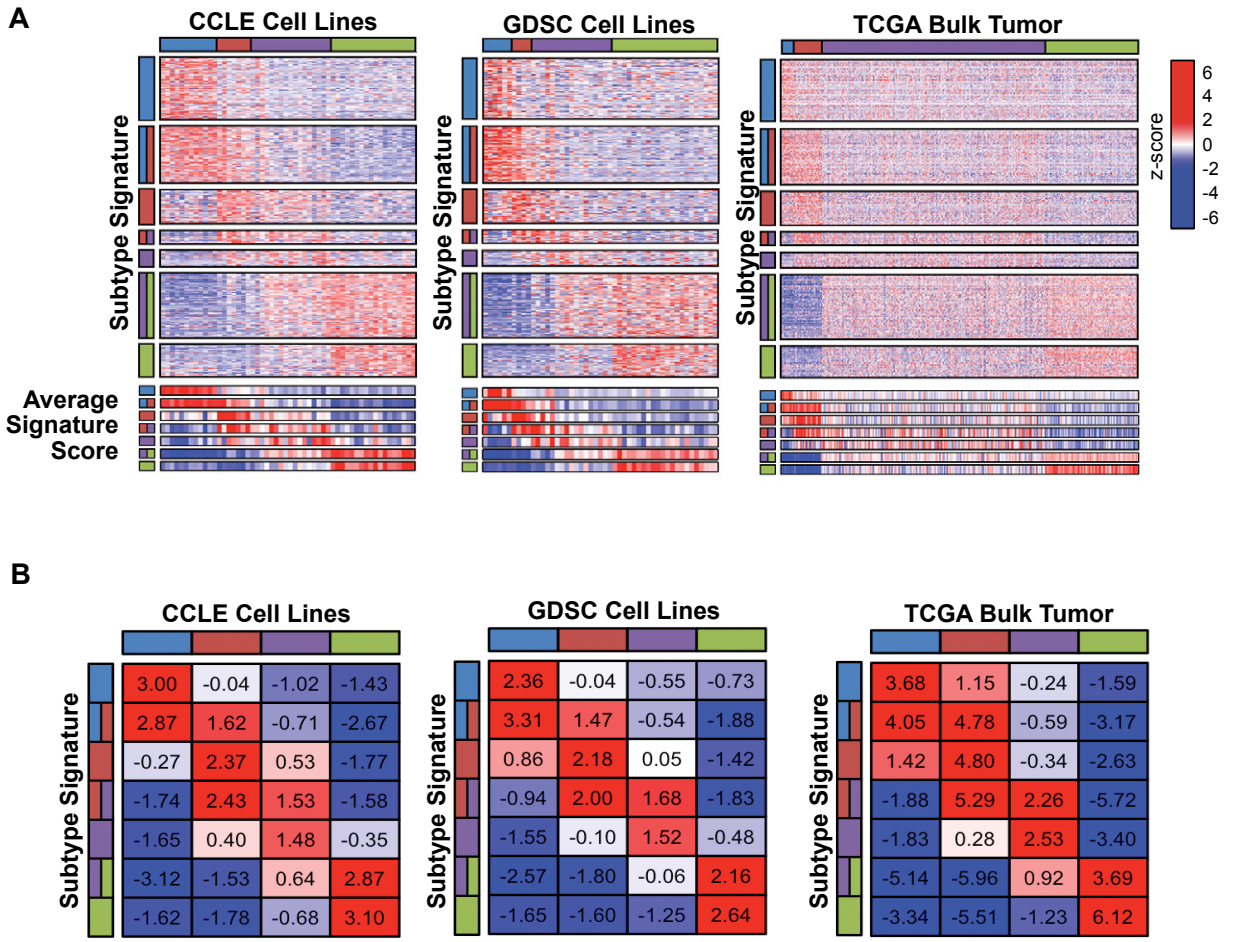

Figure 2-11. Validation of 4-stage differentiation signature genes in 3 independent datasets. (A) Heatmap of subtype signature genes (top) and average signature score (bottom) for each cell line or patient tumor samples in 3 independent datasets. (B) Heatmap of corresponding total averaged subtype scores across subtypes. To calculate the strength of each subtype signature, we calculated a score by averaging the subtype signature gene expression and then averaging all samples within a subtype set, where the average is weighted by the square root of number of samples to stabilize the variance of the mean.

Epigenetic changes in DNA methylation mirror the transcriptional programs of differentiation.

Through building a prediction model to classify melanoma subtypes in other data sets, we could harness additional paired resources to further characterize these melanoma subtypes. Since both the TCGA tumor and GDSC cell line profiles have matching methylation data, we looked to see to what extent global expression differences between differentiation stages could be regulated at the promoter methylation level. Evidence for the importance of epigenetic regulation in differentiation has been observed in genome-wide methylation analysis of melanoma that had showed hyper-methylation in regulating MITF gene expression (Lauss et al., 2015).

Similar to the gene expression data, PCA of the methylation beta values of the GDSC cell lines separates the subtypes into distinct groups following an arc-like trajectory (Figure 2-12A). Across the aforementioned transcription factors, we observed subtype-specific differences in their promoter methylation beta values that are inversely correlated with expression in both GDSC cell lines (Figure 2-12B) and TCGA tumors (Figure 2-12C). Specific examples include, lower beta values of MITF and CTNNB1 corresponding to higher expression in the transitory and melanocytic subtypes; lower beta values for SMAD3 corresponding to higher SMAD3 expression in the undifferentiated and neural crest like subtypes; and substantially higher beta values of SOX10 in the undifferentiated subtype, showing that the low expression of SOX10 could be due to promoter hyper-methylation. In addition to transcription factors, the AXL kinase appears to be regulated at the methylation level with higher beta values in the transitory and melanocytic subtypes corresponding to decreased expression in these subtypes.

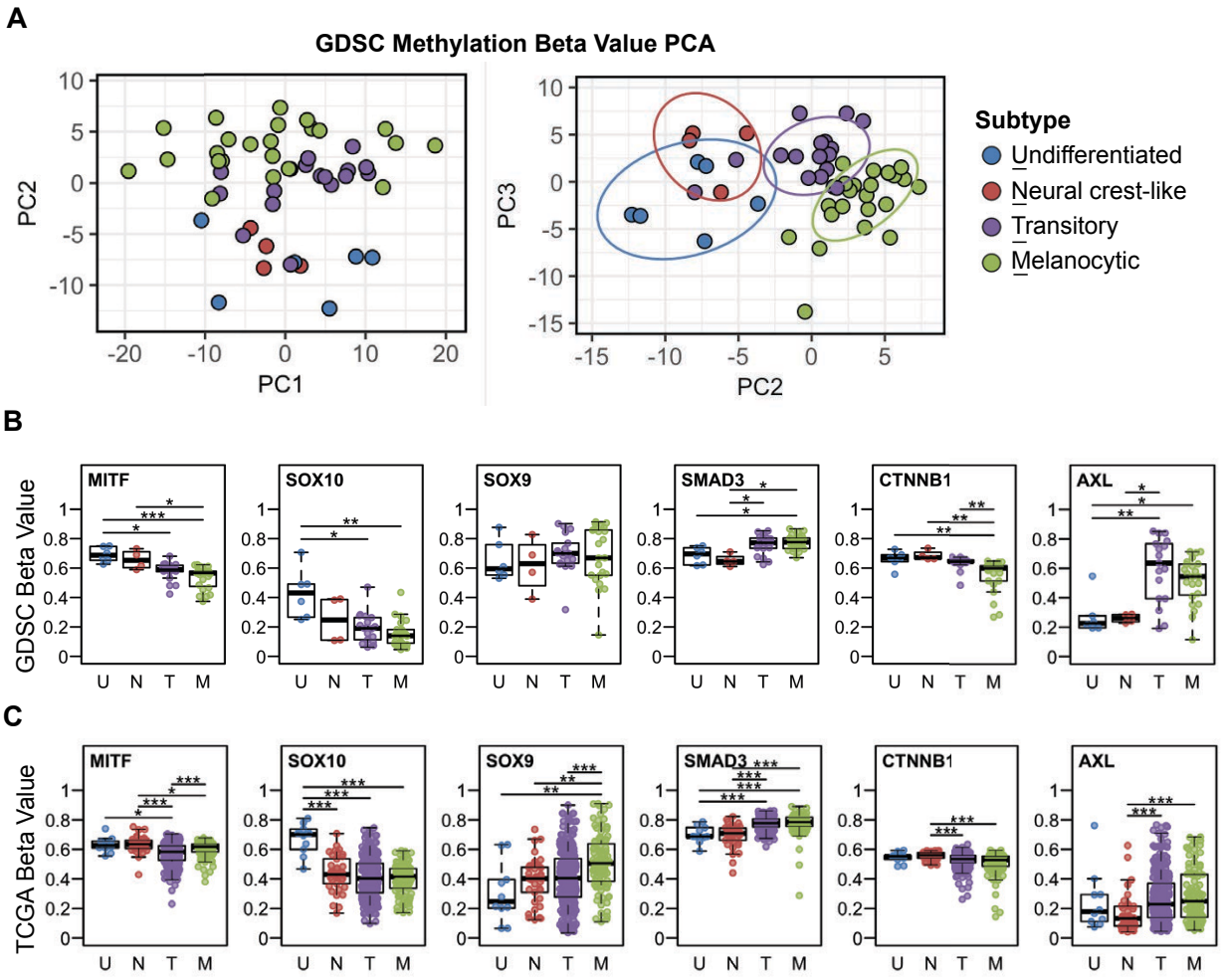

Figure 2-12. Epigenetic changes in DNA methylation mirror the transcriptional programs of differentiation. (A) PCA based on methylation beta values from the GDSC cell line dataset and annotated by predicted subtype. Plot of PC2 vs. PC3 shows subtype patterns similar to the arc-like differentiation trajectory observed with the gene expression PCA. Ellipses mark 80% confidence interval based on multivariate t-distribution. PC1 reflects other methylation signal not explained by the subtypes. (B-C) Beta values of select genes from the GDSC cell lines (A) or TCGA bulk tumors (B) grouped by predicted subtype. (U: Undifferentiated, N: Neural crest-like, T: Transitory, M: Melanocytic; number in each group, GDSC: U=6, N=4, T=17, M=23; TCGA: U=6, N=4, T=17, M=23; Kruskal-Wallis ANOVA and Dunn's post hoc test p-values: * ≤ 0.05, ** ≤ 0.01, *** ≤ 0.001).

DISCUSSION

Previously, we had identified four differentiation-related melanoma subtypes within our panel of cell lines. To evaluate these subtypes in the context of other datasets, we constructed an independently trained classifier that successfully predicted our subtypes across multiple datasets. PCA of each dataset when annotated by their predicted subtype consistently demonstrated inter-subtype relationships that follow our proposed differentiation progression. These findings illustrate that across melanoma datasets, the major melanoma-specific variances are related by differentiation state and can be summarized by two major components. The PC1 x-axis represents the previously appreciated linear melanocytic differentiation trend (Hoek et al., 2006). The PC2 y-axis represents acquisition of and then reversal from neural crest-related intermediate states, an on-off pattern that is reminiscent of the transient nature of neural crest cells and the transient nature of other developmental transcription programs (Spitz and Furlong, 2012; Telley et al., 2016).

Molecular classification strategies typically involve a variability measurement filter and variance arising from non-melanoma cells in the tumor microenvironment or adjacent normal tissue may overshadow true melanoma cell variance and therefore mask underlying melanoma cell autonomous biology. Problematic samples could be excluded based on purity estimates (Carter et al., 2012; Yoshihara et al., 2013), but this has the disadvantages of requiring a threshold, not benefiting from the full dataset, and not fully obtaining useful characterization of the less pure samples. Our analysis demonstrates how cell line-guided approaches can remove influences from non-melanoma cell contaminants to illuminate underlying cancer cell-autonomous biology trends. By training our classifier using cell line expression profiles, we were able to identify melanoma-specific subtypes within bulk tumors by features shared with cell lines, which increases the confidence of tumor specificity. Supporting this approach is the high concordance in gene expression observed between melanoma cell lines and tumors, and similar patterns observed when we systematically removed confounding signatures from the

bulk tumor expression profiles.

The universal nature of these subtypes and the ability to classify them across datasets enabled us to integrate our expression-based subtypes to additional matched datasets. Both GDSC and TCGA have paired methylation profiles, which enabled identification of subtype methylation differences congruent with gene expression, and consistent between cell lines and tumors. These results match the generally expected trend for methylated promoters to inhibit transcription and are supportive of epigenetic regulation of differentiation as previously appreciated (Cheng et al., 2015; Lauss et al., 2015; Shaffer et al., 2017).

In sum, our classification model identifies consistent differentiation-related subtypes in independent cell line and tumor datasets. Integration of the melanoma subtypes in areas that may have been previously unexplored in a differentiation context can guide future studies to discover novel relationships between melanoma differentiation state, cellular phenotypes, and therapy response.

CHAPTER 3:

Melanoma dedifferentiation status is a predictive marker of sensitivity to ferroptosis inducing drugs

INTRODUCTION

The dedifferentiation response to MAPK pathway inhibition and to pro-inflammatory signaling suggests that targeting the differentiation state could be a viable approach to overcome therapy resistance. Cell line pharmacogenomics databases combining genomic information with pharmacological response profiles have helped uncover associations between drug mechanisms of action and molecular subtypes (Barretina et al., 2012; Iorio et al., 2016; Seashore-Ludlow et al., 2015). Dedifferentiated melanomas are fundamentally different cells with divergent transcriptional profiles and phenotype (Hoek et al., 2006). Thus, these differences from its more differentiated counterparts could render cells more sensitive to new actionable pharmacological targets.

In this study, we integrated the predicted subtypes from our melanoma differentiation subtype classifier on a large panel of melanoma cell lines with the small molecule drug sensitivity profiled by the Cancer Therapeutics Response Portal (CTRP) (Seashore-Ludlow et al., 2015). Integration of our melanoma differentiation model with CTRP pharmacogenomic databases revealed a strong correlation between the degree of dedifferentiation and sensitivity to a type of cell death known as ferroptosis. Ferroptosis occurs through an iron-dependent accumulation of lethal lipid reactive oxygen species (ROS) and is regulated by GPX4, a glutathione-dependent enzyme that catalyzes the reduction of lipid ROS to lipid alcohols (Dixon et al., 2012; Yang et al., 2014). Ferroptosis is a relatively recent discovery of programmed cell death distinct from apoptosis and our findings provide a differentiated-guided approach in which it can be harnessed to counter a melanoma therapy escape route.

RESULTS

Sensitivity to ferroptosis inducing drugs is inversely correlated with differentiation status

Using our subtype classifier and refined framework of melanoma differentiation, we predicted differentiation-related subtypes from gene expression profiles of melanoma cell lines from the Cancer Cell Line Encyclopedia (CCLE) and Genomics of Drug Sensitivity in Cancer (GDSC) databases. Together, the predicted differentiation subtype and drug sensitivities of these cell lines previously characterized in the Cancer Therapeutics Response Portal (CTRP) enabled identification of new dedifferentiation-associated vulnerabilities (Seashore-Ludlow et al., 2015). To filter through the large number of small molecules characterized, we applied an ANOVA filter ($P<0.01$) to identify drugs that exhibited subtype-specific sensitivity. To increase the confidence of target specificity, we performed hierarchical clustering to identify drug clusters with a similar mechanism of action. An interrogation of the screened compounds revealed that with increased dedifferentiation status there was an increased sensitivity to all ferroptosis inducing drugs (n=4/4) irrespective of mutation status (Figure 3-1A-B). We applied our previously defined differentiation trajectory position scoring system to quantify the relative differentiation between samples and found the relationship between dedifferentiation and sensitivity was significantly correlated for all compounds (Figure 3-1C). The ferroptosis inducing compounds include erastin, (1*S*, 3*R*)-RSL3, ML162, and ML210. Small molecule compounds (1*S*, 3*R*)-RSL3 (hereafter referred to as RSL3), ML162, ML210 induce ferroptosis by direct inhibition of GPX4, while erastin indirectly inhibits GPX4 through depletion of glutathione by targeting the System Xc^- transporter (Dixon et al., 2012; Yang et al., 2014).

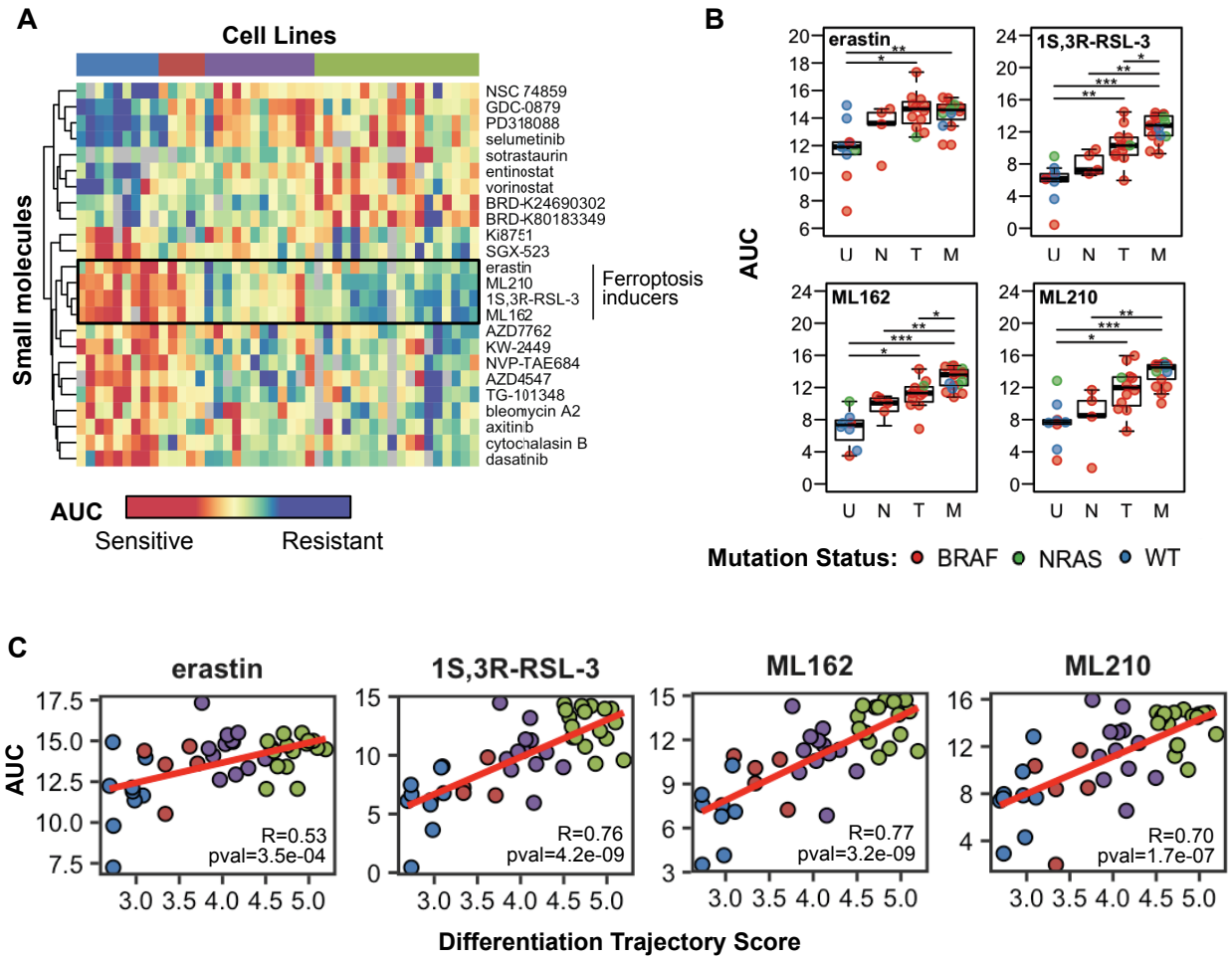

Figure 3-1. Integration of pharmacogenomics drug sensitivity profiles reveals dedifferentiation-related subtype-specific sensitivity to ferroptosis inducing drugs. (A) Hierarchical clustering of the CTRP pharmacogenomics database AUC values for small molecules pre-filtered for ANOVA P<0.01 across melanoma cell lines grouped by predicted subtype (B) Area under the curve (AUC) sensitivity values for the indicated ferroptosis inducing drugs grouped by predicted melanoma differentiation subtype. (U: Undifferentiated, N: Neural crest-like, T: Transitory, M: Melanocytic; Kruskal-Wallis ANOVA and Dunn's post hoc test p-values: * ≤ 0.05, ** ≤ 0.01, *** ≤ 0.001, lower AUC values indicate increased sensitivity) C) Plot of AUC values vs. the differentiation trajectory score for all ferroptosis inducing drugs from the CTRP show highly correlative relationship between sensitivity and dedifferentiation. Low AUC values indicate increased sensitivity.

Pharmacogenomics prediction of differentiation state sensitivity is reproducible in independent melanoma cell lines

To validate the association between dedifferentiation and ferroptosis sensitivity observed from the CTRP, we experimentally tested the sensitivity of ferroptosis inducing drugs in the original set of cell lines used in our classification analysis (Figure 3-2A, Figure 3-3A). As predicted by the CTRP results, sensitivity to the ferroptosis inducing drugs erastin and RSL3 was highly correlated to dedifferentiation score (Figure 3-2B, Figure 3-3B). In order of progressive dedifferentiation, the melanocytic subtype cell lines were more resistant to both drugs, the transitory and neural crest-like subtype lines were moderately sensitive, and the undifferentiated subtype cell lines were highly sensitive. Vemurafenib-induced dedifferentiation from the parental cell line with adaptive resistance or acquired resistance also resulted in an increase in ferroptosis sensitivity (Figure 3-2C, Figure 3-3C). As a negative control, M249R, which achieves resistance through acquisition of an *NRAS* mutation with no change in differentiation status, was equally insensitive to ferroptosis induction as the parental line. However, we acknowledge there may be other factors that affect sensitivity since there are some exceptions to undifferentiated subtype where some cell lines are only moderately sensitive to erastin or RSL3.

Furthermore, the dedifferentiation-associated patterns of sensitivity to ROS inducing drugs are specific to those that promote ferroptosis. Other subclasses of drugs in the CTRP that modulate oxidative stress but do not induce ferroptosis do not show these patterns (Figure 3-4A). Additionally, treatment with piperlongumine, a ROS inducing drug that triggers apoptosis (Raj et al., 2011), did not display any differentiation-associated trend in sensitivity in the subset of our evaluated cell lines (Figure 3-4B).

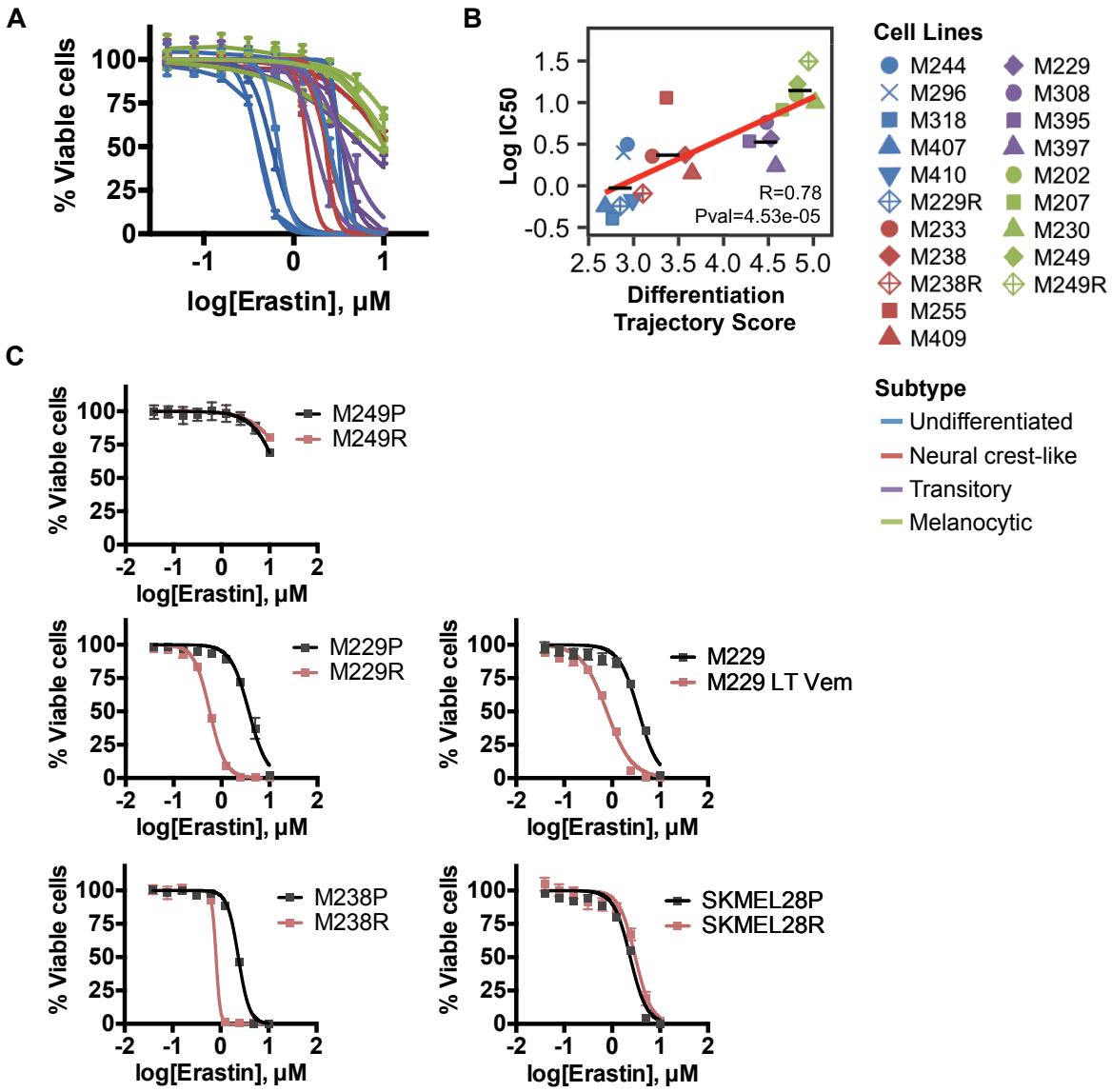

Figure 3-2. Experimental validation in independent cell lines demonstrates the reproducibility of dedifferentiation-related sensitivity to erastin. (A) Validation of erastin sensitivity patterns across indicated M series melanoma cell lines. Resistant variant curves are denoted by diamond shape with dashed lines. (B) Plot of log IC50 concentration values from dose-response curves of erastin treatment against the differentiation trajectory score showing strongly correlative relationship between dedifferentiation and sensitivity. (C) Increase in sensitivity to erastin with dedifferentiation from acquired or adaptive vemurafenib resistance (LT Vem = 44 days).

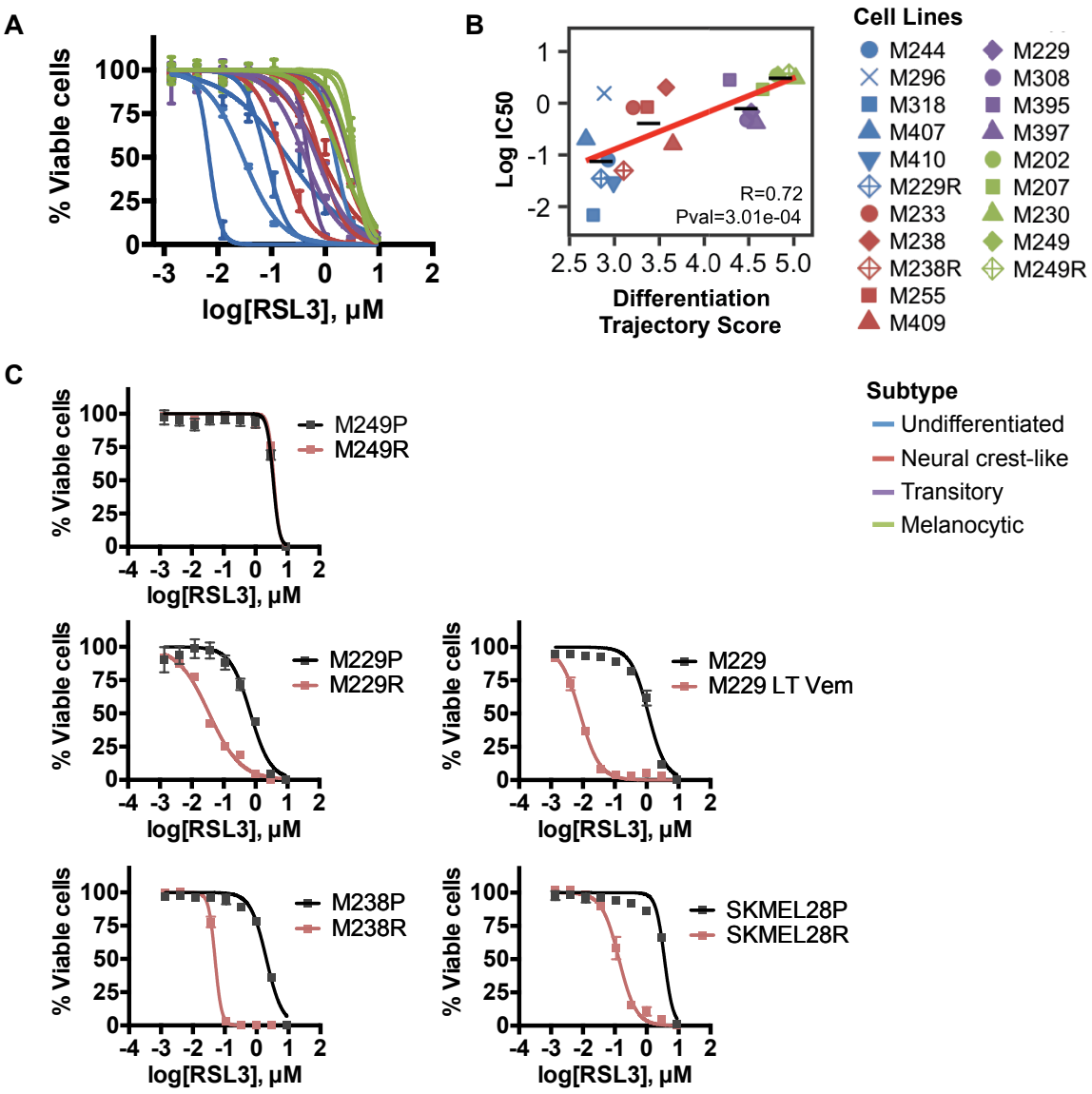

Figure 3-3. Experimental validation in independent cell lines demonstrates the reproducibility of dedifferentiation-related sensitivity to RSL3. (A) Validation of RSL3 sensitivity patterns across indicated M series melanoma cell lines. Resistant variant curves are denoted by diamond shape with dashed lines. (B) Plot of log IC50 concentration values from dose-response curves of RSL3 treatment against the differentiation trajectory score showing strongly correlative relationship between dedifferentiation and sensitivity. (C) Increase in sensitivity to RSL3 with dedifferentiation from acquired or adaptive vemurafenib resistance (LT Vem = 44 days).

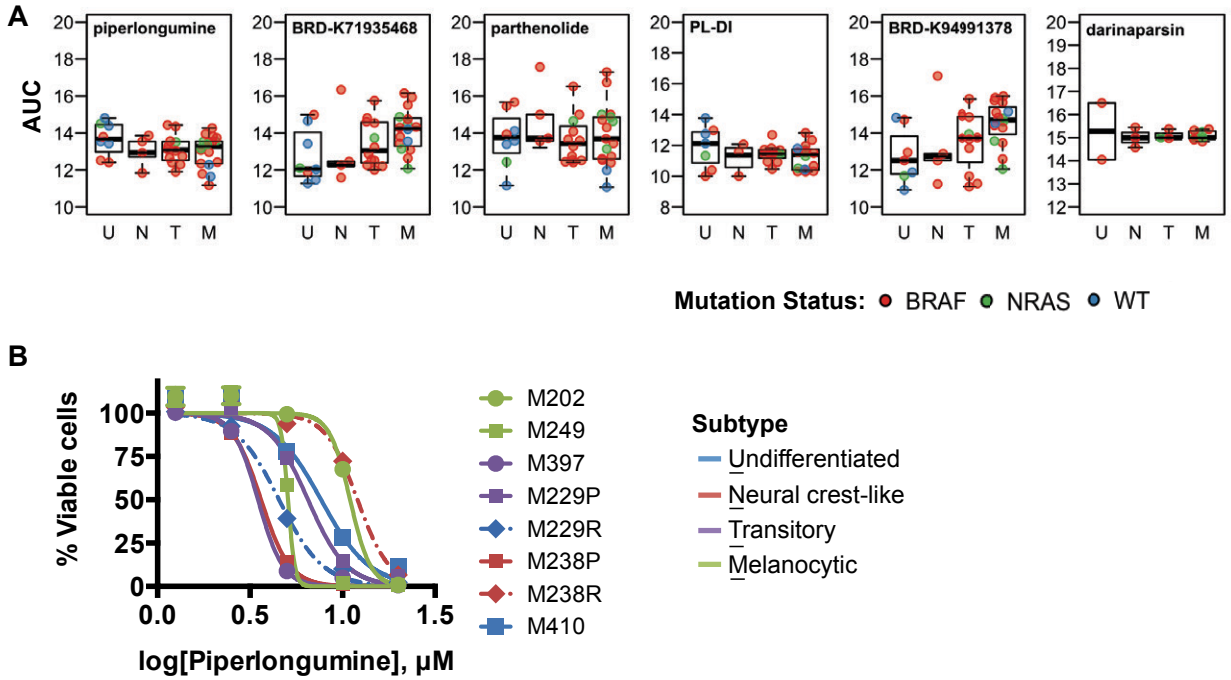

Figure 3-4. Dedifferentiation associated sensitivity to oxidative stress is limited to ferroptosis inducing drugs. (A) Boxplot of AUC values from the CTRP for other ROS generating drugs that do not induce ferroptosis do not show any distinguishable subtype trends. (U: Undifferentiated, N: Neural crest-like, T: Transitory, M: Melanocytic; Kruskal-Wallis ANOVA and Dunn's post hoc test p-values: * ≤ 0.05, ** ≤ 0.01, *** ≤ 0.001) (B) Validation of no difference in sensitivity among subtypes and vemurafenib resistant lines when treated with the ROS-inducing, but not ferroptosis-inducing, drug piperlongumine.

Erastin-induced cell death occurs through the ferroptosis mechanism

Due to the increased levels of System Xc^- observed across various cancer types that highlght its potential as a therapeutic target (Doxsee et al., 2007; Guo et al., 2011; Lo et al., 2008; Timmerman et al., 2013), we focused on exploring the treatment of melanoma cells with erastin. While erastin was less well correlated than the other GPX4 inhibitors to differentiation in the CTRP pharmacogenomics dataset, the results were concordant within our own validation. This could likely be attributed to the different media and redox buffering components used in the cell lines from the CTRP, which can affect the inhibition of glutathione synthesis achieved by erastin.

We first sought to confirm if the mechanism of cell death by erastin treatment in the dedifferentiated melanoma cells occurs through ferroptosis. Treatment with erastin resulted in a dose-dependent decrease in percent viable cells in the undifferentiated signature cell lines cell lines M296, M410 M229R, and M238R that can be almost completely rescued either by iron chelation using deferoxamine (DFO) or by the lipophilic antioxidant Trolox (Figure 3-5A), demonstrating that cell death is both iron and ROS dependent respectively. Furthermore, cell death occurred rapidly within 12 hours and completely prevented by DFO or Trolox treatment (Figure 3-5B). The mechanism of cell death induced by erastin is distinct from apoptosis, as treatment with the pan-caspase inhibitor Z-VAD-FMK could not rescue death induced by erastin treatment, but could rescue apoptosis induced by staurosporine as a positive control (Figure 3-6). Furthermore, we observed a high induction of lipid ROS at a time preceding cell death (10 hr) in the erastin sensitive cell lines, which was not present in the other non-sensitive lines tested (Figure 3-7). This increase in lipid ROS could be rescued by DFO treatment, further indicating that cell death occurs through the iron dependent accumulation of lipid ROS, a key characteristic of ferroptosis. At the same time-point post-treatment, erastin treatment also induces elevated levels of cytosolic ROS but at substantially higher levels in the undifferentiated signature cell lines. This increase in cytosolic ROS was also iron-dependent and was reduced

by DFO treatment (Figure 3-8).

Differential sensitivity to ferroptosis is attributed to basal glutathione levels

To test if the differences in ROS levels in the less sensitive cells were due to the inability of erastin to deplete glutathione, we measured glutathione by mass spectrometry in isogenic sub-lines M229P and M229R, and M238P and M238R. Erastin treatment significantly depleted both reduced glutathione (GSH) and oxidized glutathione (GSSG) across all the cell lines (Figure 3-8A-B). However, M229R and M238R had lower basal levels and also exhibited a greater fold change decrease with treatment compared to their respective parental lines in both GSH and GSSG. We confirmed the basal levels of reduced glutathione in the vemurafenib-resistant cell lines were significantly lower than parental cell lines through quantification using Ellman's reagent (Figure 3-9C). Furthermore, levels of reduced glutathione were significantly correlated to the degree of dedifferentiation, providing a mechanistic link between sensitivity to ferroptosis inducing drugs and differentiation state (Figure 3-9C). The lower levels of reduced glutathione could account for the differences in ferroptosis sensitivity, as supplementation of the culture medium with GSH substantially rescued both erastin and RSL3 cell death (Figure 3-10).

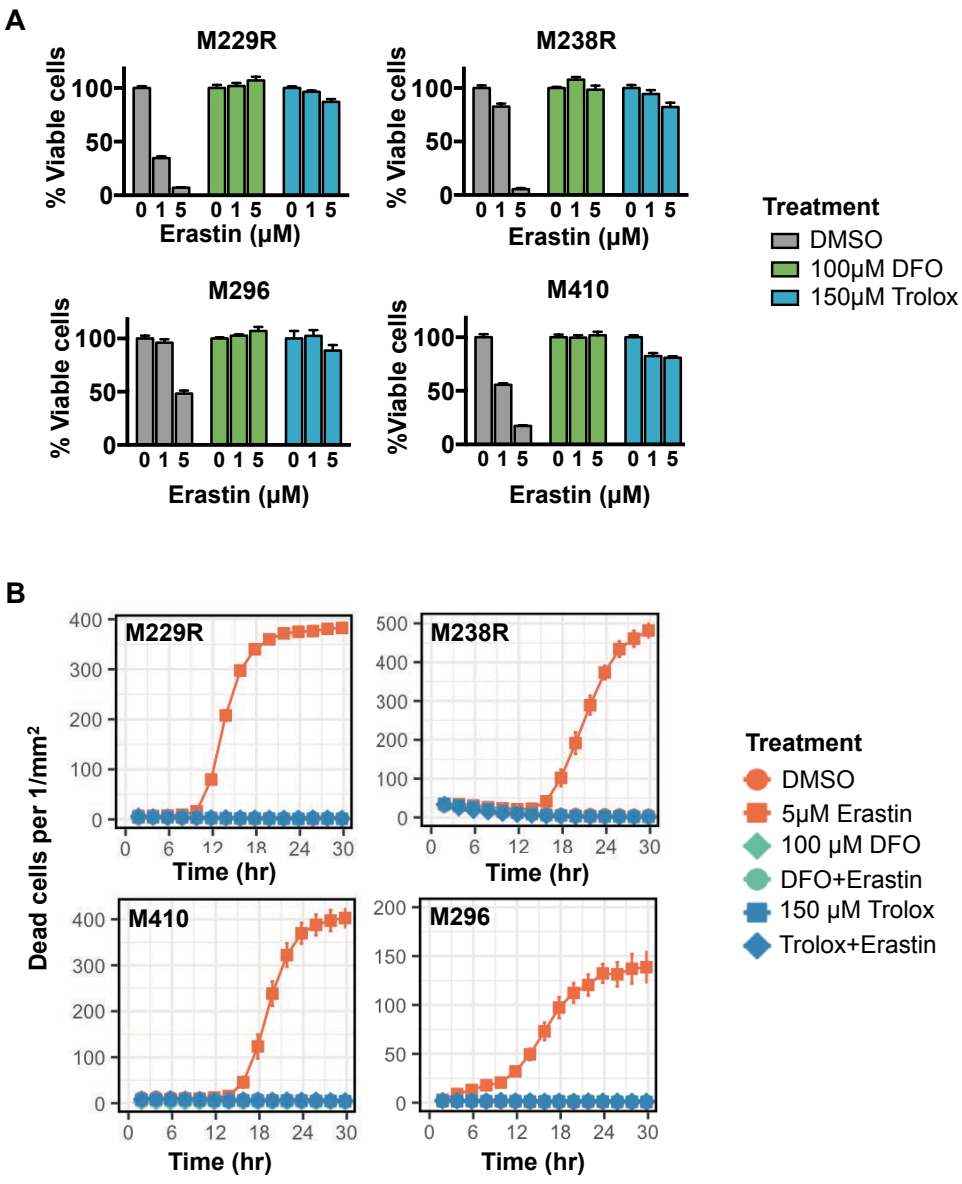

Figure 3-5. Erastin treatment induces canonical features of ferroptosis in dedifferentiated melanoma cells. (A) Measurement of percent viable cells compared to DMSO control with erastin treatment alone or in combination with DFO or Trolox. (B) Cytotoxicity assay using the Incucyte Cytotox Red reagent showing rapid cell death with erastin treatment that can be prevented with DFO or Trolox.

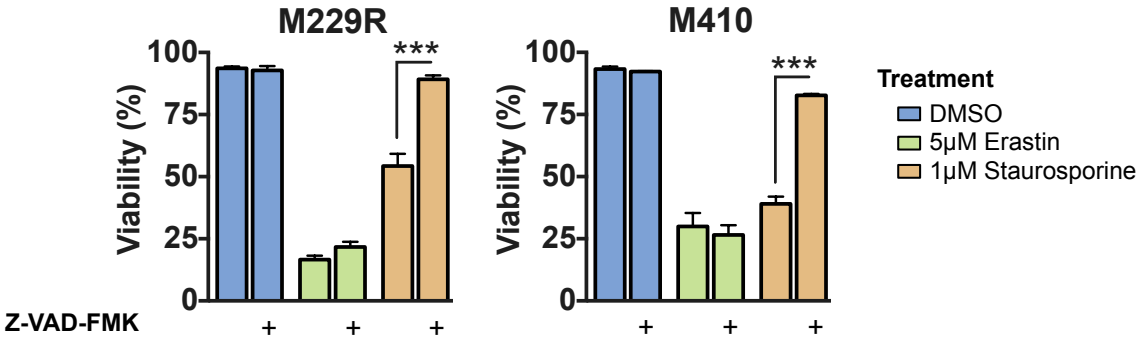

Figure 3-6. Erastin treatment induces non-apoptotic cell death in dedifferentiated melanoma cells. Trypan blue exclusion assay of 24 hr erastin or staurosporine treatment with or without caspase inhibitor Z-VAD-FMK pre-treatment for 1 hr.

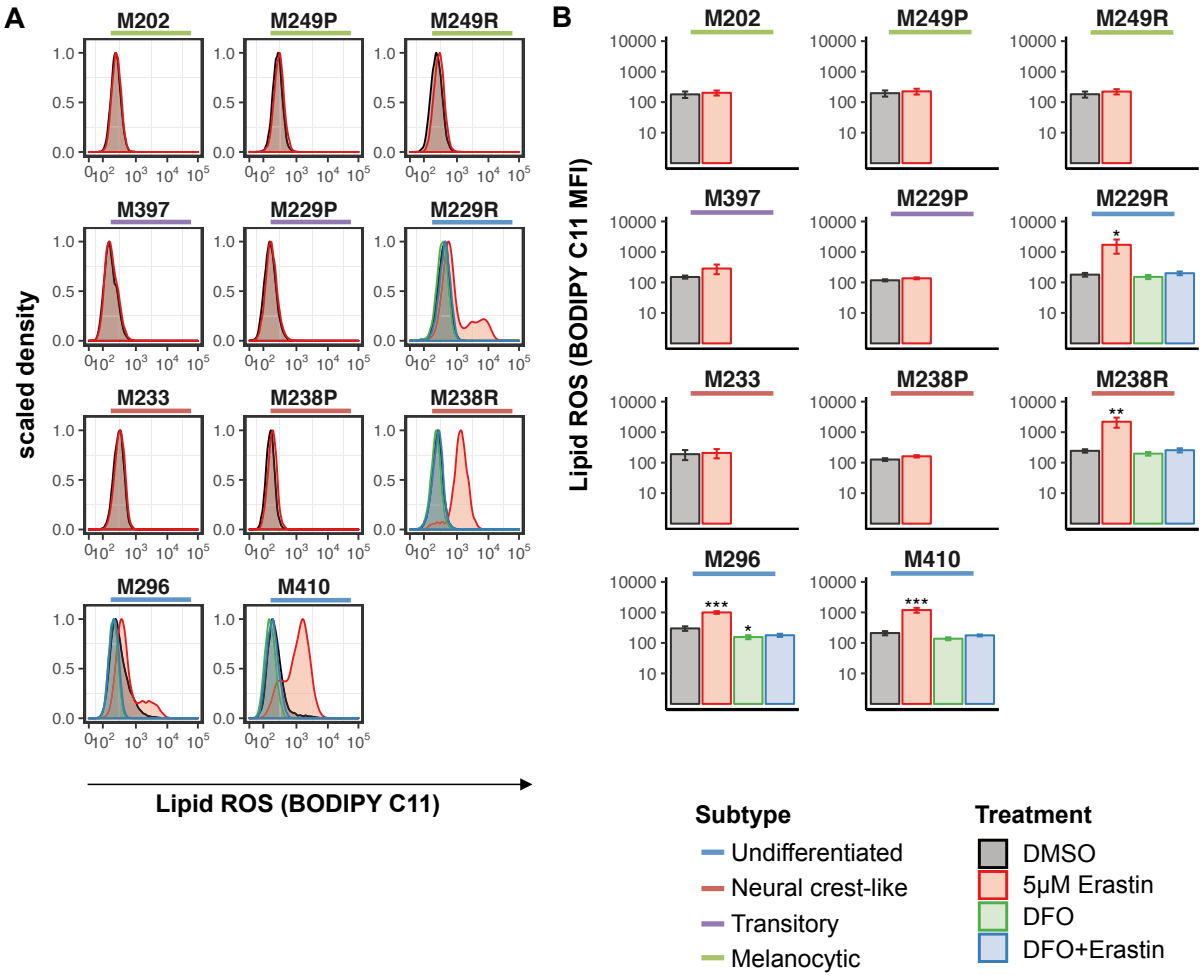

Figure 3-7. Erastin treatment induces lipid ROS in ferroptosis-sensitive cells. (A) ROS measurements after 10 hr erastin treatment across cell lines by flow cytometry using BODIPY-C11 probe to measure lipid ROS. (B) Barplot of mean fluorescence intensity of BODIPY-C11 after 10 hr erastin treatment across cell lines. Data represents mean ± sem of three independent experiments.

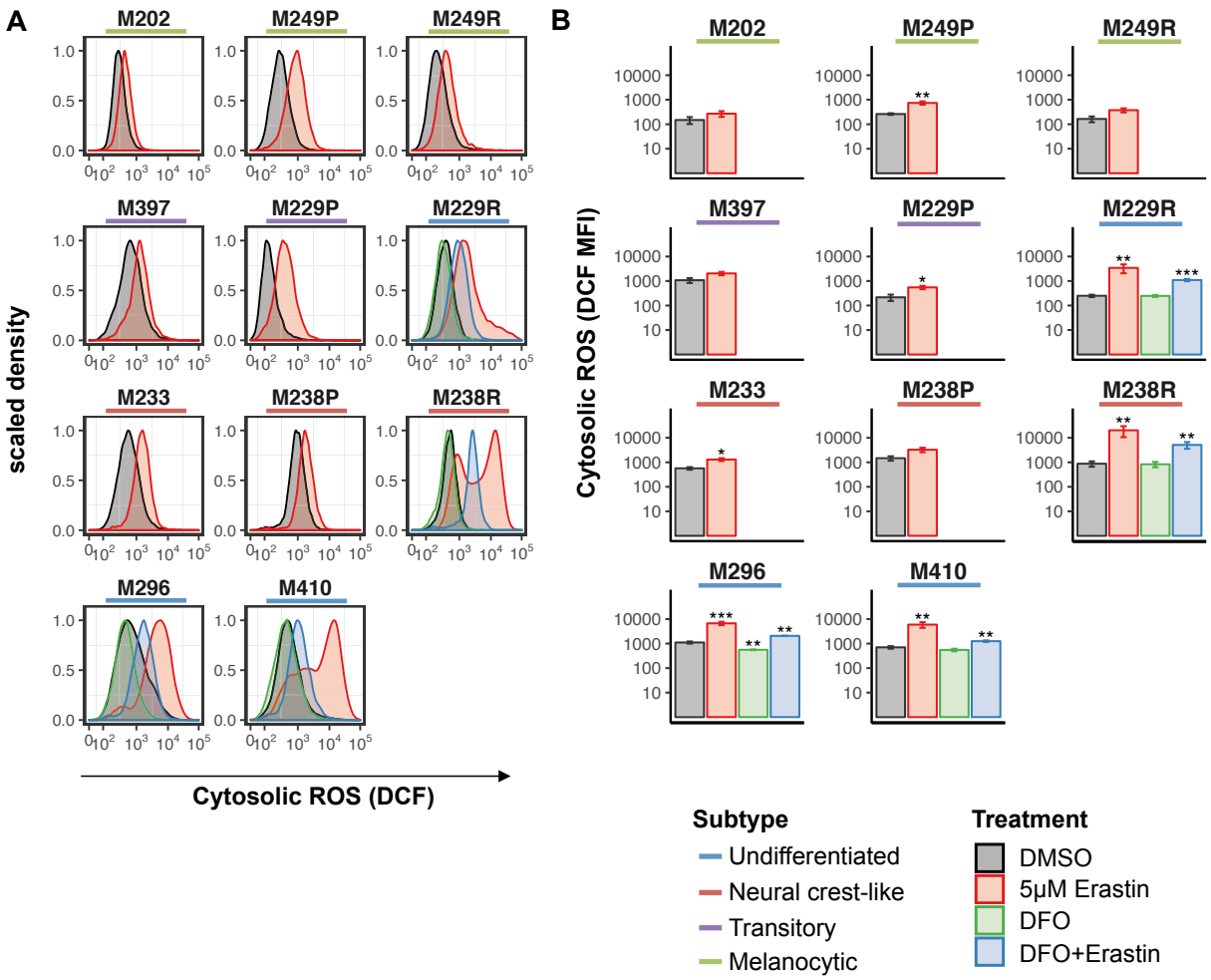

Figure 3-8. **Erastin treatment induces higher levels of cytosolic ROS in ferroptosis-sensitive cells**. (A) ROS measurements after 10 hr erastin treatment across cell lines by flow cytometry using CM-H2DCFDA probe to measure cytosolic ROS. (B) Barplot of mean fluorescence intensity of CM-H2DCFDA after 10 hr erastin treatment across cell lines. Data represents mean ± sem of three independent experiments.

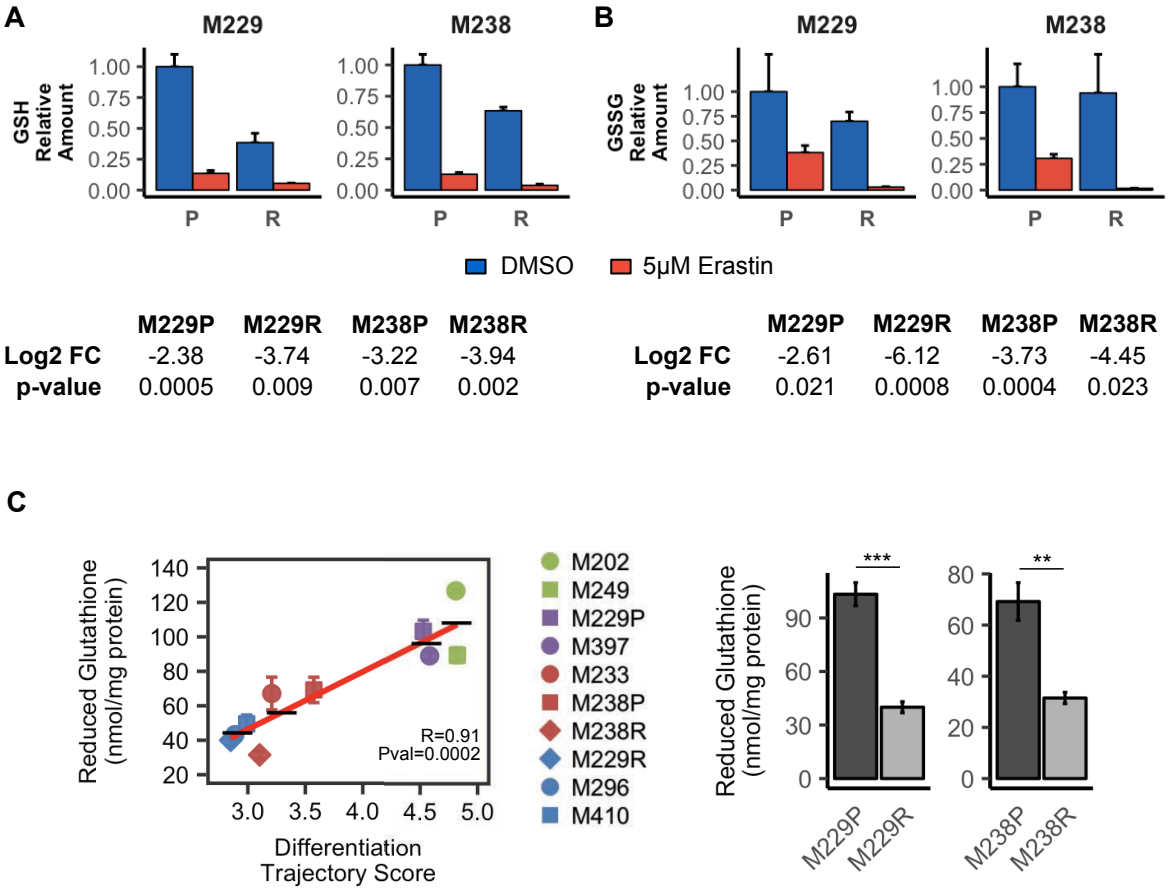

	M229P	M229R	M238P	M238R
Log2 FC	-2.38	-3.74	-3.22	-3.94
p-value	0.0005	0.009	0.007	0.002

	M229P	M229R	M238P	M238R
Log2 FC	-2.61	-6.12	-3.73	-4.45
p-value	0.021	0.0008	0.0004	0.023

Figure 3-9. Sensitivity to ferroptosis induction is associated with low basal levels of glutathione. (A-B) Relative amounts of reduced glutathione GSH (A) and oxidized GSSG (B) after 8 hr erastin treatment compared to untreated parental control for the indicated isogenic cell lines. (P: Erastin-insensitive parental cell lines; R: erastin-sensitive BRAFi-resistant cell lines.) Data shown in barplots represent mean ± sem of three replicates. (C) Plot of reduced glutathione (GSH) levels measured by Ellman's reagent vs. the differentiation trajectory score in melanoma cell lines, with means of each subtype group indicated by black dashes (left). Barplot of GSH levels of the isogenic cell line pairs (right).

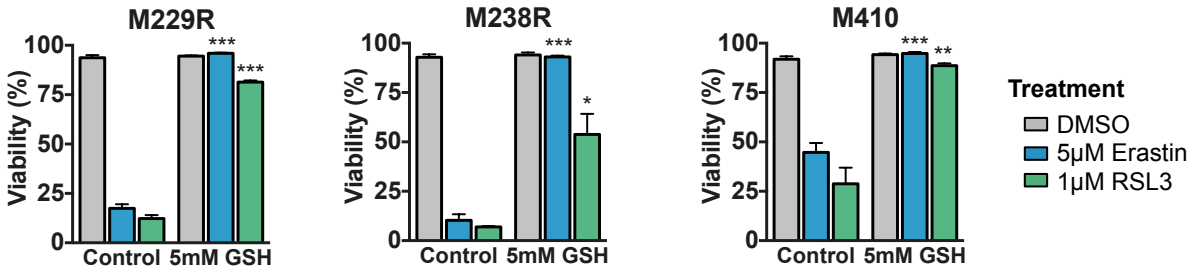

Figure 3-10. Ferroptotic cell death is rescued by addition of reduced glutathione. Trypan blue exclusion assay of 24 hr erastin or RSL3 treatment with or without supplementation of 5mM GSH in the culture medium. Data shown in barplots represent mean ± sem of three independent experiments; t-test p-values: * ≤ 0.05, ** ≤ 0.01, *** ≤ 0.001.

Combination treatment with ferroptosis inducing drugs is effective against BRAF inhibition-induced dedifferentiation and resistance

Erastin and other ferroptosis inducing drugs were initially discovered from a RAS synthetic lethal screen and studies have shown a dependence on MAPK signaling for ferroptosis in some contexts (Dolma et al., 2003; Yang and Stockwell, 2008; Yagoda et al., 2007). Therefore, to evaluate the feasibility of combination treatment to overcome BRAF inhibitor resistance, we first confirmed that the presence of vemurafenib does not reduce the high lethality observed with erastin treatment in dedifferentiated, vemurafenib-resistant cell lines. As expected, vemurafenib treatment alone was effective in reducing the viability of parental cell lines M229P and M238P, but had little effect on vemurafenib-resistant lines M229R and M238R. On the other hand, treatment with erastin in the dedifferentiated M229R and M238R lines resulted in a substantial loss of viable cells that was not attenuated even in the presence of high concentrations of vemurafenib (Figure 3-11A). Moreover, there was no consistent difference between ERK signaling levels between the isogenic cell line pairs or among the subtypes that associated with ferroptosis sensitivity (Figure 3-11B). Taken together, these results indicate MAPK-ERK signaling may not regulate ferroptosis in melanoma, and that there is no drug antagonism between BRAF inhibition and erastin in these dedifferentiated melanoma cells.

Erastin and BRAF inhibitors optimally target melanoma cells at distinct differentiation stages. Since dedifferentiation is an adaptive response to BRAFi, we sought to directly test the efficacy of combining erastin with BRAF inhibition against a cohort of BRAF mutant melanomas. We evaluated the effects of combination treatment on three melanoma cell lines that are initially BRAFi sensitive but eventually become resistant due to dedifferentiation. Biomarker evaluation of persisting cells after long-term vemurafenib treatment showed upregulation of AXL and NGFR, and downregulation of MITF or its target gene MART-1, confirming their inhibitor-induced dedifferentiation (Figure 3-12A). Of note, at this prolonged treatment time-point, pERK

levels have rebounded likely due to signaling feedback mechanisms as previously observed to begin within a few days of MAPK inhibition (Figure 3-12B) (Lito et al., 2012; Paraiso et al., 2010). Inclusion of erastin with vemurafenib in the treatment protocol resulted in a substantial decrease in long-term persisting cells (16-24 days), supporting this dual targeting therapeutic approach (Figure 3-13A). Similar results were also observed with RSL3 treatment, supporting the dual targeting therapeutic approach with ferroptosis inducing drugs (Figure 3-13B).

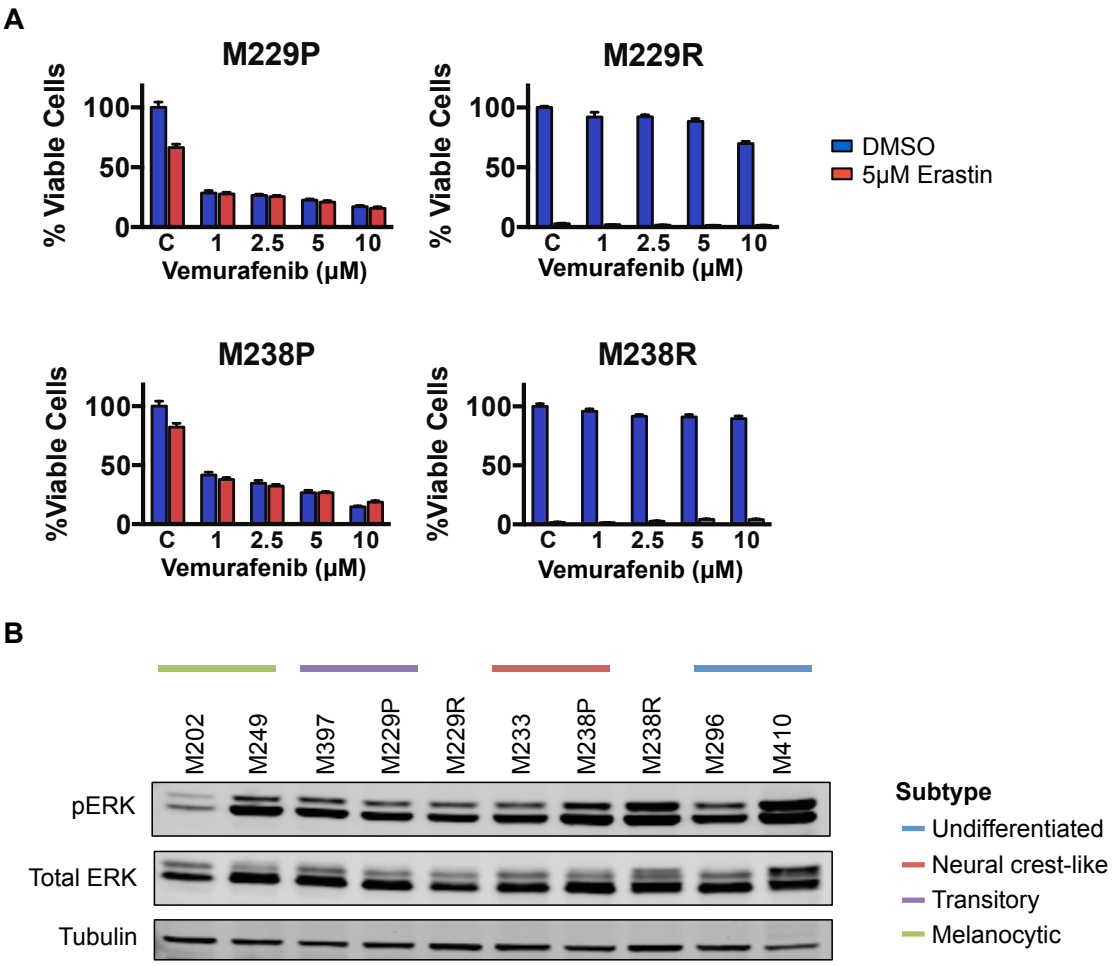

Figure 3-11. MAPK pathway inhibitors do not antagonize erastin-induced loss of viability. (A) Measurement of percent viable cells compared to vehicle control (DMSO) of erastin treatment combined with increasing concentration of BRAFi vemurafenib for 72 hours. Data shown in barplots represent mean ± sem of three replicates. (B) Immunoblot of phospho-ERK (T202/Y204) levels across melanoma grouped cell lines by subtype.

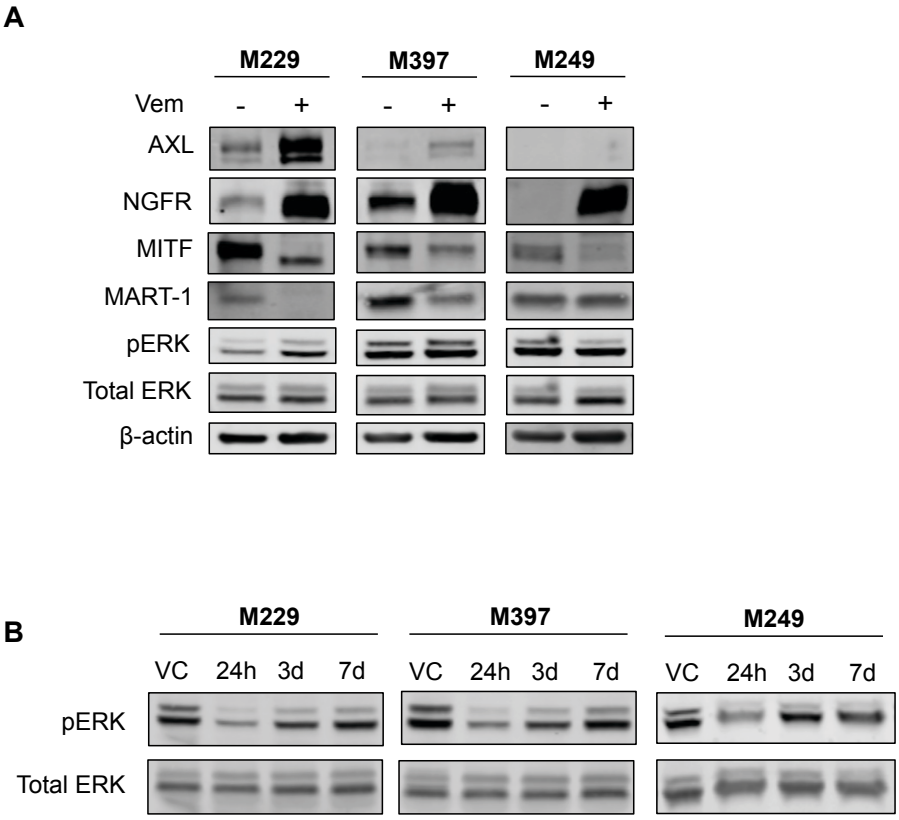

Figure 3-12. Long-term vemurafenib treatment induces dedifferentiation in melanoma. (A) Increases in the AXL and NGFR biomarkers, and decreases in the MITF and MART-1 biomarkers (immunoblot) confirming dedifferentiation of cell lines treated with long-term (21 days) vemurafenib treatment. (B) Immunoblot of phospho-ERK (T202/Y204) at vemurafenib treatment (1 μM) for the indicated time-points.

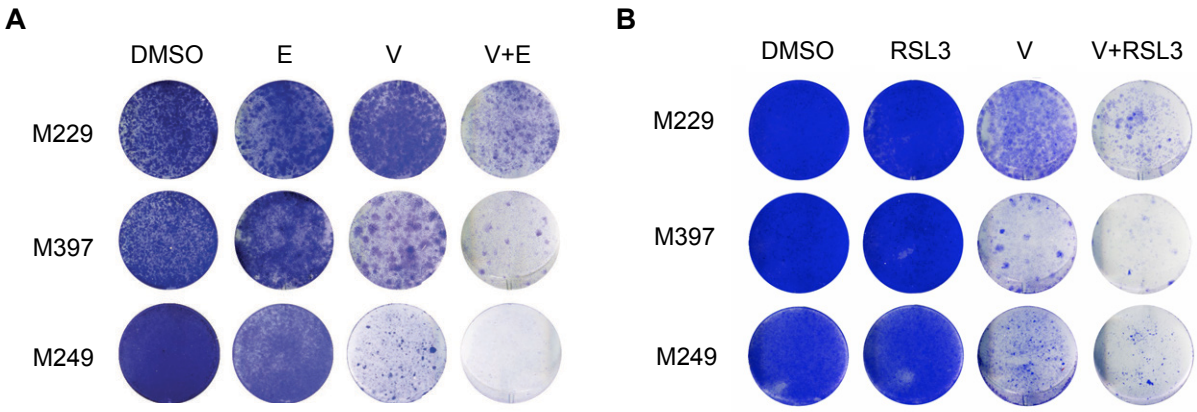

Figure 3-13. Reduction in persistent vemurafenib-induced dedifferentiated melanoma cells upon combination treatment with erastin or RSL3. (A-B) Crystal violet staining assays of long-term combination treatment of erastin (A) or RSL3 (B). For erastin: cells were treated with erastin (E= 2 μM for M229/M397, 5 μM for M249) and/or vemurafenib (V= 1 μM) for 16 days (M229), 24 days (M397), or 21 days (M249). For RSL3: cells were treated with RSL3 (R= 150 nM for M229, 40nM for M397, and 500 nM for M249) and/or vemurafenib (V= 1 μM) for 21 days. DMSO treated cells were stained when confluent at 7 days.

Inflammation-induced dedifferentiation increases sensitivity of melanoma cells to ferroptosis inducing drugs

An inflammatory microenvironment from elevated immune activity can also promote dedifferentiation of melanoma cells. Therefore, we next sought to test if immunotherapy-associated, cytokine-induced dedifferentiation would cause melanoma cells to become more sensitive to erastin treatment. The dedifferentiation response of melanoma cells to pro-inflammatory signaling can be replicated *in vitro* by treating cell lines with T cell secreted cytokines such as TNFα and IFNγ. We confirmed that TNFα and IFNγ stimulation resulted in activation of the NFKB or STAT1 signaling pathways (Figure 3-14A) and induced dedifferentiation, as determined by up-regulation of AXL and decreased levels of MITF or its target gene MART-1 (Figure 3-14B). The degree of dedifferentiation was cell specific and more prominent in cell lines M229 and M397. Consistent with the dedifferentiation response, treatment with erastin under cytokine stimulation resulted in increased cell death compared to cytokine-only or untreated cells (Figure 3-15A). In a cell line with only modest biomarker-based dedifferentiation upon IFNγ cytokine treatment (M249), we still observed increased sensitivity under higher doses of erastin (5 μM). In these experiments, the combined treatment contributed substantially and in some cases in a synthetic lethal fashion to reducing any persisting population. As with the vemurafenib co-treatment case, similar results were also observed with RSL3 treatment, supporting the dual targeting therapeutic approach with ferroptosis inducing drugs under inflammatory cytokine stimulation (Figure 3-15B).

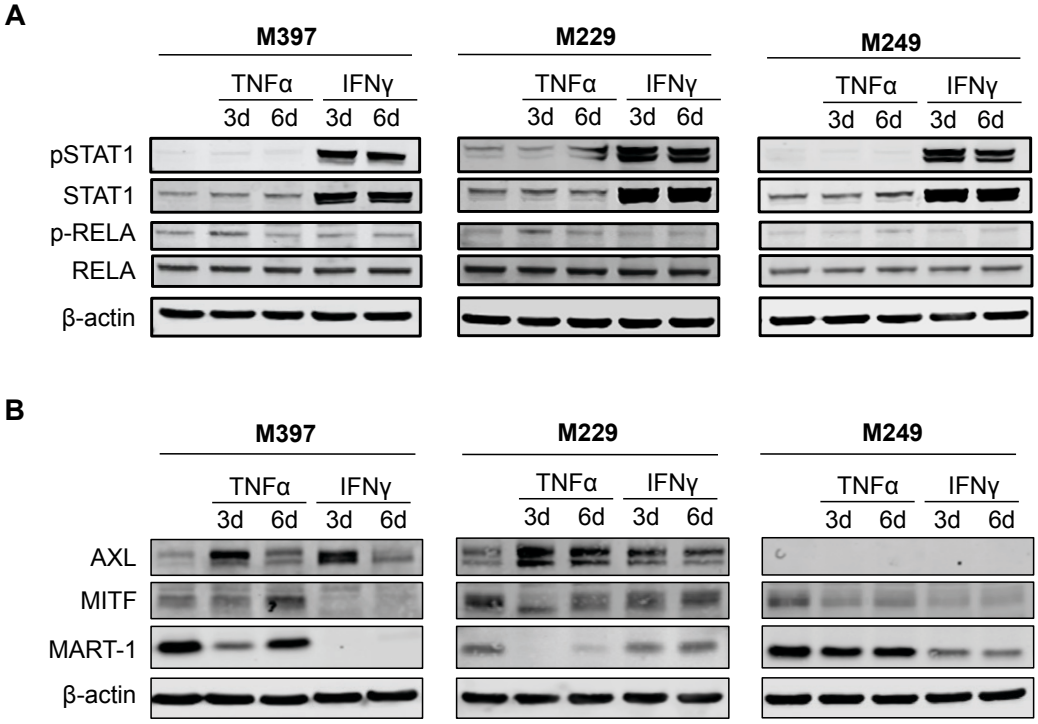

Figure 3-14. Inflammatory cytokine stimulation induces dedifferentiation in melanoma. (A) Immunoblot showing activation of NFkB p65 (RELA) by phosphorylation of S536 by TNFα treatment, and activation of STAT1 by phosphorylation of Y701 by IFNγ treatment. (B) Immunoblot showing increases in the AXL biomarker, and decreases in the MITF and MART-1 biomarkers confirming dedifferentiation of cell lines treated with the indicated cytokines.

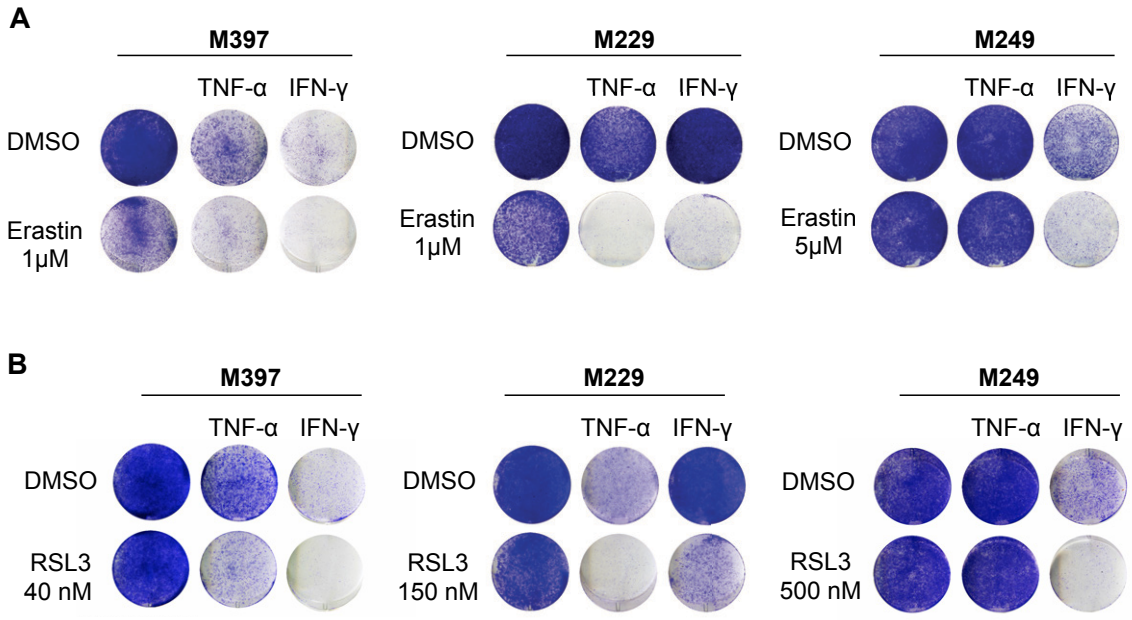

Figure 3-14. Reduction in persistent cytokine-induced dedifferentiated melanoma cells upon combination treatment with erastin or RSL3. (A-B) Crystal violet staining assays of erastin (A) or RSL3 (B) treatment at the indicated dose for 7 days with cytokine exposure for the initial 3 days (M229 and M249) or 7 days (M397). IFNγ=100 U/mL, TNFα=1000 U/mL. Data shown is representative of three independent experiments.

DISCUSSION

The mechanism of ferroptosis is a relatively recent discovery, and our study further advances the field by bringing it into the context of melanoma where it has not been extensively explored. We identified a previously unreported association of sensitivity to ferroptosis induction with the degree of dedifferentiation, where the undifferentiated subtype was the most sensitive and the melanocytic subtype was the most resistant. This sensitivity to ferroptosis complements existing therapies that preferentially target differentiated melanomas, but problematically induce dedifferentiation in therapy resistance. Our experiments support the efficacy of ferroptosis inducing drugs in targeting both innate resistance, and acquired dedifferentiation-associated resistance induced by kinase therapies and by immunotherapy-associated cytokines. Thus, combination therapies that include ferroptosis inducing drugs have the potential to enhance current treatment options for melanoma patients by providing a synthetic lethal approach to kill the persistent melanoma cell populations.

With targeted therapies, dedifferentiation-based adaptation can be seen in patient biopsies in as little as 1 to 3 weeks (Kwong et al., 2015). This early adaptation timeframe argues for upfront co-treatment, which has generally been found to be more efficient than sequential therapy (Eroglu and Ribas, 2016). Upfront co-targeting would furthermore prevent persisting melanoma cells from accumulating additional genomic alterations such as *NRAS* mutations or *BRAF* amplifications that would make treatment more difficult. In the context of immunotherapy, further relevance for a dual-targeting approach comes from the observation that melanoma cells can up-regulate surface expression of the PD-L1 ligand in response to inflammatory IFNγ signaling. Surface tumor PD-L1 can suppress T cell function through engagement of inhibitory PD1 receptor signaling (Iwai et al., 2002; Taube et al., 2012). Therefore, reducing this dedifferentiated persisting population of cells via their sensitivity to ferroptosis induction can potentially boost overall anti-tumor immunity by preventing an accumulation of melanoma cells

with immunosuppressive capabilities.

In summary, our refined framework of multi-stage melanoma differentiation subtypes guided the discovery of a rational therapeutic strategy to target the plasticity of melanoma cells associated with resistance. Dedifferentiation is a recurrent innate and acquired resistance mechanism to modern kinase targeted therapies and immunotherapies in the clinic. Our results propose and support a new co-treatment approach to effectively target the dedifferentiation-associated resistance escape route that limits the efficacy of current lines of melanoma therapy.

Table 2-1. List of reagents and resources

Antibodies		
Anti-AXL (C89E7)	Cell Signaling	Cat#8661
Anti-MITF (D5G7V)	Cell Signaling	Cat#12590
Anti-p75NTR (D4B3) XP® Rabbit mAb	Cell Signaling	Cat#8238
Anti-MART-1 (A103)	Santa Cruz	Cat#sc-20032
Anti-β-Actin (AC-15)	Sigma-Aldrich	Cat#A1978
Anti- p44/42 MAPK (Erk1/2) (L34F12)	Cell Signaling	Cat#4696
Anti-phospho-p44/42 MAPK (Erk1/2) (Thr202/Tyr204) (D13.14.4E)	Cell Signaling	Cat#4370
Anti-STAT1	Cell Signaling	Cat#9172
Anti-pSTAT1 (Y701) (58D6)	Cell Signaling	Cat#9167
Anti-NF-κB p65 (D14E12) XP® Rabbit mAb	Cell Signaling	Cat#8242
Anti-Phospho-NF-κB p65 (Ser536) (E1Z1T)	Cell Signaling	Cat#13346S
IRDye 800CW Goat Anti-Mouse IgG	LI-COR	Cat#926-32210
IRDye 680 Goat Anti-Rabbit IgG	LI-COR	Cat#926-32221
Chemicals, Peptides, and Recombinant Proteins		
Vemurafenib (PLX 4032)	Selleck Chemicals	S1267; CAS: 918504-65-1
Erastin	Selleck Chemicals	S7242; CAS: 571203-78-6
RSL3	Selleck Chemicals	S8155; CAS: 1219810-16-8
Z-VAD-FMK	Selleck Chemicals	S7023; CAS: 187389-52-2
L-Glutathione reduced	Sigma-Aldrich	G4251; CAS: 70-18-8
Piperlongumine	Selleck Chemicals	S7551; CAS: 20069-09-4
Deferoxamine	Sigma-Aldrich	D9533; CAS: 138-14-7
Resazurin	Sigma-Aldrich	R7017; CAS: 62758-13-8
Trolox	Acros Organics	Cat#218940010; CAS: 53188-07-1
Staurosporine	Cayman Chemicals	S1421; CAS: 62996-74-1
Recombinant Human TNFα	Peprotech	Cat#300-01A
Recombinant Human IFNγ	Peprotech	Cat#300-02

Commercial Assays		
Cell-Titer Glo	Promega	G7572
QuantiChrom Glutathione (GSH) Assay Kit	BioAssay Systems	DIGT-250
GenePrint® 10 System	Promega	B9510
AllPrep DNA/RNA Mini kit	Qiagen	Cat#80204
Illumina TruSeq RNA sample preparation kit	Illumina	RS-122-2001
TruPAGE™ Precast Gels 4-12%,	Sigma-Aldrich	PCG2003
Pierce BCA Protein Assay Kit	Thermo Scientific	Cat#23225
CM-H2DCFDA	Life Technologies	C6827
BODIPY 581/591 C11	Life Technologies	D3861
Trypan Blue	Gibco	15250061
IncuCyte Cytotox Red Reagent	Essen Bioscience	Cat#4632

Table 2-2. List of software and algorithms

Software and Algorithms		
GraphPad Prism 6	GraphPad	N/A
TraceFinder Software version 3.3	Thermo Scientific	N/A
ImageStudioLite	LI-COR	www.licor.com/bio/products/software/image_studio_lite/
IncuCyte ZOOM Live-Cell Imaging System	Essen Bioscience	N/A
HISAT2 (v.2.0.5)	(Kim et al., 2015)	https://ccb.jhu.edu/software/hisat2/index.shtml
HTSeq (0.6.1)	(Anders et al., 2015)	https://ccb.jhu.edu/software/hisat2/index.shtml
Tophat2 (v2.0.9)	(Kim et al., 2013)	https://ccb.jhu.edu/software/tophat/
Cufflinks (v2.2.1)	(Trapnell et al., 2012)	http://cole-trapnell-lab.github.io/cufflinks/
Gene Set Enrichment Analysis (GSEA)	(Subramanian et al., 2005)	http://software.broadinstitute.org/gsea/index.jsp
R (v3.2)	N/A	https://www.r-project.org/
ConsensusClusterPlus R Package (v1.38)	(Wilkerson and Hayes, 2010)	http://bioconductor.org/packages/release/bioc/html/ConsensusClusterPlus.html
Conditional Quantile Normalization R Package (v1.20)	(Hansen et al., 2012)	https://bioconductor.org/packages/release/bioc/html/cqn.html
sigclust R Package (v1.1)	(Liu et al., 2008)	https://cran.r-project.org/web/packages/sigclust/index.html
samr R Package (v2.0)	(Tusher et al., 2001)	https://cran.r-project.org/web/packages/samr/index.html

Experimental model and subject details

Human melanoma cell lines were established from patient's biopsies under UCLA IRB approval # 11–003254 as previously described (Søndergaard et al., 2010). A complete list of cell lines can be found in Table S1. Cells were cultured in RPMI 1640 with L-glutamine, 10% fetal bovine serum, and 1% penicillin, streptomycin and fungizone in a water-saturated incubator at 37°C with 5% CO2. Cells were maintained and tested for mycoplasma and authenticated to their early passages using GenePrint® 10 System (Promega).

RNA Extraction, Sequencing, and Analysis

RNA extraction was performed using AllPrep DNA/RNA Mini kit from Qiagen in 53 human melanoma cell lines. Libraries were prepared using the Illumina TruSeq RNA sample preparation kit per the manufacturer's instructions. RNA sequencing was performed using 50 bp paired end sequencing on the Illumina HiSeq 2000 platform. Paired end 50 bp reads generated from the melanoma cell line RNA sequencing were mapped using HISAT2 to the Homo sapiens hg38 genome build and raw counts per quantified using HTSeq. Both the 53 melanoma cell line panel and TCGA raw expected counts were analyzed similarly to reduce technical variability from data processing. Cell line and TCGA raw counts were normalized to FPKM values using conditional quantile normalization (CQN) to adjust for gene length and GC content (Hansen et al., 2012). FPKM values were next transformed in log2 space with an offset of 1. For the vemurafenib treated samples, RNASeq was performed using 50 bp single end sequencing and mapped the Homo sapiens NCBI build 37.2 reference genome using TopHat2 v2.0.9 (Kim et al., 2013) and normalized to fragments per kilobase of exon per million fragments mapped (FPKM) using Cufflinks v2.2.1 and the geometric library size normalization method (Trapnell et al., 2012).

Classification of Cell Lines and Tumors

The top 3000 genes with the highest variance were used for clustering. Consensus complete linkage hierarchical clustering was performed using the Euclidean distance metric and subsampling 75% of samples and genes 1000 times using the *ConsensusClusterPlus* R package. Pairwise cluster significance, as defined by whether each cluster originates from different Gaussian distributions, was performed using the *sigclust* R package. A SVM TSP-based approach as proposed by Shi *et al* (Shi et al., 2011) was used to train the subtype prediction model, where feature selection was performed by hypergeometric test. To have a gene list compatible for all datasets used, we took an intersection of genes from both RNASeq and microarray chip platforms, resulting in 10,545 genes. The top 250 genes were used to build the model. The gene expression matrix was converted into a gene pair binary matrix of relative comparisons for each pair of genes A and B whether A>B as introduced by the "top scoring pairs" method (Shi et al., 2011). For each subtype, pairs were then scored by hypergeometric test to calculate the p-value of enrichment for that subtype compared to the remaining subtypes. Gene-pairs were then filtered by having a minimum p-value of 1e-05 in at least one subtype, resulting in 1561 gene-pairs. The resulting binary matrix of each cell line with identified subtype was used to train the model using a radial basis function kernel with the R package *kernlab*. The model performed at 94% accuracy with leave-one-out cross validation. Gene expression profiles for all datasets for prediction were similarly converted to binary matrices and used as test set for this SVM-based prediction approach.

PCA and Statistical Analysis

Principal component analysis (PCA) was performed on mean centered data and all statistical analyses were performed in R (http://www.R-project.org/). Projections were calculated by matrix multiplication of the centered data to be projected using the rotation matrix determined from the PCA of the original source data.

Significance testing between treatment groups was performed using two-sample t-test. ANOVA p-values were determined using the non-parametric Kruskal-Wallis test at a significance threshold of 0.05. Reported p-values between pairs of subtypes were determined using Dunn post-hoc testing with multiple hypothesis correction using the Benjamini & Hochberg method.

Enrichment Analysis, Subtype Signatures, and Differentiation Trajectory Scores

For subtype comparisons, signal-to-noise ratio of one subtype vs. the remaining three were used to create ranklists. Rank-based enrichment analysis was performed using Gene Set Enrichment Analysis (GSEA) (Subramanian et al., 2005) using the MSigDB C5 GO biological process gene sets. Differential expression analysis used for generating subtype signatures was performed using Significance Analysis of Microarrays at a 5% false discovery rate (FDR) using the *samr* package in R. For average subtype signature scores, z-scores for of all member genes were summed and divided by the number of member genes. To avoid potential confounding issues with gene expression from non-tumor sources, genes correlated with the immune and keratin signature were not included. Differentiation trajectory position score was determined using a center of mass approach where all single subtype and transitional-paired subtype average signature scores were summed in a weighted fashion. Weighting represented the relative position along the differentiation trajectory (i) running from 1 to 7 for undifferentiated, undifferentiated-neural crest like pair, neural crest like, neural crest like-transitory pair, transitory, transitory-melanocytic pair, and melanocytic. The formula is given by:

$$Differentiation\ Trajectory\ Position\ = \frac{\sum_{i=1}^{7} m_i \cdot i}{\sum_{i=1}^{7} m_i}$$

where m_i are the seven signature scores.

Immune and Keratin Confounding Signature Criteria

A starter list of immune genes was obtained from the Immunome database, downloaded from InnateDB (http://www.innatedb.com). PCA was used to reduce dimensionality of the list of immune genes to a single immune score (PC1). The total list of immune confounded genes was determined by identifying genes that were correlated to the immune score above a threshold value. The threshold correlation was determined using an ROC analysis, comparing distributions of correlations of genes within the immune starter list vs. all others. Keratin confounded genes was identified similarly, using genes annotated as keratins from the NCBI gene database (http://www.ncbi.nlm.nih.gov/gene/) as the starter list of genes.

Methylation Analysis

Human tumor methylation 450K array data was obtained from The Cancer Genome Atlas. Cell line methylation 450K array data was obtained from GSE68379. Probes excluded from the downstream analysis were probes with poor detection quality, probes mapping to sex chromosomes, probes with known SNPs at the CG site, and 29,233 probes previously shown to be cross-reactive with genes on sex chromosomes (Chen et al., 2013).Using the UCSC gene annotation, probes mapping to the promoter (TSS1500, TSS200, 5'UTR, and 1stExon) were collapsed to gene level by averaging the sites mapping to each gene. Probes mapping to CG islands and probes mapping to multiple genes were excluded, resulting in gene-level promoter methylation values for 15,580 genes for the cell line data and 14,318 genes for the TCGA data.

Deposited Data

Data is deposited in the Gene Expression Omnibus (GEO) database under accession number GSE80829.

Public Data Resources

Dataset from Mica *et al* for the melanocyte differentiation stage analysis was obtained from GSE45227. Gene expression profiles from samples representing the growth conditions for each specified stage of differentiation based on the original manuscript was used for analysis (day 0 embryonic stem cell, day 6 neural crest cell, day 11 melanoblast, and day 25 melanocyte). Primary melanocyte expression profiles (adult and neonatal) were used as control.

Data from the CCLE (expression) and GSDC (expression and methylation) databases were downloaded from the respective resource websites (http://www.broadinstitute.org/ccle; http://www.cancerrxgene.org/downloads). For expression analysis, microarray probes were collapsed to gene symbol to the maximum average probe. Pharmacogenomic data from the CTRP was downloaded from the Cancer Target Discovery and Development (CTD^2) data portal (https://ocg.cancer.gov/programs/ctd2/data-portal). For subtype annotations of cell lines used in the pharmacogenomics analysis, we used our support vector machine (SVM)-based classifier and merged both the CCLE and GDSC predictions. We excluded 6 cell lines that either had mismatched or non-confident classifications, resulting in 43 lines analyzed (1 assayed in duplicate by the CTRP).

For the data from Landsberg *et al*, expression profiles were obtained from GSE40213. Mouse genes were mapped to human homologs using the NCBI HomoloGene database. To account for any genes that might not vary in a mouse and could dilute signal when switching to human analysis, a variance filter of 0.3 was applied.

RNASeq raw expected counts (RNASeqV2) and DNA methylation beta values (HM450K) of skin cutaneous melanoma (SKCM) bulk tumors from The Cancer Genome Atlas (TCGA) were downloaded from the data portal (http://tcga-data.nci.nih.gov).

For MAPKi treated data, RSEM TPM expression values of patient tumor samples on-treatment from Kwong *et al* were obtained from European Genome-phenome Archive (EGA S00001000992). FPKM values for single and double drug MAPKi resistant cell lines and

disease progression tumors from Hugo *et al* were obtained from GSE65186. For these disease progression tumors, dedifferentiation was determined by MITF downregulation or PDGFRB upregulation as previously observed (Müller et al., 2014). MAPK reactivation was determined by upregulation, amplification or alternative splicing of BRAF, or upregulation or mutation of NRAS (Corcoran et al., 2010; Nazarian et al., 2010; Poulikakos et al., 2011). Mixed / heterogeneous response cases had biomarkers for both mechanisms. FPKM values of disease progression tumors from Tirosh *et al* were obtained from GSE77940.

Clonogenic Survival, Viability and Cytotoxicity Assays

For the BRAFi timecourse study, M229 was treated with vemurafenib or DMSO for the indicated timepoints at twice the 50% inhibition concentration (500 nM). For the crystal violet assays, 2.5 x 10^5 cells were plated in 6-well plates. The next day media was replaced by drug media and replenished every 2-3 days. Plates were stained with crystal violet solution (1% crystal violet, 50% methanol). Control wells were grown for 1 week and stained when 100% confluent.
For measurement of percent viable cells with treatment, cells were plated at 5000 cells per well and the next day treated with drug. Percentage cell viability is reported as a percentage relative to the negative control treatment. Dose-response curves were assayed using CellTiter-Glo (Promega) luminescent cell viability assay. IC50 values were obtained by fitting the data to nonlinear regression with variable slope using GraphPad Prism. For other viability measurements, an resazurin-based assay (*a.k.a.* Alamar Blue) was used and fluorescence was measured at 570/600 ex/em wavelength. Measurement of dead cells per time was measured by incubating treated cells with the IncuCyte Cytotox Red Reagent and imaging with IncuCyte ZOOM Live-Cell Imaging System (Essen BioScience). For measurement of cell death, Trypan blue exclusion assay was used.

Analysis of Reactive Oxygen Species Production

In 12-well plates, 100,000 cells per well were seeded and allowed to attach for approximately 12 hours. Cells were then treated with media containing 5 μM of erastin, 100 μM deferoxamine or a combination of both, and returned to the 37°C tissue culture incubator. After 10 hours, drug media was replaced by media containing DMSO control, 5 μM of CM-H2DCFDA dye (Life Technologies, C6827), or 5 μM of C11-BODIPY (Life Technologies, D3861) and incubated for another 20 min at 37°C. Cells were then washed with PBS, harvested by trypsinization, followed by another wash with PBS. Cells were resuspended in 400μL PBS, strained through a 35μm nylon mesh filter, and analyzed by flow cytometry using BD LSRII equipped with 488 nm laser for excitation (BD Biosciences).

Immunoblotting

Cells were lysed in modified RIPA buffer (50 mM Tris–HCl (pH 7.5), 150 NaCl, 10 mM β-glycerophosphate, 1% NP-40, 0.25% sodium deoxycholate, 10 mM sodium pyrophosphate, 30 mM sodium fluoride, 1 mM EDTA, 1 mM vanadate, 20 μg/ml aprotinin, 20 μg/ml leupeptin, and 1 mM phenylmethylsulfonyl fluoride). Whole-cell lysates were resolved by SDS–PAGE on TruPAGE 4–15% gradient gels (Sigma-Aldrich) and blotted onto nitrocellulose membranes. Membranes were blocked overnight with 5% milk and then incubated sequentially with primary and then IRDye-conjugated secondary antibodies (Li-Cor). Blots were imaged using the Odyssey Infrared Imaging System (Li-Cor).

GSH Measurement

Levels of GSH were measured using the colorimetric QuantiChrom Glutathione Assay Kit (BioAssay Systems) according to the kit instructions. Briefly, $2x10^6$ cells were plated on 10 cm dishes. The next day, cells were scraped with cold PBS and centrifuged at 1000g for 10 minutes

at 4° C. Cells were re-suspended in 1 mL cold phosphate buffer (50mM phosphate, 1 mM EDTA, ph=6.5) and lysed by sonication. Lysates were spun down at 10,000g for 15 min at 4° C. The supernatant was split into two for measurement of GSH using the kit reagents, and protein quantification using the BCA Protein Assay Kit from Pierce Biotechnology.

Mass spectrometry-based metabolomic analyses

In 6-well plates, 200,000 cells per seeded per well and allowed to attach over night. The next day, media was replaced with media containing 5 μM of erastin. After 8 hr of treatment, cells were washed with ice-cold 150 mM ammonium acetate (NH_4AcO) pH 7.3 and metabolites extracted in 1 ml ice-cold 80% MeOH. The cells were quickly transferred into a microfuge tube, and 10 nmol norvaline was added to the cell suspension for use as an internal standard. The suspension was subsequently vortexed three times over 15 min and then spun down at 4°C for 5 min. The supernatant was transferred into a glass vial, the cell pellet was re-extracted with 200 μl ice-cold 80% MeOH and spun down and the supernatants were combined. Metabolites were dried at 30°C under vacuum and re-suspended in 50 μl of 70% acetonitrile (ACN).

Samples were run on a Q-Exactive mass spectrometer coupled to an UltiMate 3000RSLC UHPLC system (Thermo Scientific). The mass spectrometer was run in polarity switching mode (+3.00 kV/−2.25 kV) with an m/z window ranging from 65 to 975. Mobile phase A was 5 mM NH_4AcO, pH 9.9, and mobile phase B was ACN. Metabolites were separated on a Luna 3 μm NH2 100 Å (150 × 2.0 mm) (Phenomenex) column. The flow was kept at 200 μl/min, and the gradient was from 15% A to 95% A in 18 min, followed by an isocratic step for 9 min and re-equilibration for 7 min. Metabolites were detected and quantified as area under the curve (AUC) based on retention time and accurate mass (≤ 3 ppm) using the TraceFinder 3.1 (Thermo Scientific) software. Samples were normalized by protein concentration measured using the BCA Protein Assay Kit from Pierce Biotechnology. All samples were run as biological triplicates, and consistent results were seen in independent experiments.

PERSPECTIVES AND FUTURE STUDIES

Our molecular classification analysis of melanoma cell lines led to the identification of four subtypes that reflected progressive step-wise differentiation states. This refined framework of melanoma differentiation can guide new discoveries in melanoma biology. As differences in differentiation state can yield fundamentally different cellular properties, it can potentially help reconcile heterogeneity of phenotypes and responses to therapy. For example, a high MITF differentiated transcriptional state was found to be more dependent on MAPK pathway signaling and therefore more sensitive to inhibition of the pathway (Konieczkowski et al., 2014a; Müller et al., 2014).

In our work we integrated our differentiation framework with publicly available pharmacogenomics resources to uncover a new dedifferentiation-associated vulnerability to drug-induced ferroptosis. Dedifferentiation is a recurrent innate and acquired resistance mechanism to modern kinase targeted therapies and immunotherapies in the clinic. Thus, this discovery offers a new co-treatment option targeted directly at the dedifferentiation-based resistance escape route that limits the efficacy of current lines of melanoma therapy. However, the mechanisms as to why less differentiated cells are more sensitive to ferroptosis induction is not fully clear. Further understanding these mechanisms will be essential in optimizing ferroptosis induction for the treatment of melanoma.

Treatment with ferroptosis inducing drugs *in vivo*

Our experimental results thus far provide compelling evidence that ferroptosis inducing drugs would be a new therapeutic avenue to treat dedifferentiation-associated therapy resistant melanomas. However, these functional studies were carried out *in vitro* and the question remains whether the sensitivity of dedifferentiated cells to undergo ferroptosis would be recapitulated *in vivo* where the level of nutrients and metabolism would be different. Since

melanoma cells are highly plastic and can switch differentiation states *in vivo* (Hoek et al., 2008b), combinatorial treatments that target both states would be predicted to be more effective than single agent therapies. Preclinical studies by others have shown that ferroptosis inducing drugs such as erastin and RSL3 do have *in vivo* anti-tumor efficacy and are well tolerated, but currently remain limited due to poor pharmacokinetics (Yang et al., 2014). Once new ferroptosis drugs with improved bioavailability are identified, further *in vivo* studies to investigate combination therapy with MAPK pathway inhibitors or immunotherapy drugs is warranted.

Differentiation state and regulation of oxidative stress

Melanocytes have vital antioxidant stresses and defenses inherent to their biology, owing to the high oxidative stress from melanin biosynthetic processes and UV radiation (Denat et al., 2014). Thus, it logical that differentiated melanoma cells, which are more similar to normal melanocytes, are better able to withstand induction of lipid ROS and ferroptosis. The loss of differentiation programs that combat redox stresses could render redox-challenged cancer cells susceptible to oxidative stress. High MITF cells were found to be more resistant to H_2O_2-induced cell death through MITF transcriptional upregulation of the redox sensor APE-1 (Liu et al., 2009). MITF has also been shown to drive the expression of PGC1α, a key transcription factor regulating mitochondria biogenesis and expression of ROS detoxifying enzymes (Vazquez et al., 2013). Genetic experiments modulating MITF or other associated transcription factors could uncover the role of melanocyte differentiation in protecting cells from accumulation of oxidative stress.

Metabolic regulation of lipid redox in melanoma

When ferroptosis-sensitive and -resistant isogenic melanoma cell lines were treated with erastin, levels of reduced (GSH) and oxidized (GSSG) glutathione were greatly depleted in both lines, albeit at different magnitudes. We found that the levels of reduced and total glutathione

were lower in undifferentiated melanomas, and accordingly low glutathione levels are linked to ferroptosis sensitivity. The ferroptosis insensitive lines, despite having a considerable depletion of GSH, had no detectable level of lipid ROS at the measured time-point. There could be many contributing factors as to why these insensitive lines do not generate high levels of lipid ROS. The levels of cellular iron, activity of the iron-dependent ROS producing enzymes such as lipoxygenases, and availability of oxidizable polyunsaturated fatty acids in the lipid membrane have been shown contribute to the production of lipid ROS and sensitivity to ferroptosis (Dixon et al., 2012; Doll et al., 2017; Xie et al., 2016; Yang et al., 2016). Assays to measure the available labile iron and lipidomics to profile the phospholipid composition could shed light on the factors driving the differential amounts of lipid ROS between the ferroptosis sensitive and insensitive lines.

Alternatively, the ferroptosis insensitive cells may have an increased capacity to quickly detoxify the generated lipid ROS. The reaction to detoxify lipid ROS is carried out by GPX4, which also converts to GSH to GSSG as a reducing equivalent. GSH can be regenerated by glutathione reductase (GSR) requires NADPH. Engagement of metabolic pathways that generate NADPH can therefore promote the regeneration of GSH and the capacity of cells to maintain low ROS levels (Gorrini et al., 2013). Accordingly, low basal levels of NADPH were found to be predictive of sensitivity to ferroptosis across multiple cancer cell lines (Shimada et al., 2016). NADPH can be produced from the oxidative pentose phosphate pathway, folate metabolism, the conversion of malate to pyruvate through malic enzyme 1 (ME1), or the conversion of isocitrate to α-ketoglutarate by isocitrate dehydrogenase 1 and 2 (IDH1, IDH2) (Fan et al., 2014; Gorrini et al., 2013). Metabolomic profiling and flux analysis of the ferroptosis insensitive cells compared to the sensitive cells could reveal which metabolic pathways are involved in melanoma adaptation and survival under oxidative stress. Collectively, a greater understanding of the metabolism of melanoma cells could guide development of new combination therapies by modulating oxidative stress.

Oxidative stress and metastasis

Recently, it was shown that metastasizing melanoma cells experienced high levels of oxidative stress and successful metastasis is dependent on metabolic adaptations that increase GSH regeneration (Piskounova et al., 2015). This adaptation was also found to be dependent on NADPH generating enzymes, most notably of the folate pathway. Since metastasizing cells are under oxidative stress, we would expect that these cells would have a heightened sensitivity to ferroptosis induction due to lower levels of NADPH and GSH. Future studies with *in vivo* metastatic models could determine if treatment with ferroptosis inducing drugs could have an additional benefit of limiting distant metastasis, which would significantly improve patient survival.

APPENDIX

The selected work described here are a result of collaborative efforts to advance the understanding of melanoma and treatment response through bioinformatic analysis. In each of the following studies, my contributions were to the processing, analysis, and interpretation of microarray or RNA sequencing gene expression data that have guided the design and conclusions of specific experiments in the paper.

Improved antitumor activity of immunotherapy with BRAF and MEK inhibitors in *BRAF^{V600E}* melanoma

Targeted therapy for the treatment with *BRAF^{V600E}*-driven melanoma with oncogenic BRAF inhibitors have led to high response rates, but side effects occur due to the paradoxical activation of BRAF in wild-type cells. The addition of downstream MEK inhibitors has helped alleviate these toxicities and has resulted in improved survival compared to the BRAF monotherapy alone. However, targeted MAPK inhibitor (MAPKi) therapy is limited by the inability to achieve durable responses due to the development of resistance. This is in contrast to treatment with immunotherapy, which has led to remarkable durable responses in patients. Therefore, the combination of all three can potentially achieve a greater antitumor effect by incorporating the rapid response rates of targeted therapy and durability of immunotherapy. However, it remains unknown whether MEK inhibition will dampen the immune response. In this study, we evaluate the feasibility of the triple combination therapy.

We show that in a syngeneic mouse model of *BRAF^{V600E}*-driven melanoma, the triple combination therapy including dabrafenib, trametinib, and adoptive cell transfer (ACT) immunotherapy of gp100 antigen specific T cells (pmel cells) resulted in enhanced antitumor effect with complete tumor regression and increased T cell infiltration. Gene expression analysis of harvested tumors at day 5 after ACT shows that pmel ACT with dabrafenib and/or trametinib treated tumors cluster distinctly from the other treatment groups (Figure A-1A). Moreover, there were three unique immune signature profiles among the treatment groups (Figure A-1B). Immune A genes are upregulated after treatment with dabrafenib, trametinib, or the combination with either mock or pmel ACT. Immune B genes are upregulated after treatment with dabrafenib, trametinib, or the combination and receiving pmel ACT but not the mock ACT. Immune C genes were those downregulated by dabrafenib or trametnib treatment in mock or pmel ACT. There was an general increase of chemokines and their receptors gene expression with treatment of pmel ACT with dabrafenib or trametnib, and more so with the triple

combination (Figure A-1C). Treatment with dabrafenib, trametinib, or the combination resulted upregulation of melanosomal antigens (Figure A-1D), which can promote antigen specific T cell recognition. MHC expression were also upregulated with treatment of dabrafenib and/or trametinib combined with pmel ACT, but not mock ACT. This indicated that the antigen-specific effector cells were important for the MHC upregulation.

In summary, our gene expression analysis suggested that the heightened antitumor response in the triple combination therapy is from improved T cell recognition by upregulation of melanocytic antigen and MHC gene expression. There was a strong global upregulation of immune-related gene expression with the triple combination treatment, further supporting an increase of immune infiltration in this treatment group.

Reference:

Hu-Lieskovan, S., Mok, S., Moreno, B.H., Tsoi, J., Robert, L., Goedert, L., Pinheiro, E.M., Koya, R.C., Graeber, T.G., Comin-Anduix, B., and Ribas, A. (2015). Improved antitumor activity of immunotherapy with BRAF and MEK inhibitors in BRAFV600E melanoma. Sci Transl Med 7, 279ra41-279ra41.

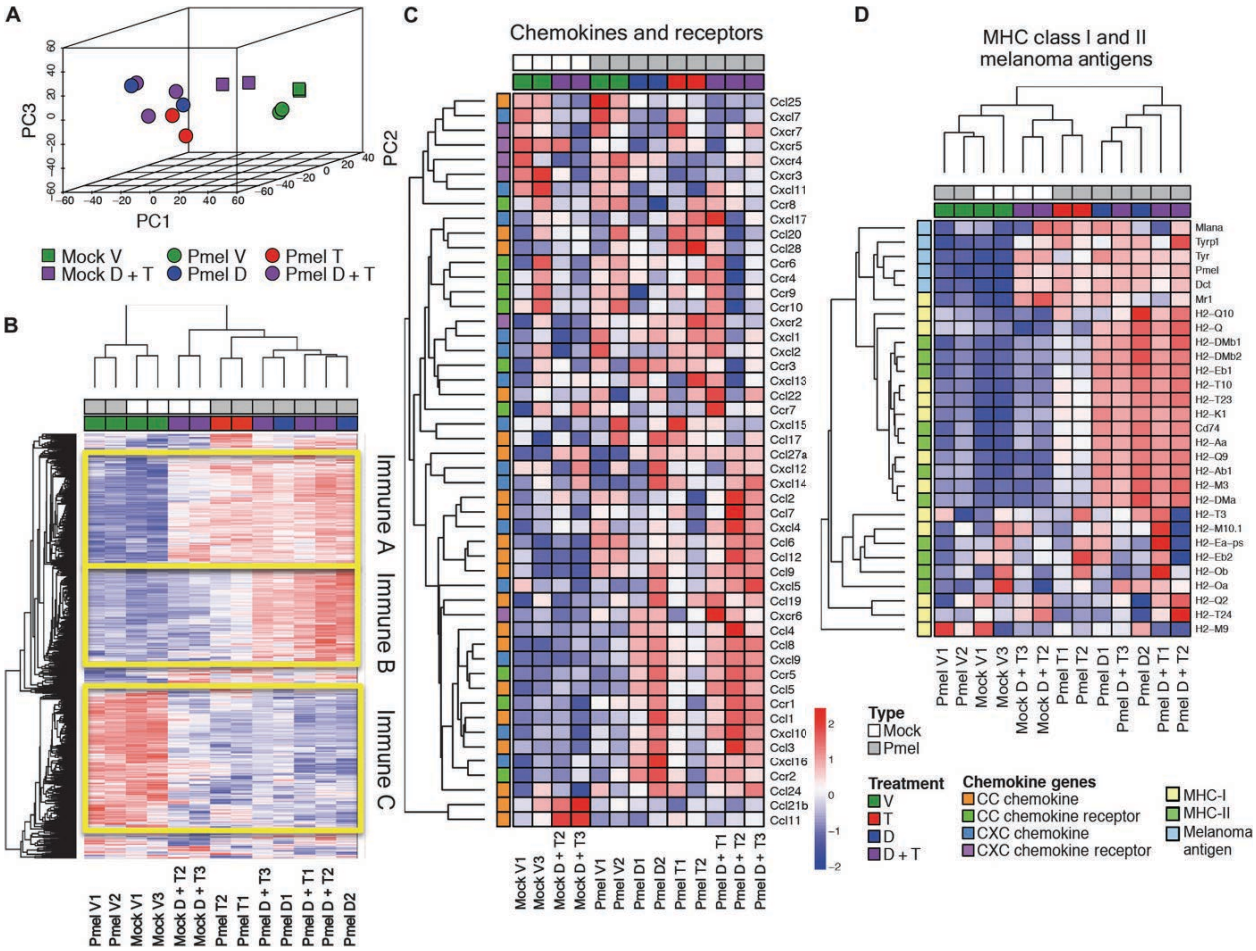

Figure A-1. Microarray analysis of tumors treated by dabrafenib, trametinib, or the combination of dabrafenib and trametinib with pmel-1 ACT or mock ACT.
On day 5 after ACT, tumors were isolated and snap-frozen immediately (two to three mice in each group). RNA isolation was done after all samples were collected. (A) PCA of gene expression profile of the tested samples. (B) Clustering of immune-related genes with analysis of variance (ANOVA) filter, $P < 0.05$. Gene names in individual clusters are listed in tables S1 to S3. (C) Clustering of chemokines and their receptors. (D) Clustering of MDAs and MHC class I and II molecules. See reference for additional detail. Figure is adapted from Figure 5 of Hu-Lieskovan et al, 2015.

Inhibition of colony stimulating factor-1 receptor improves antitumor efficacy of BRAF inhibition

Targeted therapy with oncogenic BRAF inhibitors also have an additional immune potentiating effect, due to paradoxical activation of wild-type BRAF in tumor-infiltrating lymphocytes (TILs) that increases cytotoxic activity and IFN-γ production. However, melanoma cells can secrete the cytokine colony stimulating factor 1 (CSF1) to promote an immunosuppressive microenvironment to promote immune escape. Engagement of CSF1 to CSF1 receptor can induce the differentiation and polarization of M2 macrophages and myeloid derived suppressor cells. In this study, we show in the SM1 murine melanoma model that combination therapy of oncogenic BRAF inhibitor PLX4032 and CSF1R inhibitor PLX3397 results an increase in TILs and heightened antitumor response that is T-cell dependent.

Gene expression analysis of the SM1 tumors was performed following treatments with PLX3397, PLX4032, or the combination for 5 days. We determined the presence of monocytic or T cell immune populations within the tumor by using the rank-based overlap tool Rank-Rank Hypergeometic Overlap (RRHO) with reference immune signatures from the Differentiation Map Portal (DMAP). We compared the differential expression between each of the treated groups from vehicle control with the differential expression between monocytes and T cells. Our RRHO overlap analysis suggest that for all treated groups, there is a stronger T cell signature with the higher signal in the combination therapy group (Figure A-2, A-C).

Additionally, we looked into the immune specific gene expression from F4/80+ CD11b+ macrophages and CD3+ CD8+ T-cells. Within the macrophage gene expression dataset, we observed a downregulation of the immunosuppressive M2 polarized macrophage-related gene expression such as *Arg1*, *IL-10*, *CD163*, and *MSR1.* This downregulation was present in all treatment groups, but was stronger in the combination therapy (Figure A-2D). Within the CD8+ T cell dataset, we observed upregulation of T cell activation genes such as *IFN-γ, Gzmb,* and *Pdcd1*. This upregulation was again present in all treatment groups, but strongest in the

combination therapy treatment group (Figure A-2E). Taken together, our results suggests that the improved antitumor response from PLX3397 and PLX4032 treatment can be attributed to the combined effect of both drugs. PLX3397 treatment decreases the immunosuppressive M2-polarized macrophages from PLX3397 treatment, which then promotes T-cell infiltration, while PLX4032 treatment augments T-cell activation and cytotoxic response.

Reference:

Mok, S., Tsoi, J., Koya, R.C., Hu-Lieskovan, S., West, B.L., Bollag, G., Graeber, T.G., and Ribas, A. (2015). Inhibition of colony stimulating factor-1 receptor improves antitumor efficacy of BRAF inhibition. BMC Cancer 15, 356.

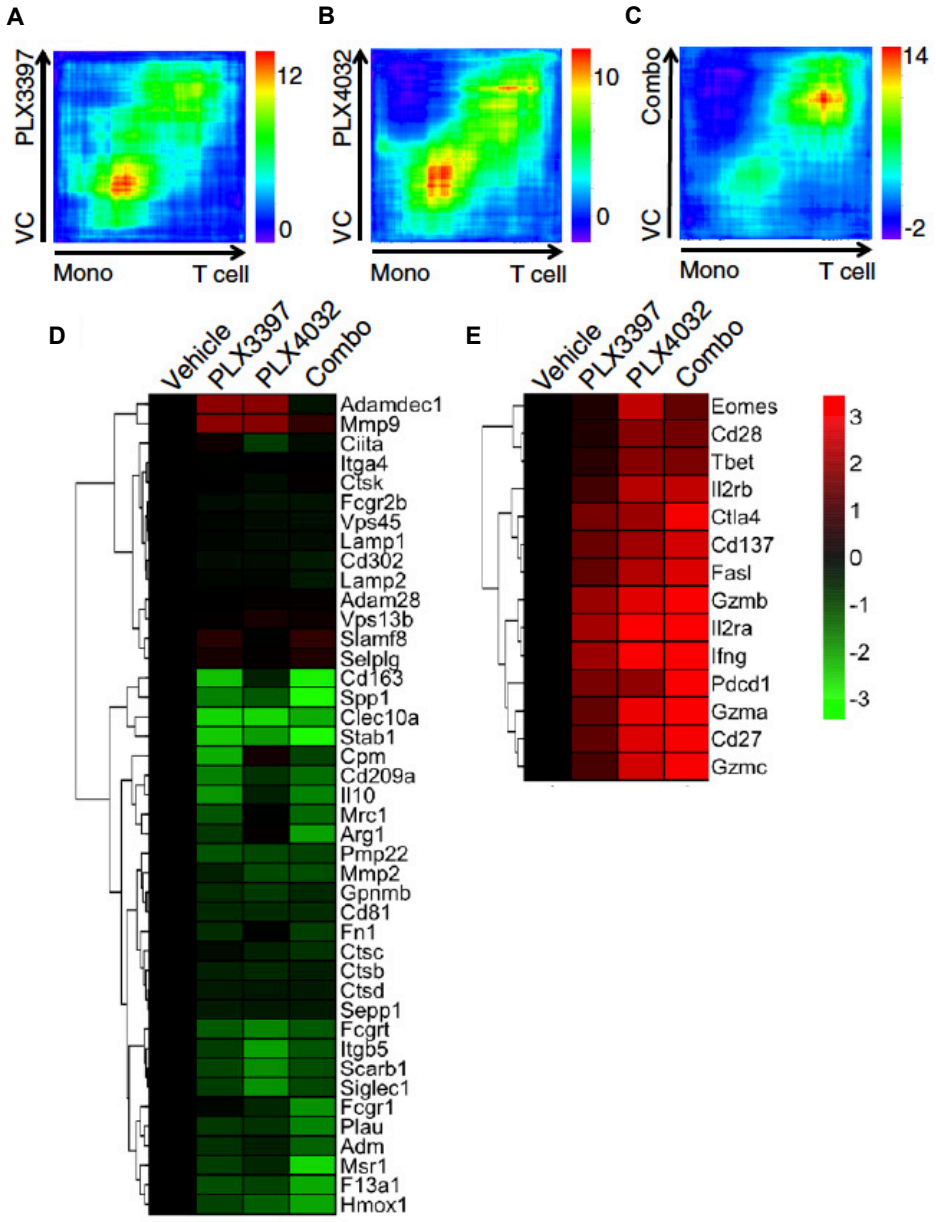

Figure A-2. *In vivo* T-cell activation and suppression of macrophages mediated by PLX3397 and PLX4032. Gene expression signature overlap maps were used to compare the similarity of drug-treated full tumor gene expression profiles with a panel of T-cell and monocyte (Mono) gene signatures from a reference immune cell signature database (the Rank-Rank Hypergeometric Overlap (RRHO) algorithm and the Differentiation Map (DMAP) database), (A) PLX3397 treatment vs vehicle control (VC); (B) PLX4032 vs vehicle; (C) combined drug treatment (Combo) vs vehicle. (D) Gene expression heat map for macrophage signature genes in F4/80(+) CD11b(+) macrophages FACS-sorted from SM1 tumors treated with PLX3397 or PLX4032 for 5 days. (E) Gene expression heat map for T-cell signature genes in CD3(+) CD8(+) T-cells from SM1 tumors. Color scale, log2-transformed fold change expression (red, high; green, low) for each gene (row) normalized to the value for the vehicle control-treated tumors. See reference for more detail. Adapted from Figure 5 from Mok et al, 2015.

CRAF R391W is a melanoma driver oncogene

While the majority of melanomas have driver mutations in BRAF or NRAS, there remains a subset of melanomas with no known driver mutation. In this study, we identify a rare and novel driver mutation in a patient with melanoma that is wild-type to BRAF and NRAS. Although wild-type for BRAF and NRAS, the cell line derived from the patient biopsy, M375, was highly sensitive to pan-RAF and MEK inhibition (Figure A-3A). Additionally, M375 had signaling patterns similar to the BRAF mutant cell line M397, as indicated by substantially higher phosphorylation of MEK and ERK that can be suppressed by pan-RAF inhibition. As negative controls, BRAF/NRAS wild-type cell lines M230 and PB have lower phosphorylation levels of MEK and ERK, and are less affected by RAF inhibition (Figure A-3, B-C). Therefore, we hypothesized that M375 had a previously undiscovered MAPK pathway mutation driving the oncogenic phenotype.

Through RNA sequencing analysis, we found that the levels of CRAF were substantially higher in M375 than any of the other tested cell lines (Figure A-3D). Due to the higher RNASeq transcript levels, we were able to confidently perform mutation calling of the CRAF locus and identified a homozygous *CRAF* A1171T missense mutation (R391W). This mutation was confirmed by Sanger sequencing to be a homozygous mutation that is present in the original patient biopsy and therefore not an artifact of cell culture (Figure A-3E). Additionally, this mutation is not present in normal blood cells, indicating that it is a somatic mutation. The levels of this CRAF protein were also strongly elevated (Figure A-3F), suggesting a functional importance for the mutated kinase.

In summary, our RNA sequencing analysis and cell line phenotype information has led to the discovery of the CRAF R391W mutation. The abundant transcript levels and homozygosity of this mutation all indicate a selective advantage of this mutation and its importance. Further validation experiments guided by this discovery have confirmed that CRAF R391W is a novel oncogene. In CRAF wild-type cells, exogenous expression enables CRAF continuous

homodimerization, increased MAPK signaling activity, can confer resistance to BRAF inhibition, and supports anchorage independent growth in NIH3T3 cells. Experimental details can be found in the original referenced manuscript.

Reference:

Atefi, M., Titz, B., Tsoi, J., Avramis, E., Le, A., Ng, C., Lomova, A., Lassen, A., Friedman, M., Chmielowski, B., Ribas, A., and Graeber, T.G. (2016). CRAF R391W is a melanoma driver oncogene. Sci Rep 6, 27454.

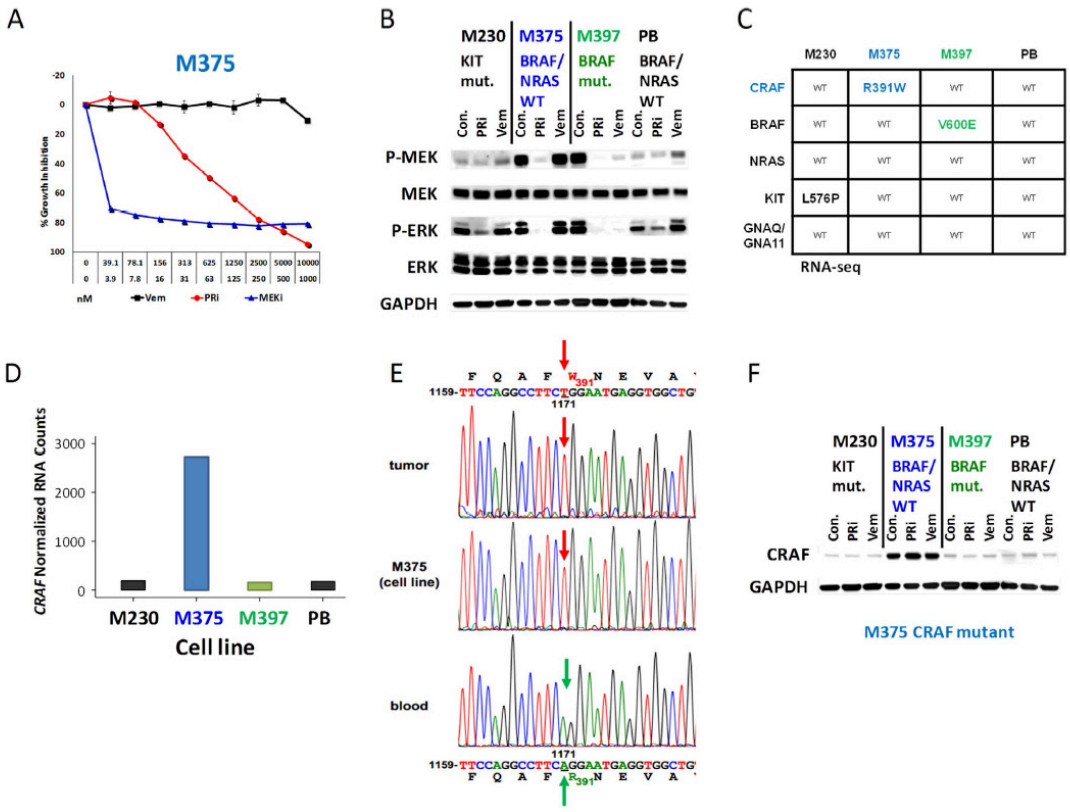

Figure A-3. Identification of CRAF R391W as a candidate melanoma oncogene in a BRAF WT/NRAS WT cell line (M375) and matched patient sample. (**A**) Growth inhibition assay demonstrates sensitivity of the BRAF/NRAS wild type cell line M375 to pan-RAF inhibitor (PRi) and MEK inhibitor (MEKi) and its resistance to the BRAF inhibitor vemurafenib. M375 was treated with serial dilutions of these drugs in duplicate. MEKi concentration was 1/10 of the PRi and vemurafenib concentration for each dilution. The assay was repeated twice. Error bars indicate the standard error. (**B**) MAP-kinase signaling and inhibitor treatment response of CRAF mutant M375 cells is reminiscent of BRAF mutated cells except for lack of vemurafenib sensitivity. Western blot assay was performed on CRAF mutant M375, c-KIT mutant M230, BRAF mutant M397 and NRAS/BRAF wild type PB cell lines to analyze their MAPK pathway activities at basal levels or after treatment with 1.0 µM of PRi or vemurafenib for 24 hours. (**C**) RNA-seq analysis of M375 reveals a homozygous *CRAF* A1171T mutation (CRAF R391W). RNA-seq analysis was performed for the M375, M230 (c-KIT mutant), M397 (BRAF mutant), and PB (BRAF WT/NRAS WT) cell lines. For discovery of the CRAF R391W mutation all mutations detected in the sequencing data were filtered for potentially damaging mutations in the MAP kinase pathway (see methods). The table shows the detected mutations in the common melanoma oncogenes and CRAF for the four cell lines. (**D**) mRNA expression of CRAF in the four cell lines as determined by RNA-seq analysis. M375 shows >10x higher expression of CRAF (R391W). (**E**) *CRAF* A1171T/R391W mutation in M375 and its corresponding tumor is the result of a somatic mutation. Sanger sequencing was performed on the genomic DNA samples isolated from M375 cell line, its corresponding tumor and matched blood of the patient. Sequencing confirmed the presence of *CRAF* A1171T mutation in the tumor, its derived cell line (M375), but not in the blood of the patient. (**F**) Western blot analysis shows strongly elevated abundance of CRAF protein levels in the CRAF mutated melanoma cell line M375 in comparison with 3 other melanoma cell lines. See reference for more details. Adapted from Figure 1 from Atefi et al, 2016.

REFERENCES

Akbani, R., Akdemir, K.C., Aksoy, B.A., Albert, M., Ally, A., Amin, S.B., Arachchi, H., Arora, A., Auman, J.T., Ayala, B., et al. (2015). Genomic Classification of Cutaneous Melanoma. Cell *161*, 1681–1696.

Alexandrov, L.B., Nik-Zainal, S., Wedge, D.C., Aparicio, S.A.J.R., Behjati, S., Biankin, A.V., Bignell, G.R., Bolli, N., Borg, A., Børresen-Dale, A.-L., et al. (2013). Signatures of mutational processes in human cancer. Nature *500*, 415–421.

Alizadeh, A.A., Eisen, M.B., Davis, R.E., Ma, C., Lossos, I.S., Rosenwald, A., Boldrick, J.C., Sabet, H., Tran, T., Yu, X., et al. (2000). Distinct types of diffuse large B-cell lymphoma identified by gene expression profiling. Nature *403*, 503–511.

Allen, E.M.V., Wagle, N., Sucker, A., Treacy, D.J., Johannessen, C.M., Goetz, E.M., Place, C.S., Taylor-Weiner, A., Whittaker, S., Kryukov, G.V., et al. (2014). The Genetic Landscape of Clinical Resistance to RAF Inhibition in Metastatic Melanoma. Cancer Discovery *4*, 94–109.

Anders, S., Pyl, P.T., and Huber, W. (2015). HTSeq—a Python framework to work with high-throughput sequencing data. Bioinformatics *31*, 166–169.

Balch, C.M., Gershenwald, J.E., Soong, S., Thompson, J.F., Atkins, M.B., Byrd, D.R., Buzaid, A.C., Cochran, A.J., Coit, D.G., Ding, S., et al. (2009). Final Version of 2009 AJCC Melanoma Staging and Classification. JCO *27*, 6199–6206.

Barretina, J., Caponigro, G., Stransky, N., Venkatesan, K., Margolin, A.A., Kim, S., Wilson, C.J., Lehár, J., Kryukov, G.V., Sonkin, D., et al. (2012). The Cancer Cell Line Encyclopedia enables predictive modelling of anticancer drug sensitivity. Nature *483*, 603–607.

Bogunovic, D., O'Neill, D.W., Belitskaya-Levy, I., Vacic, V., Yu, Y.-L., Adams, S., Darvishian, F., Berman, R., Shapiro, R., Pavlick, A.C., et al. (2009). Immune profile and mitotic index of metastatic melanoma lesions enhance clinical staging in predicting patient survival. PNAS *106*, 20429–20434.

Brichard, V., Pel, A.V., Wölfel, T., Wölfel, C., Plaen, E.D., Lethé, B., Coulie, P., and Boon, T. (1993). The tyrosinase gene codes for an antigen recognized by autologous cytolytic T lymphocytes on HLA-A2 melanomas. Journal of Experimental Medicine *178*, 489–495.

Carter, S.L., Cibulskis, K., Helman, E., McKenna, A., Shen, H., Zack, T., Laird, P.W., Onofrio, R.C., Winckler, W., Weir, B.A., et al. (2012). Absolute quantification of somatic DNA alterations in human cancer. Nat Biotech *30*, 413–421.

Chapman, P.B., Hauschild, A., Robert, C., Haanen, J.B., Ascierto, P., Larkin, J., Dummer, R., Garbe, C., Testori, A., Maio, M., et al. (2011). Improved Survival with Vemurafenib in Melanoma with BRAF V600E Mutation. New England Journal of Medicine *364*, 2507–2516.

Chen, Y., Lemire, M., Choufani, S., Butcher, D.T., Grafodatskaya, D., Zanke, B.W., Gallinger, S., Hudson, T.J., and Weksberg, R. (2013). Discovery of cross-reactive probes and polymorphic CpGs in the Illumina Infinium HumanMethylation450 microarray. Epigenetics *8*, 203–209.

Cheng, P.F., Shakhova, O., Widmer, D.S., Eichhoff, O.M., Zingg, D., Frommel, S.C., Belloni, B.,

Raaijmakers, M.I., Goldinger, S.M., Santoro, R., et al. (2015). Methylation-dependent SOX9 expression mediates invasion in human melanoma cells and is a negative prognostic factor in advanced melanoma. Genome Biology *16*, 42.

Corcoran, R.B., Dias-Santagata, D., Bergethon, K., Iafrate, A.J., Settleman, J., and Engelman, J.A. (2010). BRAF Gene Amplification Can Promote Acquired Resistance to MEK Inhibitors in Cancer Cells Harboring the BRAF V600E Mutation. Sci. Signal. *3*, ra84-ra84.

Davies, H., Bignell, G.R., Cox, C., Stephens, P., Edkins, S., Clegg, S., Teague, J., Woffendin, H., Garnett, M.J., Bottomley, W., et al. (2002). Mutations of the BRAF gene in human cancer. Nature *417*, 949–954.

Denat, L., Kadekaro, A.L., Marrot, L., Leachman, S.A., and Abdel-Malek, Z.A. (2014). Melanocytes as Instigators and Victims of Oxidative Stress. Journal of Investigative Dermatology *134*, 1512–1518.

Dhillon, A.S., Hagan, S., Rath, O., and Kolch, W. (2007). MAP kinase signalling pathways in cancer. Oncogene *26*, 3279–3290.

Dixon, S.J., Lemberg, K.M., Lamprecht, M.R., Skouta, R., Zaitsev, E.M., Gleason, C.E., Patel, D.N., Bauer, A.J., Cantley, A.M., Yang, W.S., et al. (2012). Ferroptosis: An Iron-Dependent Form of Nonapoptotic Cell Death. Cell *149*, 1060–1072.

Doll, S., Proneth, B., Tyurina, Y.Y., Panzilius, E., Kobayashi, S., Ingold, I., Irmler, M., Beckers, J., Aichler, M., Walch, A., et al. (2017). ACSL4 dictates ferroptosis sensitivity by shaping cellular lipid composition. Nat Chem Biol *13*, 91–98.

Dolma, S., Lessnick, S.L., Hahn, W.C., and Stockwell, B.R. (2003). Identification of genotype-selective antitumor agents using synthetic lethal chemical screening in engineered human tumor cells. Cancer Cell *3*, 285–296.

Doxsee, D.W., Gout, P.W., Kurita, T., Lo, M., Buckley, A.R., Wang, Y., Xue, H., Karp, C.M., Cutz, J.-C., Cunha, G.R., et al. (2007). Sulfasalazine-induced cystine starvation: Potential use for prostate cancer therapy. Prostate *67*, 162–171.

Dugo, M., Nicolini, G., Tragni, G., Bersani, I., Tomassetti, A., Colonna, V., Vecchio, M.D., Braud, F.D., Canevari, S., Anichini, A., et al. (2015). A melanoma subtype with intrinsic resistance to BRAF inhibition identified by receptor tyrosine kinases gene-driven classification. Oncotarget *6*, 5118–5133.

Eichhoff, O.M., Zipser, M.C., Xu, M., Weeraratna, A.T., Mihic, D., Dummer, R., and Hoek, K.S. (2010). The immunohistochemistry of invasive and proliferative phenotype switching in melanoma: a case report. Melanoma Res *20*, 349–355.

Emery, C.M., Vijayendran, K.G., Zipser, M.C., Sawyer, A.M., Niu, L., Kim, J.J., Hatton, C., Chopra, R., Oberholzer, P.A., Karpova, M.B., et al. (2009). MEK1 mutations confer resistance to MEK and B-RAF inhibition. PNAS *106*, 20411–20416.

Eroglu, Z., and Ribas, A. (2016). Combination therapy with BRAF and MEK inhibitors for melanoma: latest evidence and place in therapy. Therapeutic Advances in Medical Oncology *8*, 48–56.

Fallahi-Sichani, M., Becker, V., Izar, B., Baker, G.J., Lin, J.-R., Boswell, S.A., Shah, P., Rotem, A., Garraway, L.A., and Sorger, P.K. (2017). Adaptive resistance of melanoma cells to RAF inhibition via reversible induction of a slowly dividing de-differentiated state. Molecular Systems Biology *13*, 905.

Fan, J., Ye, J., Kamphorst, J.J., Shlomi, T., Thompson, C.B., and Rabinowitz, J.D. (2014). Quantitative flux analysis reveals folate-dependent NADPH production. Nature *510*, 298–302.

Flaherty, K.T., Robert, C., Hersey, P., Nathan, P., Garbe, C., Milhem, M., Demidov, L.V., Hassel, J.C., Rutkowski, P., Mohr, P., et al. (2012). Improved Survival with MEK Inhibition in BRAF-Mutated Melanoma. New England Journal of Medicine *367*, 107–114.

Fridman, W.H., Pagès, F., Sautès-Fridman, C., and Galon, J. (2012). The immune contexture in human tumours: impact on clinical outcome. Nat Rev Cancer *12*, 298–306.

Girotti, M.R., Pedersen, M., Sanchez-Laorden, B., Viros, A., Turajlic, S., Niculescu-Duvaz, D., Zambon, A., Sinclair, J., Hayes, A., Gore, M., et al. (2013). Inhibiting EGF Receptor or SRC Family Kinase Signaling Overcomes BRAF Inhibitor Resistance in Melanoma. Cancer Discovery *3*, 158–167.

Goel, V.K., Lazar, A.J.F., Warneke, C.L., Redston, M.S., and Haluska, F.G. (2006). Examination of Mutations in BRAF, NRAS, and PTEN in Primary Cutaneous Melanoma. J Invest Dermatol *126*, 154–160.

Gorrini, C., Harris, I.S., and Mak, T.W. (2013). Modulation of oxidative stress as an anticancer strategy. Nat Rev Drug Discov *12*, 931–947.

Gray-Schopfer, V.C., Karasarides, M., Hayward, R., and Marais, R. (2007). Tumor Necrosis Factor-α Blocks Apoptosis in Melanoma Cells when BRAF Signaling Is Inhibited. Cancer Res *67*, 122–129.

Guo, W., Zhao, Y., Zhang, Z., Tan, N., Zhao, F., Ge, C., Liang, L., Jia, D., Chen, T., Yao, M., et al. (2011). Disruption of xCT inhibits cell growth via the ROS/autophagy pathway in hepatocellular carcinoma. Cancer Letters *312*, 55–61.

Hansen, K.D., Irizarry, R.A., and Wu, Z. (2012). Removing technical variability in RNA-seq data using conditional quantile normalization. Biostat *13*, 204–216.

Hauschild, A., Grob, J.-J., Demidov, L.V., Jouary, T., Gutzmer, R., Millward, M., Rutkowski, P., Blank, C.U., Miller Jr, W.H., Kaempgen, E., et al. (2012). Dabrafenib in BRAF-mutated metastatic melanoma: a multicentre, open-label, phase 3 randomised controlled trial. The Lancet *380*, 358–365.

Hodi, F.S., O'Day, S.J., McDermott, D.F., Weber, R.W., Sosman, J.A., Haanen, J.B., Gonzalez, R., Robert, C., Schadendorf, D., Hassel, J.C., et al. (2010). Improved Survival with Ipilimumab in Patients with Metastatic Melanoma. New England Journal of Medicine *363*, 711–723.

Hodis, E., Watson, I.R., Kryukov, G.V., Arold, S.T., Imielinski, M., Theurillat, J.-P., Nickerson, E., Auclair, D., Li, L., Place, C., et al. (2012). A Landscape of Driver Mutations in Melanoma. Cell *150*, 251–263.

Hoek, K.S., Schlegel, N.C., Brafford, P., Sucker, A., Ugurel, S., Kumar, R., Weber, B.L., Nathanson, K.L., Phillips, D.J., Herlyn, M., et al. (2006). Metastatic potential of melanomas defined by specific gene expression profiles with no BRAF signature. Pigment Cell Research *19*, 290–302.

Hoek, K.S., Schlegel, N.C., Eichhoff, O.M., Widmer, D.S., Praetorius, C., Einarsson, S.O., Valgeirsdottir, S., Bergsteinsdottir, K., Schepsky, A., Dummer, R., et al. (2008a). Novel MITF targets identified using a two-step DNA microarray strategy. Pigment Cell & Melanoma Research *21*, 665–676.

Hoek, K.S., Eichhoff, O.M., Schlegel, N.C., Döbbeling, U., Kobert, N., Schaerer, L., Hemmi, S., and Dummer, R. (2008b). In vivo Switching of Human Melanoma Cells between Proliferative and Invasive States. Cancer Res *68*, 650–656.

Hoshida, Y., Brunet, J.-P., Tamayo, P., Golub, T.R., and Mesirov, J.P. (2007). Subclass Mapping: Identifying Common Subtypes in Independent Disease Data Sets. PLOS ONE *2*, e1195.

Hou, L., Pavan, W.J., Shin, M.K., and Arnheiter, H. (2004). Cell-autonomous and cell non-autonomous signaling through endothelin receptor B during melanocyte development. Development *131*, 3239–3247.

Howlader, N., Noone, A., Krapcho, M., Miller, D., Bishop, K., Altekruse, S., Kosary, C., Yu, M., Ruhl, J., Tatalovich, Z., et al. (2015). SEER Cancer Statistics Review (CSR) 1975-2013 (Bethesda, MD: National Cancer Institute).

Hugo, W., Shi, H., Sun, L., Piva, M., Song, C., Kong, X., Moriceau, G., Hong, A., Dahlman, K.B., Johnson, D.B., et al. (2015). Non-genomic and Immune Evolution of Melanoma Acquiring MAPKi Resistance. Cell *162*, 1271–1285.

Iorio, F., Knijnenburg, T.A., Vis, D.J., Bignell, G.R., Menden, M.P., Schubert, M., Aben, N., Gonçalves, E., Barthorpe, S., Lightfoot, H., et al. (2016). A Landscape of Pharmacogenomic Interactions in Cancer. Cell *166*, 740–754.

Iwai, Y., Ishida, M., Tanaka, Y., Okazaki, T., Honjo, T., and Minato, N. (2002). Involvement of PD-L1 on tumor cells in the escape from host immune system and tumor immunotherapy by PD-L1 blockade. PNAS *99*, 12293–12297.

Johannessen, C.M., Boehm, J.S., Kim, S.Y., Thomas, S.R., Wardwell, L., Johnson, L.A., Emery, C.M., Stransky, N., Cogdill, A.P., Barretina, J., et al. (2010). COT drives resistance to RAF inhibition through MAP kinase pathway reactivation. Nature *468*, 968–972.

Jönsson, G., Busch, C., Knappskog, S., Geisler, J., Miletic, H., Ringnér, M., Lillehaug, J.R., Borg, Å., and Lønning, P.E. (2010). Gene Expression Profiling–Based Identification of Molecular Subtypes in Stage IV Melanomas with Different Clinical Outcome. Clin Cancer Res *16*, 3356–3367.

Kawakami, Y., Dang, N., Wang, X., Tupesis, J., Robbins, P.F., Wang, R.F., Wunderlich, J.R., Yannelli, J.R., and Rosenberg, S.A. (2000). Recognition of shared melanoma antigens in association with major HLA-A alleles by tumor infiltrating T lymphocytes from 123 patients with melanoma. J. Immunother. *23*, 17–27.

Kim, D., Pertea, G., Trapnell, C., Pimentel, H., Kelley, R., and Salzberg, S.L. (2013). TopHat2: accurate alignment of transcriptomes in the presence of insertions, deletions and gene fusions. Genome Biology *14*, R36.

Kim, D., Langmead, B., and Salzberg, S.L. (2015). HISAT: a fast spliced aligner with low memory requirements. Nat Meth *12*, 357–360.

Konieczkowski, D.J., Johannessen, C.M., Abudayyeh, O., Kim, J.W., Cooper, Z.A., Piris, A., Frederick, D.T., Barzily-Rokni, M., Straussman, R., Haq, R., et al. (2014a). A Melanoma Cell State Distinction Influences Sensitivity to MAPK Pathway Inhibitors. Cancer Discovery *4*, 816–827.

Konieczkowski, D.J., Johannessen, C.M., Abudayyeh, O., Kim, J.W., Cooper, Z.A., Piris, A., Frederick, D.T., Barzily-Rokni, M., Straussman, R., Haq, R., et al. (2014b). A Melanoma Cell State Distinction Influences Sensitivity to MAPK Pathway Inhibitors. Cancer Discovery *4*, 816–827.

Kwong, L.N., Boland, G.M., Frederick, D.T., Helms, T.L., Akid, A.T., Miller, J.P., Jiang, S., Cooper, Z.A., Song, X., Seth, S., et al. (2015). Co-clinical assessment identifies patterns of BRAF inhibitor resistance in melanoma. Journal of Clinical Investigation *125*, 1459–1470.

Landsberg, J., Kohlmeyer, J., Renn, M., Bald, T., Rogava, M., Cron, M., Fatho, M., Lennerz, V., Wölfel, T., Hölzel, M., et al. (2012). Melanomas resist T-cell therapy through inflammation-induced reversible dedifferentiation. Nature *490*, 412–416.

Larkin, J., Chiarion-Sileni, V., Gonzalez, R., Grob, J.J., Cowey, C.L., Lao, C.D., Schadendorf, D., Dummer, R., Smylie, M., Rutkowski, P., et al. (2015). Combined Nivolumab and Ipilimumab or Monotherapy in Untreated Melanoma. New England Journal of Medicine *373*, 23–34.

Lauss, M., Haq, R., Cirenajwis, H., Phung, B., Harbst, K., Staaf, J., Rosengren, F., Holm, K., Aine, M., Jirström, K., et al. (2015). Genome-Wide DNA Methylation Analysis in Melanoma Reveals the Importance of CpG Methylation in MITF Regulation. Journal of Investigative Dermatology *135*, 1820–1828.

Lazova, R., Tantcheva-Poor, I., and Sigal, A.C. (2010). P75 nerve growth factor receptor staining is superior to S100 in identifying spindle cell and desmoplastic melanoma. Journal of the American Academy of Dermatology *63*, 852–858.

Lito, P., Pratilas, C.A., Joseph, E.W., Tadi, M., Halilovic, E., Zubrowski, M., Huang, A., Wong, W.L., Callahan, M.K., Merghoub, T., et al. (2012). Relief of Profound Feedback Inhibition of Mitogenic Signaling by RAF Inhibitors Attenuates Their Activity in BRAFV600E Melanomas. Cancer Cell *22*, 668–682.

Liu, F., Fu, Y., and Meyskens Jr., F.L. (2009). MiTF Regulates Cellular Response to Reactive Oxygen Species through Transcriptional Regulation of APE-1/Ref-1. Journal of Investigative Dermatology *129*, 422–431.

Liu, Y., Hayes, D.N., Nobel, A., and Marron, J.S. (2008). Statistical Significance of Clustering for High-Dimension, Low–Sample Size Data. Journal of the American Statistical Association *103*, 1281–1293.

Lo, M., Wang, Y.-Z., and Gout, P.W. (2008). The x c− cystine/glutamate antiporter: A potential target for therapy of cancer and other diseases. J. Cell. Physiol. *215*, 593–602.

Luke, J.J., Flaherty, K.T., Ribas, A., and Long, G.V. (2017). Targeted agents and immunotherapies: optimizing outcomes in melanoma. Nat Rev Clin Oncol *14*, 463–482.

Masters, J.R.W. (2000). Human cancer cell lines: fact and fantasy. Nat Rev Mol Cell Biol *1*, 233–236.

Mica, Y., Lee, G., Chambers, S.M., Tomishima, M.J., and Studer, L. (2013). Modeling Neural Crest Induction, Melanocyte Specification, and Disease-Related Pigmentation Defects in hESCs and Patient-Specific iPSCs. Cell Reports *3*, 1140–1152.

Moll, R., Divo, M., and Langbein, L. (2008). The human keratins: biology and pathology. Histochem Cell Biol *129*, 705–733.

Montagut, C., Sharma, S.V., Shioda, T., McDermott, U., Ulman, M., Ulkus, L.E., Dias-Santagata, D., Stubbs, H., Lee, D.Y., Singh, A., et al. (2008). Elevated CRAF as a Potential Mechanism of Acquired Resistance to BRAF Inhibition in Melanoma. Cancer Res *68*, 4853–4861.

Monti, S., Tamayo, P., Mesirov, J., and Golub, T. (2003). Consensus Clustering: A Resampling-Based Method for Class Discovery and Visualization of Gene Expression Microarray Data. Machine Learning *52*, 91–118.

Mort, R.L., Jackson, I.J., and Patton, E.E. (2015). The melanocyte lineage in development and disease. Development *142*, 620–632.

Müller, J., Krijgsman, O., Tsoi, J., Robert, L., Hugo, W., Song, C., Kong, X., Possik, P.A., Cornelissen-Steijger, P.D.M., Foppen, M.H.G., et al. (2014). Low MITF/AXL ratio predicts early resistance to multiple targeted drugs in melanoma. Nat Commun *5*, 5712.

Nazarian, R., Shi, H., Wang, Q., Kong, X., Koya, R.C., Lee, H., Chen, Z., Lee, M.-K., Attar, N., Sazegar, H., et al. (2010). Melanomas acquire resistance to B-RAF(V600E) inhibition by RTK or N-RAS upregulation. Nature *468*, 973–977.

Nissan, M.H., Pratilas, C.A., Jones, A.M., Ramirez, R., Won, H., Liu, C., Tiwari, S., Kong, L., Hanrahan, A.J., Yao, Z., et al. (2014). Loss of NF1 in Cutaneous Melanoma Is Associated with RAS Activation and MEK Dependence. Cancer Res *74*, 2340–2350.

O'Connell, M.P., Marchbank, K., Webster, M.R., Valiga, A.A., Kaur, A., Vultur, A., Li, L., Herlyn, M., Villanueva, J., Liu, Q., et al. (2013). Hypoxia induces phenotypic plasticity and therapy resistance in melanoma via the tyrosine kinase receptors ROR1 and ROR2. Cancer Discovery CD-13-0005.

Ordóñez, N.G. (2014). Value of melanocytic-associated immunohistochemical markers in the diagnosis of malignant melanoma: a review and update. Human Pathology *45*, 191–205.

Paraiso, K.H.T., Fedorenko, I.V., Cantini, L.P., Munko, A.C., Hall, M., Sondak, V.K., Messina, J.L., Flaherty, K.T., and Smalley, K.S.M. (2010). Recovery of phospho-ERK activity allows melanoma cells to escape from BRAF inhibitor therapy. Br J Cancer *102*, 1724–1730.

Paraiso, K.H.T., Thakur, M.D., Fang, B., Koomen, J.M., Fedorenko, I.V., John, J.K., Tsao, H., Flaherty, K.T., Sondak, V.K., Messina, J.L., et al. (2014). Ligand independent EphA2 signaling drives the adoption of a targeted therapy-mediated metastatic melanoma phenotype. Cancer Discovery CD-14-0293.

Perou, C.M., Sørlie, T., Eisen, M.B., van de Rijn, M., Jeffrey, S.S., Rees, C.A., Pollack, J.R., Ross, D.T., Johnsen, H., Akslen, L.A., et al. (2000). Molecular portraits of human breast tumours. Nature *406*, 747–752.

Piskounova, E., Agathocleous, M., Murphy, M.M., Hu, Z., Huddlestun, S.E., Zhao, Z., Leitch, A.M., Johnson, T.M., DeBerardinis, R.J., and Morrison, S.J. (2015). Oxidative stress inhibits distant metastasis by human melanoma cells. Nature *527*, 186–191.

Poulikakos, P.I., Persaud, Y., Janakiraman, M., Kong, X., Ng, C., Moriceau, G., Shi, H., Atefi, M., Titz, B., Gabay, M.T., et al. (2011). RAF inhibitor resistance is mediated by dimerization of aberrantly spliced BRAF(V600E). Nature *480*, 387–390.

Raj, L., Ide, T., Gurkar, A.U., Foley, M., Schenone, M., Li, X., Tolliday, N.J., Golub, T.R., Carr, S.A., Shamji, A.F., et al. (2011). Selective killing of cancer cells by a small molecule targeting the stress response to ROS. Nature *475*, 231–234.

Ravindran Menon, D., Das, S., Krepler, C., Vultur, A., Rinner, B., Schauer, S., Kashofer, K., Wagner, K., Zhang, G., Bonyadi Rad, E., et al. (2014). A stress-induced early innate response causes multidrug tolerance in melanoma. Oncogene.

Riesenberg, S., Groetchen, A., Siddaway, R., Bald, T., Reinhardt, J., Smorra, D., Kohlmeyer, J., Renn, M., Phung, B., Aymans, P., et al. (2015). MITF and c-Jun antagonism interconnects melanoma dedifferentiation with pro-inflammatory cytokine responsiveness and myeloid cell recruitment. Nat Commun *6*, 8755.

Robert, C., Long, G.V., Brady, B., Dutriaux, C., Maio, M., Mortier, L., Hassel, J.C., Rutkowski, P., McNeil, C., Kalinka-Warzocha, E., et al. (2015). Nivolumab in Previously Untreated Melanoma without BRAF Mutation. New England Journal of Medicine *372*, 320–330.

Rodeck, U., Nishiyama, T., and Mauviel, A. (1999). Independent Regulation of Growth and SMAD-mediated Transcription by Transforming Growth Factor β in Human Melanoma Cells. Cancer Res *59*, 547–550.

Rosenberg, S.A., Yang, J.C., Sherry, R.M., Kammula, U.S., Hughes, M.S., Phan, G.Q., Citrin, D.E., Restifo, N.P., Robbins, P.F., Wunderlich, J.R., et al. (2011). Durable Complete Responses in Heavily Pretreated Patients with Metastatic Melanoma Using T-Cell Transfer Immunotherapy. Clin Cancer Res *17*, 4550–4557.

Samatar, A.A., and Poulikakos, P.I. (2014). Targeting RAS-ERK signalling in cancer: promises and challenges. Nat Rev Drug Discov *13*, 928–942.

Santarpia, L., Lippman, S.L., and El-Naggar, A.K. (2012). Targeting the Mitogen-Activated Protein Kinase RAS-RAF Signaling Pathway in Cancer Therapy. Expert Opin Ther Targets *16*, 103–119.

Sauka-Spengler, T., and Bronner-Fraser, M. (2008). A gene regulatory network orchestrates

neural crest formation. Nat Rev Mol Cell Biol *9*, 557–568.

Schepsky, A., Bruser, K., Gunnarsson, G.J., Goodall, J., Hallsson, J.H., Goding, C.R., Steingrimsson, E., and Hecht, A. (2006). The Microphthalmia-Associated Transcription Factor Mitf Interacts with β-Catenin To Determine Target Gene Expression. Mol. Cell. Biol. *26*, 8914–8927.

Seashore-Ludlow, B., Rees, M.G., Cheah, J.H., Cokol, M., Price, E.V., Coletti, M.E., Jones, V., Bodycombe, N.E., Soule, C.K., Gould, J., et al. (2015). Harnessing Connectivity in a Large-Scale Small-Molecule Sensitivity Dataset. Cancer Discov.

Shaffer, S.M., Dunagin, M.C., Torborg, S.R., Torre, E.A., Emert, B., Krepler, C., Beqiri, M., Sproesser, K., Brafford, P.A., Xiao, M., et al. (2017). Rare cell variability and drug-induced reprogramming as a mode of cancer drug resistance. Nature *advance online publication*.

Shakhova, O., Zingg, D., Schaefer, S.M., Hari, L., Civenni, G., Blunschi, J., Claudinot, S., Okoniewski, M., Beermann, F., Mihic-Probst, D., et al. (2012). Sox10 promotes the formation and maintenance of giant congenital naevi and melanoma. Nat Cell Biol *14*, 882–890.

Shi, H., Moriceau, G., Kong, X., Lee, M.-K., Lee, H., Koya, R.C., Ng, C., Chodon, T., Scolyer, R.A., Dahlman, K.B., et al. (2012). Melanoma whole-exome sequencing identifies V600EB-RAF amplification-mediated acquired B-RAF inhibitor resistance. Nat Commun *3*, 724.

Shi, H., Hugo, W., Kong, X., Hong, A., Koya, R.C., Moriceau, G., Chodon, T., Guo, R., Johnson, D.B., Dahlman, K.B., et al. (2014). Acquired Resistance and Clonal Evolution in Melanoma during BRAF Inhibitor Therapy. Cancer Discovery *4*, 80–93.

Shi, P., Ray, S., Zhu, Q., and Kon, M.A. (2011). Top scoring pairs for feature selection in machine learning and applications to cancer outcome prediction. BMC Bioinformatics *12*, 375.

Shimada, K., Hayano, M., Pagano, N.C., and Stockwell, B.R. (2016). Cell-Line Selectivity Improves the Predictive Power of Pharmacogenomic Analyses and Helps Identify NADPH as Biomarker for Ferroptosis Sensitivity. Cell Chemical Biology *23*, 225–235.

Søndergaard, J.N., Nazarian, R., Wang, Q., Guo, D., Hsueh, T., Mok, S., Sazegar, H., MacConaill, L.E., Barretina, J.G., Kehoe, S.M., et al. (2010). Differential sensitivity of melanoma cell lines with BRAF V600E mutation to the specific Raf inhibitor PLX4032. Journal of Translational Medicine *8*, 39.

Sotiriou, C., and Pusztai, L. (2009). Gene-Expression Signatures in Breast Cancer. New England Journal of Medicine *360*, 790–800.

Soudja, S.M., Wehbe, M., Mas, A., Chasson, L., Tenbossche, C.P. de, Huijbers, I., Eynde, B.V. den, and Schmitt-Verhulst, A.-M. (2010). Tumor-Initiated Inflammation Overrides Protective Adaptive Immunity in an Induced Melanoma Model in Mice. Cancer Res *70*, 3515–3525.

Spitz, F., and Furlong, E.E.M. (2012). Transcription factors: from enhancer binding to developmental control. Nat Rev Genet *13*, 613–626.

Su, F., Viros, A., Milagre, C., Trunzer, K., Bollag, G., Spleiss, O., Reis-Filho, J.S., Kong, X., Koya, R.C., Flaherty, K.T., et al. (2012). RAS Mutations in Cutaneous Squamous-Cell

Carcinomas in Patients Treated with BRAF Inhibitors. New England Journal of Medicine *366*, 207–215.

Subramanian, A., Tamayo, P., Mootha, V.K., Mukherjee, S., Ebert, B.L., Gillette, M.A., Paulovich, A., Pomeroy, S.L., Golub, T.R., Lander, E.S., et al. (2005). Gene set enrichment analysis: A knowledge-based approach for interpreting genome-wide expression profiles. PNAS *102*, 15545–15550.

Sullivan, R.J., and Flaherty, K. (2013). MAP kinase signaling and inhibition in melanoma. Oncogene *32*, 2373–2379.

Sun, C., Wang, L., Huang, S., Heynen, G.J.J.E., Prahallad, A., Robert, C., Haanen, J., Blank, C., Wesseling, J., Willems, S.M., et al. (2014). Reversible and adaptive resistance to BRAF(V600E) inhibition in melanoma. Nature *508*, 118–122.

Takeda, K., Yasumoto, K., Takada, R., Takada, S., Watanabe, K., Udono, T., Saito, H., Takahashi, K., and Shibahara, S. (2000). Induction of Melanocyte-specific Microphthalmia-associated Transcription Factor by Wnt-3a. J. Biol. Chem. *275*, 14013–14016.

Taube, J.M., Anders, R.A., Young, G.D., Xu, H., Sharma, R., McMiller, T.L., Chen, S., Klein, A.P., Pardoll, D.M., Topalian, S.L., et al. (2012). Colocalization of Inflammatory Response with B7-H1 Expression in Human Melanocytic Lesions Supports an Adaptive Resistance Mechanism of Immune Escape. Science Translational Medicine *4*, 127ra37-127ra37.

Telley, L., Govindan, S., Prados, J., Stevant, I., Nef, S., Dermitzakis, E., Dayer, A., and Jabaudon, D. (2016). Sequential transcriptional waves direct the differentiation of newborn neurons in the mouse neocortex. Science *351*, 1443–1446.

Thomas, A.J., and Erickson, C.A. (2008). The making of a melanocyte: the specification of melanoblasts from the neural crest. Pigment Cell & Melanoma Research *21*, 598–610.

Thomas, N.E., Busam, K.J., From, L., Kricker, A., Armstrong, B.K., Anton-Culver, H., Gruber, S.B., Gallagher, R.P., Zanetti, R., Rosso, S., et al. (2013). Tumor-Infiltrating Lymphocyte Grade in Primary Melanomas Is Independently Associated With Melanoma-Specific Survival in the Population-Based Genes, Environment and Melanoma Study. J Clin Oncol *31*, 4252–4259.

Timmerman, L.A., Holton, T., Yuneva, M., Louie, R.J., Padró, M., Daemen, A., Hu, M., Chan, D.A., Ethier, S.P., van 't Veer, L.J., et al. (2013). Glutamine Sensitivity Analysis Identifies the xCT Antiporter as a Common Triple-Negative Breast Tumor Therapeutic Target. Cancer Cell *24*, 450–465.

Tirosh, I., Izar, B., Prakadan, S.M., Wadsworth, M.H., Treacy, D., Trombetta, J.J., Rotem, A., Rodman, C., Lian, C., Murphy, G., et al. (2016). Dissecting the multicellular ecosystem of metastatic melanoma by single-cell RNA-seq. Science *352*, 189–196.

Titz, B., Lomova, A., Le, A., Hugo, W., Kong, X., ten Hoeve, J., Friedman, M., Shi, H., Moriceau, G., Song, C., et al. (2016). JUN dependency in distinct early and late BRAF inhibition adaptation states of melanoma. Cell Discov *2*, 16028.

Trapnell, C., Roberts, A., Goff, L., Pertea, G., Kim, D., Kelley, D.R., Pimentel, H., Salzberg, S.L., Rinn, J.L., and Pachter, L. (2012). Differential gene and transcript expression analysis of RNA-

seq experiments with TopHat and Cufflinks. Nat. Protocols *7*, 562–578.

Tusher, V.G., Tibshirani, R., and Chu, G. (2001). Significance analysis of microarrays applied to the ionizing radiation response. Proc Natl Acad Sci U S A *98*, 5116–5121.

Vazquez, F., Lim, J.-H., Chim, H., Bhalla, K., Girnun, G., Pierce, K., Clish, C.B., Granter, S.R., Widlund, H.R., Spiegelman, B.M., et al. (2013). PGC1α Expression Defines a Subset of Human Melanoma Tumors with Increased Mitochondrial Capacity and Resistance to Oxidative Stress. Cancer Cell *23*, 287–301.

Verfaillie, A., Imrichova, H., Atak, Z.K., Dewaele, M., Rambow, F., Hulselmans, G., Christiaens, V., Svetlichnyy, D., Luciani, F., Mooter, L.V. den, et al. (2015). Decoding the regulatory landscape of melanoma reveals TEADS as regulators of the invasive cell state. Nature Communications *6*, 6683.

Verhaak, R.G.W., Hoadley, K.A., Purdom, E., Wang, V., Qi, Y., Wilkerson, M.D., Miller, C.R., Ding, L., Golub, T., Mesirov, J.P., et al. (2010). Integrated Genomic Analysis Identifies Clinically Relevant Subtypes of Glioblastoma Characterized by Abnormalities in PDGFRA, IDH1, EGFR, and NF1. Cancer Cell *17*, 98–110.

Villanueva, J., Vultur, A., Lee, J.T., Somasundaram, R., Fukunaga-Kalabis, M., Cipolla, A.K., Wubbenhorst, B., Xu, X., Gimotty, P.A., Kee, D., et al. (2010). Acquired Resistance to BRAF Inhibitors Mediated by a RAF Kinase Switch in Melanoma Can Be Overcome by Cotargeting MEK and IGF-1R/PI3K. Cancer Cell *18*, 683–695.

Wagle, N., Allen, E.M.V., Treacy, D.J., Frederick, D.T., Cooper, Z.A., Taylor-Weiner, A., Rosenberg, M., Goetz, E.M., Sullivan, R.J., Farlow, D.N., et al. (2014). MAP Kinase Pathway Alterations in BRAF-Mutant Melanoma Patients with Acquired Resistance to Combined RAF/MEK Inhibition. Cancer Discovery *4*, 61–68.

Wan, P.T.C., Garnett, M.J., Roe, S.M., Lee, S., Niculescu-Duvaz, D., Good, V.M., Project, C.G., Jones, C.M., Marshall, C.J., Springer, C.J., et al. (2004). Mechanism of Activation of the RAF-ERK Signaling Pathway by Oncogenic Mutations of B-RAF. Cell *116*, 855–867.

Whittaker, S.R., Theurillat, J.-P., Allen, E.V., Wagle, N., Hsiao, J., Cowley, G.S., Schadendorf, D., Root, D.E., and Garraway, L.A. (2013). A Genome-Scale RNA Interference Screen Implicates NF1 Loss in Resistance to RAF Inhibition. Cancer Discovery *3*, 350–362.

Wilkerson, M.D., and Hayes, D.N. (2010). ConsensusClusterPlus: a class discovery tool with confidence assessments and item tracking. Bioinformatics *26*, 1572–1573.

Xie, Y., Hou, W., Song, X., Yu, Y., Huang, J., Sun, X., Kang, R., and Tang, D. (2016). Ferroptosis: process and function. Cell Death Differ *23*, 369–379.

Yagoda, N., von Rechenberg, M., Zaganjor, E., Bauer, A.J., Yang, W.S., Fridman, D.J., Wolpaw, A.J., Smukste, I., Peltier, J.M., Boniface, J.J., et al. (2007). RAS–RAF–MEK-dependent oxidative cell death involving voltage-dependent anion channels. Nature *447*, 865–869.

Yang, W.S., and Stockwell, B.R. (2008). Synthetic Lethal Screening Identifies Compounds Activating Iron-Dependent, Nonapoptotic Cell Death in Oncogenic-RAS-Harboring Cancer Cells.

Chemistry & Biology *15*, 234–245.

Yang, W.S., SriRamaratnam, R., Welsch, M.E., Shimada, K., Skouta, R., Viswanathan, V.S., Cheah, J.H., Clemons, P.A., Shamji, A.F., Clish, C.B., et al. (2014). Regulation of Ferroptotic Cancer Cell Death by GPX4. Cell *156*, 317–331.

Yang, W.S., Kim, K.J., Gaschler, M.M., Patel, M., Shchepinov, M.S., and Stockwell, B.R. (2016). Peroxidation of polyunsaturated fatty acids by lipoxygenases drives ferroptosis. PNAS *113*, E4966–E4975.

Yoshihara, K., Shahmoradgoli, M., Martínez, E., Vegesna, R., Kim, H., Torres-Garcia, W., Treviño, V., Shen, H., Laird, P.W., Levine, D.A., et al. (2013). Inferring tumour purity and stromal and immune cell admixture from expression data. Nat Commun *4*.